HIERARCHICAL MICROSTRUCTURE DESIGN AND CAST PROCESSING ROUTE OF A MODIFIED TNM GAMMA TIAL ALLOY

DANIEL BERNAL RODRÍGUEZ

Supervisors:

Dr. Iñaki Hurtado

Dr. Xabier Chamorro

A thesis submitted in fulfillment of the requirements for the degree of

Doctor by Mondragon Unibertsitatea

Mechanical and Manufacturing Department

Mondragon Unibertsitatea

February 4, 2021

Preface

Declaration of Originality

I hereby declare that this thesis, and the work presented in it with its results, were carried out entirely by me at the Mechanical and Manufacturing Department of the University of Mondragon's Polytechnic School. Some results come from the collaboration with the Ruhr Universität Bochum.

Daniel Bernal

February 2021

Acknowledgments

Llegado este punto, miro hacia atrás y me llena de alegría el poder compartir este trabajo que no habría sido posible sin la contribución de una serie de personas. Han sido unos estupendos años, llenos de aprendizaje tanto científico como de desarrollo personal, que me han ayudado a alcanzar este momento tan mágico.

En primer lugar, me gustaría agradecer en especial a mis directores de tesis, el Dr. Iñaki Hurtado y el Dr. Xabier Chamorro por darme la oportunidad de hacer esta tesis, vuestra dedicación y apoyo ha sido incondicional, habéis sido como una familia para mí.

En segundo lugar, a ITP Aero por su participación en el proyecto TALDEA. En especial a Iñaki Madariaga por su dedicación y consejos, has sido de gran apoyo y has aportado un enorme valor a este trabajo.

También me gustaría agradecer a Erika Domínguez y Larraitz Azpitarte por todos esos buenos momentos vividos en el laboratorio de materiales, hemos aprendido y disfrutado mucho.

A mis compañeros, por haberme acompañado en esta etapa de mi vida, cada café ha sido un momento único para reponerse de energía y de esa chispa que te lleva a trabajar con una sonrisa.

A mi familia, por todo el apoyo y cariño. Gracias por educarme de la forma que lo habéis hecho y hacerme tan feliz.

Abstract

Gamma titanium aluminides following the β-solidifying pathway, are intermetallic alloys that have the potential to replace heavier materials in high temperature structural applications, such as aerospace and aeronautics. They meet the requirements for being used in the newly designed turbines that have to withstand higher demanding conditions, allowing improved efficiency, as well as pollution and noise reduction. Indeed, γ-TiAl are an attractive option to replace Ni-base superalloys due to their lower density, good mechanical properties at elevated temperatures and good oxidation resistance.

Among them, the third generation of γ-TiAl alloy TNM is a promising candidate for utilization in the low-pressure turbines (LPT) of aircraft. However, its manufacturing route is time-consuming, involving casting/HIPing plus forging and multiple HT to achieve the required properties. In this regard, alloying elements play a key role in this process, hence boron is often added to refine the grain size in order to improve mechanical properties. However, the formation mechanism of the different types of borides in cast TiAl alloys is not yet clearly understood.

In light of this gap, this study seeks to design a modified TNM alloy with superior properties and define a suitable processing window. This was accomplished by designing a simplified processing route and correlating the chemical composition and solidification cooling rate of cast TiAl alloys, with the type of boride precipitated and the resulting microstructure.

The study reveals that simpler processing namely casting/HIPing plus a single-step heat treatment achieve a microstructure appropriate for structural applications. Regarding microstructure developing, the work also shows that boron contents below a critical value and cooling rates during solidification above a key value promote the formation of detrimental ribbon borides. While boron contents above a critical value and cooling rates during solidification below a key value promote the formation of a refined microstructure through the precipitation of the beneficial boride. Finally, a novel integrated HIP-heat-treatment processing route is presented to achieve an optimized creep resistance modified TNM alloy.

Resumen

Los aluminuros de titanio que solidifican mediante la via β, son aleaciones intermetálicas que tienen el potencial de sustituir a materiales más pesados en aplicaciones estructurales de alta temperatura. Cumplen los requisitos de las nuevas turbinas que deben soportar condiciones más exigentes, lo que permite aumentar la eficiencia, así como reducir la contaminación y el ruido. De hecho, las aleaciones γ-TiAl representan una opción atractiva para sustituir a las superaleaciones de base níquel debido a su menor densidad, sus buenas propiedades mecánicas a altas temperaturas y su elevada resistencia frente a la oxidación.

De entre ellas, la aleación TNM destaca por su potencial para ser empleada en los álabes de la turbina de baja presión de los aviones. Sin embargo, la ruta convencional para su fabricación es larga y costosa, ya que conlleva los procesos de fundición, HIP y forjado, así como múltiples tratamientos térmicos para lograr las propiedades requeridas. En este sentido, los elementos de aleación juegan un papel clave en este proceso, es por ello que el boro se suele añadir para afinar el tamaño del grano, con el fin de mejorar las propiedades mecánicas. Sin embargo, dependiendo de las condiciones del proceso, así como de la aleación, el tipo de boruro formado es diferente. Dada la complejidad del mecanismo de formación de los diferentes tipos de boruros en las aleaciones de TiAl fundidas, aún no se conoce con claridad bajo qué condiciones se forman cada uno de ellos.

En consecuencia, este estudio pretende diseñar una aleación TNM con unas propiedades mecánicas mejoradas, mediante el ajuste de los parámetros de proceso clave. Para ello se ha simplificado la ruta de fabricación, a la vez que se ha correlación la composición química y la velocidad de solidificación con el tipo de boruro precipitado y la microestructura resultante.

El estudio revela que una ruta de fabricación más sencilla, a través de los procesos de fundición, HIP y tratamiento térmico monoetapa, permiten obtener una microestructura adecuada para aplicaciones estructurales. En cuanto al desarrollo de la microestructura, el estudio muestra que un contenido en boro inferior a un valor crítico y una velocidad de enfriamiento durante la solidificación por encima de un valor crítico, conllevan la formación de cadenas de boruros denominados “ribbon”, perjudiciales para las propiedades mecánicas. Mientras que un contenido en boro superior a un valor crítico y una velocidad de enfriamiento durante la solidificación inferior a un valor crítico, potencian el afinamiento de la microestructura, a través de la precipitación homogénea de boruros denominados “blocky”. Por último, se presenta una nueva ruta de fabricación que de forma integrada combina el ciclo de HIP y de tratamiento térmico, con el fin de conseguir una aleación TNM optimizada.

Laburpena

Gamma familiako titaniozko aluminioak, beta bidez solidotzen direnak, tenperatura altuetan erabiltzen diren material astunagoak ordezkatzeko ahalmena dituzte, batez ere aplikazio aeroespazialan eta aeronautikan ere. Diseinu berriko turbinen baldintza zorrotzak jasatzen dituzte, eta horrek eraginkortasuna hobetzea eta kutsadura eta baita zarata murriztea ahalbidetzen du. Izan ere, γ-TiAl aleazioak Ni oinarriko superaleazioak ordezkatzeko aukera erakargarria izan daitezke, dentsitate txikiagoa dutelako, tenperatura altuetan dituzten propietate mekaniko onengatik eta oxidazioarekiko erresistentzia ona dutelako.

Horien artean, TNM azpiklaseko γ-TiAl aleazioaren hirugarren belaunaldia, hegazkinetako presio baxuko turbinetan (LPT) erabiltzeko etorkizun handiko hautagaia da. Hala ere, bere fabrikazio ibilbidea luzea eta garestia da (galdaketa, HIP eta forjaketa prozesuak baitakartz). Gainera, beharrezko propietateak lortzeko tratamendu termiko ugari ere beharko ditu. Aleazio elementuei dagokienez, Boroa gehitu ohi da, boruro egokia osatzen bada alearen tamaina finagoa egin daiteke, honela, propietate mekanikoak hobetuz. Hala ere, galdatutako TiAl-aleazioetan boruro mota ezberdinak sortzeko mekanismoa oraindik ez dago argi.

Beraz, ikerketa honen helburua propietate hobeagoak dituen TNM aleazio berezi bat diseinatzea da, baita material horren prozesamendu-leiho egokia definitzea. Horretarako, lehendabizi, erraztutako prozesatze ibilbide bat diseinatu da eta ondoren, konposizio kimikoa eta solidotze-abiadura erlazionatu dira osatutako boruro motarekin eta lortutako mikroegiturarekin.

Ikerketaren arabera, prozesamendu sinpleago batek, non galdaketa eta tratamendu termikoa integratuta duen HIP prozesua, mikroegitura egokia sortzea lortzen du. Mikroegituraren garapenari dagokionez, ikerketak agerian uzten du nola boroko edukia balio kritiko batetik behera izanik eta balio kritiko batetik gorako solidotze-abiadurak boruro kaltegarrien kateak sortzea sustatzen dituela. Aldi berean, balio kritiko baten gainetik dauden boro-edukiek eta solidotze-abiadura kritiko baten azpitik ari diren aleazioak, boruro onuragarria sustatzen dute eta beraz mikroegitura hobeagoa lortzen da. Azkenik, TiAl-aleazioetarako tratamendu termikoa integratuta duen HIP prosezu berri bat aurkezten da, TNM aleazio berritzaile eta optimizatu bat lortu ahal izateko.

Contents

Nomenclature

LPT	Low Pressure Turbine
HIP	Hot Isostatic Pressing
CCIM	Cold Crucible Induction Melting
ISM	Induction Skull Melting
HT	Heat Treatment
BCC	Body-Centred Cubic
CR	Cellular Reaction
HCP	Hexagonal Close-Packed
BDT	Brittle-Ductile Transition
DRX	Dynamic Recrystallization
BDTC	Brittle-Ductile Transition during Creep
SEM	Scanning Electron Microscopy
BSE	Backscattered Electron
HTC	Heat Transfer Coefficient
EDS	Energy Dispersive X-Ray Spectroscopy
VAR	Vacuum Arc Remelting
PAM	Plasma Arc Melting
emf	electromagnetic force
CFD	Computational Fluid Dynamics
DSC	Differential Scanning Calorimetry
T_m	Melting temperature
IHH	Integrated HIP/HT processing
LAS	Leica Application Suite
URQ	Uniform Rapid Quenching furnace
FCT	Face-Centred Tetragonal
PAM	Plasma Arc Melting

ε_{min}	Minimum creep rate
PVD	Physical Vapour Deposition
CVD	Chemical Vapour Deposition
K_p	Parabolic oxidation rate constant
Q	Activation energy for oxidation

List of Figures

List of Tables

Chapter 1

1 Introduction

In this chapter, the framework of the dissertation and the motivation to conduct this research is presented. Then, the research objectives and the working methodology to accomplish those objectives are defined.

1.1 Motivation

The focus of interest in the aeronautics, automotive and aerospace sectors is the development of components with improved mechanical properties and reduced weight so as to improve the efficiency of engines and reduce fuel consumption. New designs and materials must therefore be developed to satisfy such demands, in additon to complying with even more restrictive environmental policies.

γ-TiAls are attracting so much attention because they have a unique strength to weight ratio in comparison to the heavier nickel-base superalloys. In comparison with other aerospace structural materials, it has been established that γ-TiAl alloys present the following properties: high melting point, low density, high specific strengths and moduli, low diffusivity, good structural stability, good resistance against oxidation and corrosion and high ignition resistance [1].

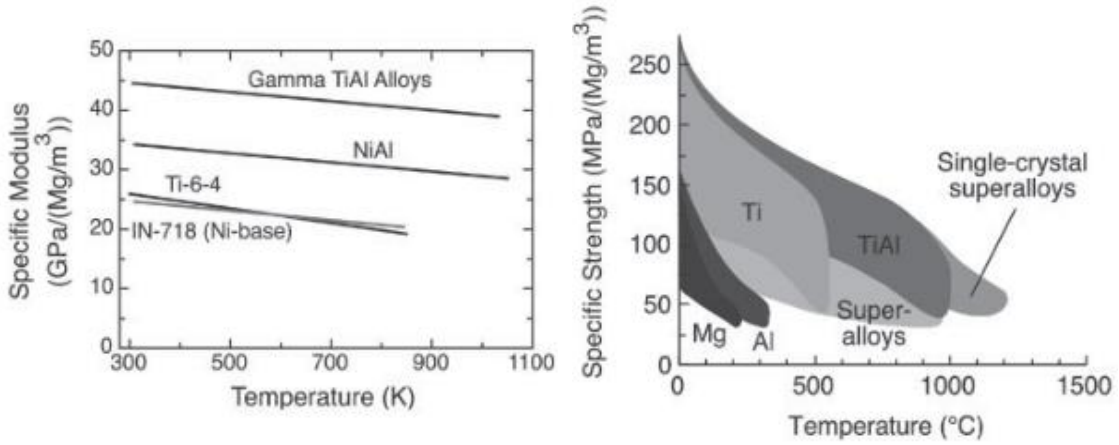

a) **b)**

Figure 1-1. Mechanical properties of TiAl; a) Specific moduli and b) Specific strength [1]

As Figure 1-1 shows, γ-TiAl can replace heavier nickel-base superalloys in applications where the service temperature does not exceed around 800 ºC. Thus, they provide a higher specific strength, which leads to the development of new engine designs [2].

Therefore, intermetallic γ-TiAl alloys are a key component in the weight reduction of components subject to rotation cycles in the turbofan, such as the fan, compressor and especially the low-pressure turbine (LPT) blades. This implies a lower energy consumption in the movement of such components increasing the thrust of the engine.

The LPT has a high rotation speed, and thus the material must be of low density, high strength and capable of withstanding high mechanical loads, maintaining a certain ductility at room temperature [3].

This has led to new designs for applications at high service temperature, delivering a lighter weight to improve efficiency. These designs are already available in the engines of commercial aeroplanes such as the PW1000G-JM engine [2].

Figure 1-2. Geared turbofan jet engine [2]

This geared turbofan engine has achieved a reduction in fuel consumption, as well as CO_2, NO_x and noise emissions. By decoupling the fan and the LPT stages through the introduction of a speed-reduction gearbox, all components can run at their respective optimum speed. Since these new engines operate under different conditions, the materials used have to be adapted. Among the candidates, TiAl alloys are an attractive alternative given the above-mentioned characteristics.

To develop a γ-TiAl alloy that had a homogeneous microstructure and could be forged under nearly conventional conditions, Clemens *et al.* developed the so-called TNM alloy with the baseline chemical composition of Ti-(42-45)Al-5Nb-1Mo-0.1B at.% [4]. However, TNM alloys are not optimized for casting, and consequently there is a need for adjusting the chemical composition as well as the melting process.

Thus, a new alloy and its postprocessing routes for their adaptation to casting needs to be developed. This will enable us to meet the demands of industry: reducing the machining operations and equipment required, saving money and time, and maintaining good mechanical properties. The present work employs the Cold Crucible Induction Melting (CCIM) or so-called Induction Skull Melting (ISM), as this technology can melt TiAl alloys to the required quality in terms of low chemical variations and reduced machining operations.

This study therefore aims to adapt the forged TNM alloy to a new alloy optimised for casting. For this purpose, the chemical composition was adjusted and the key melting process parameters were optimized, as well as the process parameters of the downstream processes. This allowed us to obtain high-value added TiAl components.

1.2 Objectives

The main objective of this dissertation is to achieve a novel aeronautic quality castable TNM alloy by modifying the chemical composition, optimizing solidification and heat treatments (HT). To this end, the following specific objectives have been defined:

- Modify the chemical composition to render it suitable for this application, by achieving a homogeneous microstructure and the precipitation of the desirable boride.

- Adjust the melting and solidification path to ensure an optimal microstructure, precipitation of the beneficial borides, and well-balanced chemical composition in the bulk material.

- Design a HT sequence that provides a creep resistance microstructure suitable for LPT components, reducing the working processing time by proposing a novel processing workflow.

1.3 Outline of the dissertation

To achieve the objectives defined in Section 1.2, the thesis document is divided into four blocks, as shown in Figure 1-3. The first addresses the bibliographic review of TiAl alloys and the characterization of the master alloy. The second covers the basics of the casting of TiAl alloys and the mould design, and the third block addresses the development of the modified TNM alloys. Finally, the fourth block focuses on the design of the HT for the novel modified TNM alloy and its subsequent validation by creep testing.

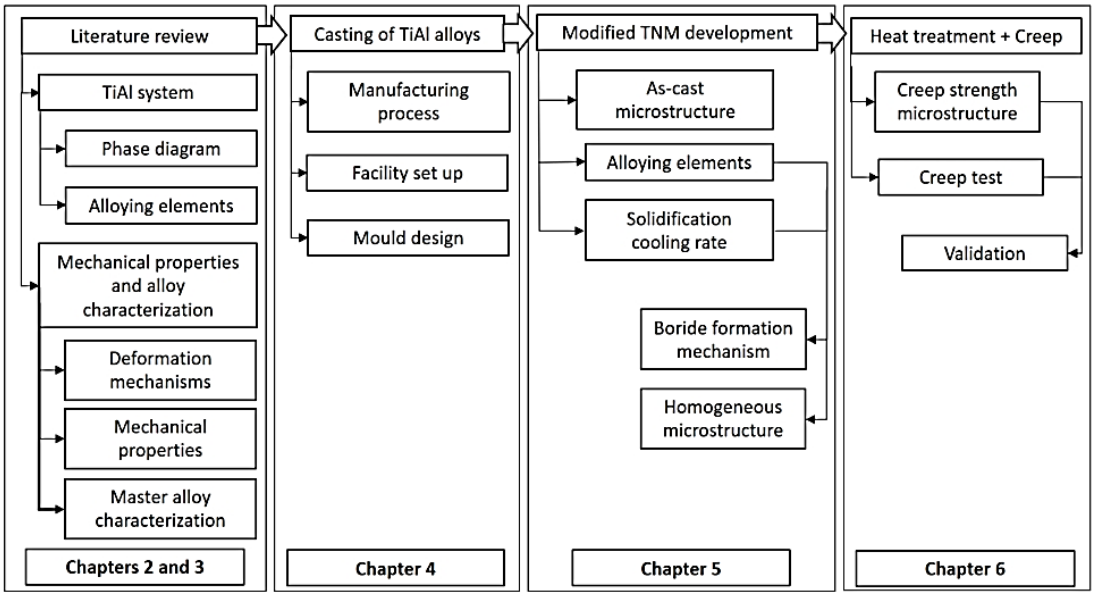

Figure 1-3. Research workflow

Chapter 2, “TiAl System” outlines the required knowledge of the key microstructural parameters of TiAl alloys. The bibliographic analysis first focusses on the basics of TiAl alloys. Then the phase diagram, microconstituents and the effect the alloying elements for the selected TNM master alloy are covered.

In chapter 3, “Mechanical Properties and Alloy Characterisation”, a bibliographic study of the mechanical properties of TiAl alloys is conducted, to determine the most relevant phenomena that control TiAl behaviour. This identifies the effect of the microstructure on the mechanical properties of the material under service conditions. Finally, characterisation of the as-received master alloy is performed to determine the microstructural key points, and set the baseline for the design of the new alloy.

Chapter 4, "The casting of TiAl Alloys", focuses on understanding the casting process of β-solidifying TiAl alloys, covering the manufacturing of the supplied billets of TNM master alloy, to their casting in the MGEP facilities. The design of the casting part and the mould is analysed to achieve different processing windows that determine the relationship between casting processing parameters and microstructure.

Chapter 5, “Alloy Design”, describes the modification of the chemical composition of the master alloy and the adjustment of the melting conditions, to obtain a homogeneous microstructure and the precipitation of the appropriate boride. To this end, the effect of different amounts of the alloying elements, as well as the solidification cooling rate in the generation of the as-cast microstructure are detailed. Finally, a boride formation mechanism is proposed.

Chapter 6, “Heat Treatments and Creep”, covers the HT design that provides the required final mechanical properties for the components. Hence, the effect of different microstructures in terms of type, quantity and morphology of the different micro-constituents on mechanical properties is analysed, and the final microstructure validated by creep tests is discussed. Since these components usually work for long periods at high temperatures and under relatively continuous load, creep behaviour is a suitable test for microstructural evaluations. In addition, a more cost-effective processing route for modified TNM alloys through Casting/Hot Isostatic Pressing (HIP) and a single step HT is presented, and a novel integrated HIP+HT (IHH) process for β-solidifying γ-TiAl alloys is shown.

In chapter 7, “Conclusions and Future Work”, the main conclusions and contributions of this work are set out below. This chapter also identifies the future lines of work in this field to respond to the main challenges identified and uncovered in this research.

Chapter 2

2 TiAl System

This chapter covers the basics of TiAl alloys from the point of view of microstructure. First, γ-TiAl alloys are presented and the reasons why they have become so attractive are discussed. Then, the effect of the chemical elements are analysed, as well as the role of the potential phases to be formed. This helps to determine the limitations of the different generations of TiAl alloys, and define the key points for improvement. The chapter concludes with the selection of the most suitable family of TiAl alloys, addressing their main microstructural characteristics, such as phase diagram and role of constituents.

2.1 Introduction

γ-TiAl alloys are of great interest in the aeronautics and aerospace industries, as they have a singular combination of mechanical properties such as [5]:

- High melting point, around 1500 ºC.
- Low density of 3.9-4.2 g/cm^3.
- High specific strength and moduli.
- Good resistance against oxidation and corrosion.
- Low diffusivity.
- High ignition resistance when compared with conventional titanium alloys.

Titanium easily dissolves other elements that depending on the number of valence electrons per atom of the alloy in question, tend to stabilize either the α or β phase [6]. The elements with less than four valence electrons per atom stabilize the α-phase. Thus, they dissolve preferentially into the α-phase, expanding their margin of existence, and at the same time increasing the temperature at which the α-phase is stable. Aluminium, oxygen, carbon and nitrogen are among the α-stabilizing elements. Elements with more than four valence electrons per atom stabilize the β-phase, producing a decrease in the transition temperature α–Ti → β-Ti (T β-transus). β stabilizing elements can be classified into two groups (Figure 2-1):

- β isomorphs: These have limited solubility in the α-phase while in the β-phase solubility is complete. Some of these elements are vanadium, molybdenum, tantalum, and niobium.
- β eutectoids: These have limited solubility in the β-phase and form intermetallic compounds by eutectoid decomposition of β. Some of these elements are manganese, copper, iron, silicon, nickel and hydrogen.

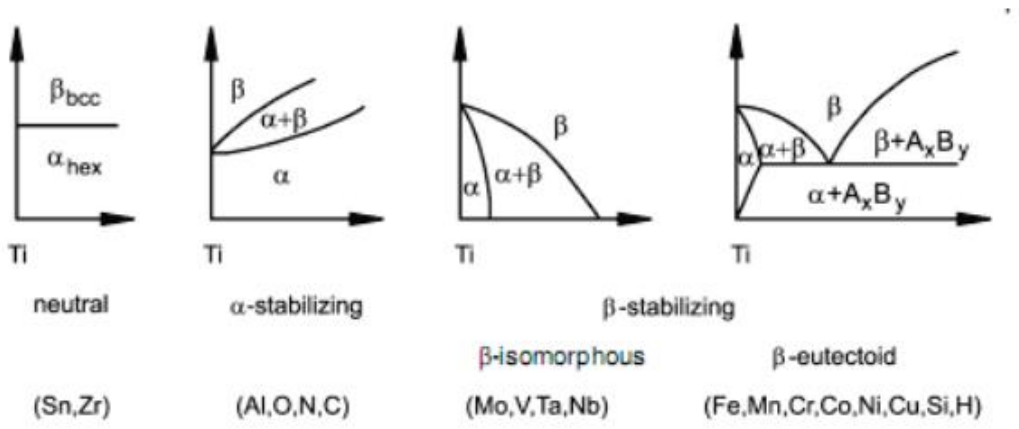

Figure 2-1. Effect of alloying elements on phase diagrams of titanium alloys [7]

In intermetallic TiAl alloys, three intermetallic titanium aluminides phases are known: α_2-Ti_3Al, γ-TiAl and $TiAl_3$. However, only α_2-Ti_3Al and γ-TiAl meet aeronautics requirements, and the latter has generated the most interest in the last decade due to its good and balanced mechanical properties. The phase diagram is set out in Figure 2-2.

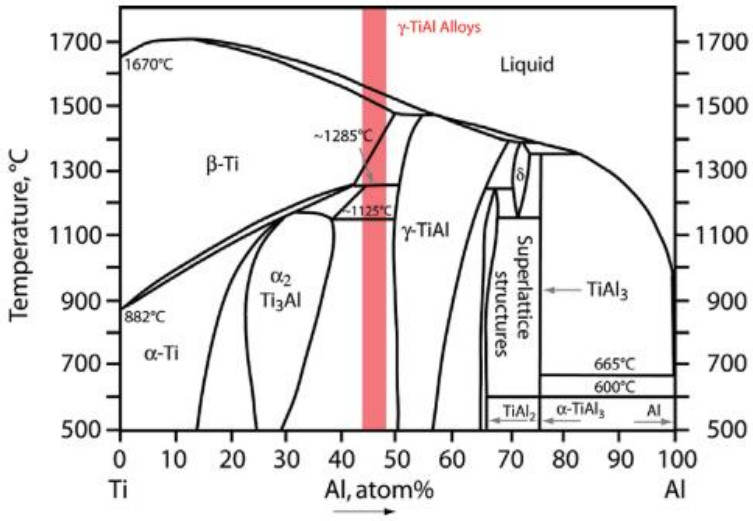

Figure 2-2. Ti-Al phase diagram, the red area represents γ-TiAl [8]

A brief comparison of properties of titanium aluminides, conventional titanium-based alloys and nickel-based superalloys is presented in Table 2-1 [9]. It can be concluded that γ-TiAl alloys have improved mechanical properties in comparison to conventional titanium-based alloys, providing excellent creep and oxidation resistance at high temperatures. When comparing conventional nickel-based superalloys to γ-TiAl alloys, the latter display superior specific strength at both room and high temperatures. However, this is at a cost of a reduced ductility and low damage tolerance at room temperature, which is one of the major drawbacks of γ-TiAl alloys [8].

Table 2-1. Properties of titanium aluminides, conventional titanium-based alloys and nickel-based superalloys [9]

Property	Ti-based alloys	Ti_3Al-based α_2 alloys	TiAl-based γ alloys	Nickel-based superalloys
Density, g/cm^3	4.5	4.1-4.7	3.7-3.9	8.3
Modulus, GPa	96-115	100-145	160-176	206
Yield strength, MPa	380-1115	700-990	400-630	250-1310
Tensile strength, MPa	480-1200	800-1140	450-700	620-1620
Creep limit, ºC	600	750	1000	1090
Oxidation limit, ºC	600	650	900-1000	1090
Ductility at room temperature, %	10-20	2-7	1-3	3-5
Ductility at high temperature, %	High	10-20	10-90	10-20

The chemical composition of γ-TiAl alloys has evolved, with the addition of different elements to improve creep and oxidation resistance. This is because binary Ti-Al systems do not meet the requirements for becoming an engineering material [10].

The composition of conventional engineering γ-TiAl or so-called 2nd generation is in at.% of: Ti-(45-48)Al-(1-3)(Cr,Mn,V)-(2-5)(Nb,Ta,W,Mo)-(<1)(Si,C,B). One example of these 2nd generation alloys is Ti-48Al-2Nb-2Cr, which is the most widely used γ-TiAl alloy employed in the turbine blade of aero-engines. This generation exhibits good workability, medium tensile and ductility properties, however the creep resistance is limited to application with a service temperature of up to 700 ºC.

Therefore, in a need to improve the high temperature properties, the 3rd generation of γ-TiAl was developed [11], with a chemical composition in at.% of: Ti-(42-46)Al-(0-10)(Cr,Mn,Nb,Ta)-(0-3)(Mo,W,Hf,Zr)-(0-1)(C,Si,B)-(0-0.5)(Rare Earth elements). An example of this generation alloy and subject of study of this research is the TNM (Ti-Al-Mo titanium aluminide), which displays superior strength and oxidation resistance, so creep and thermal stability at high temperatures is enhanced.

For the reasons presented above, the intermetallic titanium aluminide TNM alloy has been selected as the TiAl based-alloy subject to improvement. The present study aims to enhance its mechanical properties for structural applications (aeronautics) through the casting processing route.

2.2 Phase diagram and constituent phases

2.2.1 TNM basics

TNM alloys are γ-TiAl alloys with a nominal composition ranging between Ti-(42-45)Al-5Nb-1Mo-0.1B at.%. They present low density, high specific yield strength, high specific stiffness, good oxidation resistance, resistance against "titanium fire" and good creep properties at elevated temperatures [4].

The equilibrium phase diagram in the composition range of TNM alloys is set out in Figure 2-3, which is a quasi-binary cut through the multicomponent system xTi-xAl-4Nb-1Mo-0.1B, where the aluminium content is varied. It shows that for a nominal composition of 43.5 at.% of aluminium, the solidification range is about 100 ºC. Below the liquidus temperature, β-grains enriched in the refractory elements Nb and Mo start to precipitate in the melt. Once the alloy has completely solidified, the β-phase remains stable across a wide range of temperatures. Below the β-transus temperature, the α-phase starts to precipitate consuming part of the β-phase. Once the γ-solvus temperature is reached, the γ-phase starts to precipitate consuming part of the α and β-phases. Finally, the ordering reactions occur, first the ordering of the β to β_0 takes places, then the ordering of the α to α_2 at the eutectoid temperature. Therefore, depending on the temperature, TNM alloys can display five different phases without counting borides [12].

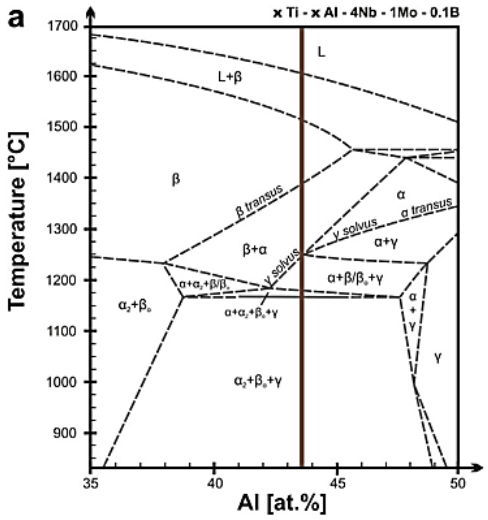

Figure 2-3. Quasi-binary phase diagram of the TNM alloy. The vertical line refers to the nominal composition of the alloy [12]

The solidification path of the TNM alloys is presented in Equation 2-1:

$$L \rightarrow L + \beta \rightarrow \beta \rightarrow \beta + \alpha \rightarrow \alpha + \beta + \gamma \rightarrow \alpha + \beta + \beta_0 + \gamma \rightarrow \alpha + \beta_0 + \gamma \rightarrow \alpha + \alpha_2 + \beta_0 + \gamma \rightarrow \alpha_2 + \beta_0 + \gamma \quad \textit{Equation 2-1}$$

Where L refers to liquid and the other letters refer to the constituent phases

Figure 2-4. Quasi-binary phase diagram of the TNM alloy. The vertical line refers to the nominal composition of the alloy [12]

Depending on the temperature there are different phases, two of which are disordered phases (β and α), and the other three ordered phases (α_2, β_0 and γ) [5].

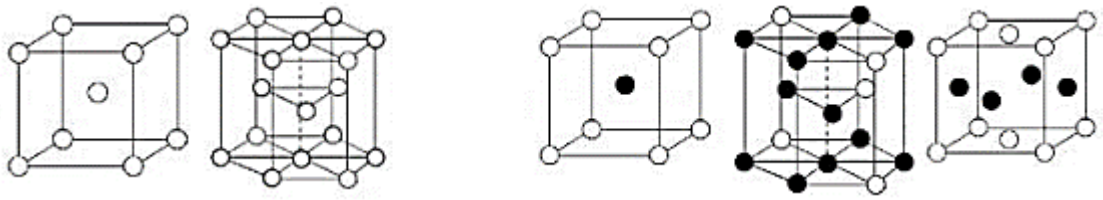

a) A2 **b) A3** **c) B2** **d) DO_{19}** **e) $L1_0$**

Figure 2-5. Crystal structures of phases in TNM alloys; a) β-phase, b) α-phase, c) β_0-phase, d) α_2-phase and e) γ-phase [5]

White circles represent a no fixed position of titanium and aluminium atoms

At room temperature, TNM alloys consist of a large amount of γ-phase and a small amount of α_2-phase, displaying residual amounts of β_0-phase [12]. Figure 2-6 shows the elemental composition of the phases presented in TNM alloys. It can be concluded that α_2 and β_0 phases have a slightly higher Ti content than the γ-phase, while Al is reduced in the latter. Nb is a strong β-stabilizing element and Mo even greater, so the β_0-phase is especially enriched in Mo. Interstitial elements like C, N or O are more likely to be found in the α_2-phase, due to the higher solubility of small atoms in the α_2-phase [13].

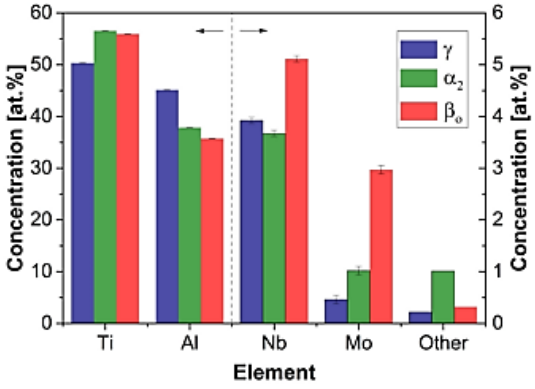

Figure 2-6. Phase composition of a TNM alloy in the homogenised condition [13]

Boron has a unique grain refinement effect, which is attributed to the presence of thermally stable borides that act as heterogeneous nucleation sites during the solidification and/or the solid-state transformation from β to α-phase [13] [1]. Borides observed in TNM alloys are mono-borides containing around 45 at.% of B. It is believed that their composition is off-stoichiometric, either by the creation of anti-site defects or vacancies, possibly due to the alloying elements. These borides show hardly any solubility of Al and a high amount of Nb, as Table 2-2 shows.

Table 2-2. Composition of TNM mono-borides [13]

Elemental at.%	B	Ti	Al	Nb	Mo	Other
TNM	45.1 ± 0.01	47.0 ± 0.01	-	6.8 ± 0.03	1,1 ± 0.04	0,0

2.2.2 TNM phase evolution

Liquid to β-phase transformation

For TNM alloys the morphology of the primary phase is equiaxial. This process consists of the following stages: nucleation, growth and mass transport, and the clash of grain fronts (Figure 2-7). During the nucleation stage, the first solid particles are formed once the temperature of the melt reaches the liquidus temperature. When the particles reach a size larger than the critical size they become stable nuclei and can grow from the melt. The formation of nuclei implies a liberation of energy in the form of latent heat, such a release of energy into the melting produces a slight increase of temperature, a so-called "recalescence" phenomenon. Later, the grains start growing, consuming the liquid until there is a clash between grains that prevents further grain growth. Indeed, the motion of grain boundaries is affected by the interaction of the boundary with imperfections of the crystal such as vacancies, dislocations, phase interfaces or external crystal surfaces. Finally, the solidification ends with the solidification of the rest of the melt [14].

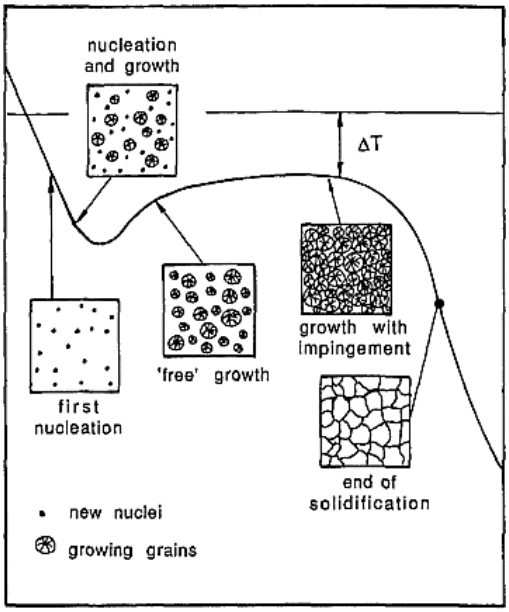

Figure 2-7. Solidification stages during equiaxial grain growth [14]

The cooling rate plays a key role in defining the amount and size of the newly born grains after solidification. At low undercooling, very few nuclei can overcome the energy to become stable nucleis. At high undercooling the driving force is high, but slow diffusion limits the nucleation rate. Therefore, the rate of stable nucleation exhibits a maximum as regards the undercooling. Nucleation from the melt can generally be divided into homogeneous and heterogeneous nucleation. The former refers to nucleation of solid particles directly from the melt, which is generally attributed to high energy for nucleation, and thus, a high undercooling is required. The latter refers to nucleation on the surface of a third phase, which is generally attributed to lower energy consumption and lower undercooling [15]. In TNM alloys, heterogeneous nucleation occurs on the surface of the mould as well as on borides, however homogeneous nucleation from the liquid is also possible.

Figure 2-8 depicts the precipitation of the β-phase from the liquid for the TNM alloy [12]. The TNM alloy solidifies primarily via the β-phase, below the liquidus temperature a certain driving force acts to create the lowest free energy in the system, which leads to the precipitation of large equiaxed β grains. This β-phase is enriched in the refractory Nb and Mo elements which have a high melting point. Indeed, boron may act as nucleation points for the β-phase reducing the grain size, hence an initial refinement during solidification can be achieved [16].

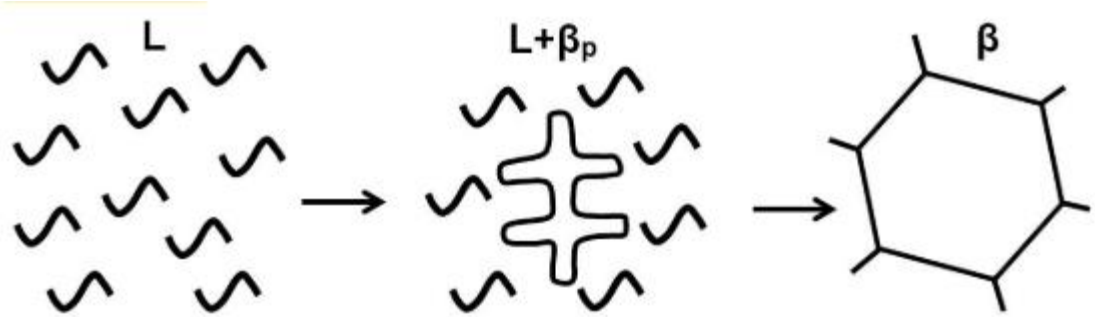

Figure 2-8. β-solidification pathway of TNM alloys [12]

Solid-states transformations

Once the β-transus temperature is reached, the disordered α-phase of the hexagonal close-packed (HCP) lattice becomes thermodynamically stable, consuming part of the β-phase. As a result, the α-phase usually nucleates from grain boundaries, triple points and on borides. An orientation relationship, called the Burgers orientation relationship, between the β parental phase and the precipitating α-phase takes place. During this process, the slip planes of the body-centred cubic (BCC) lattice convert into the basal planes of the hexagonal lattice, and the slip directions convert into the respective orientations. As a result, 12 different orientations of the α-phase are possible, and thus a significant grain refining effect is achieved.

However, once the γ-solvus temperature is reached, the lamellar α_2/γ-colonies start to precipitate. This implies that they are aligned only in directions given by the Burgers orientation relationship, which annihilates the effect of the previous grain refinement achieved during the β to α solid-state transformation, as depicted in Figure 2-9 [12].

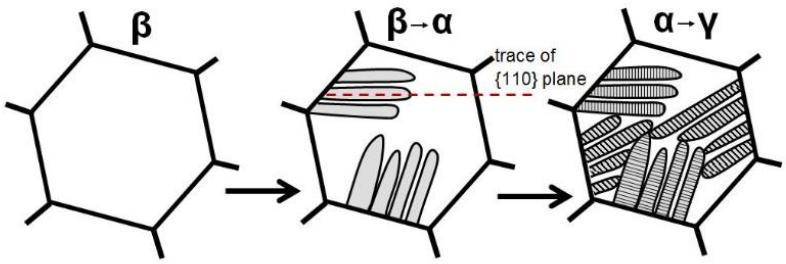

Figure 2-9. The sequence of solid-state transformation and lamellae formation in TNM alloys [12]

Another important fact is that the morphology of the α-phase is strongly dependent on the cooling rate. This is because high cooling rates favour fine Widmanstätten structures with a sharp and defined lath-like structure, while low cooling rates lead to equiaxed structures.

The cooling rate has also a significant role in establishing the temperature of transformation. In the case of the TNM-B1 alloy, the β to α phase transformation occurs at a temperature of around 1380 °C when the cooling rate is low. However, the cooling rate affects the transformation temperature (Figure 2-10), as well as the morphology of the precipitated phase [17]. Klein *et al.* confirmed that low cooling rates during phase transformation generate an equiaxed grain structure without the preferential direction of growth. In contrast, high cooling rates generate a structure in the form of sheets with crystallographic orientation relationship between the two phases. Therefore, to form a randomly oriented lamellar microstructure that provides improved mechanical properties, the cooling rate should stay low.

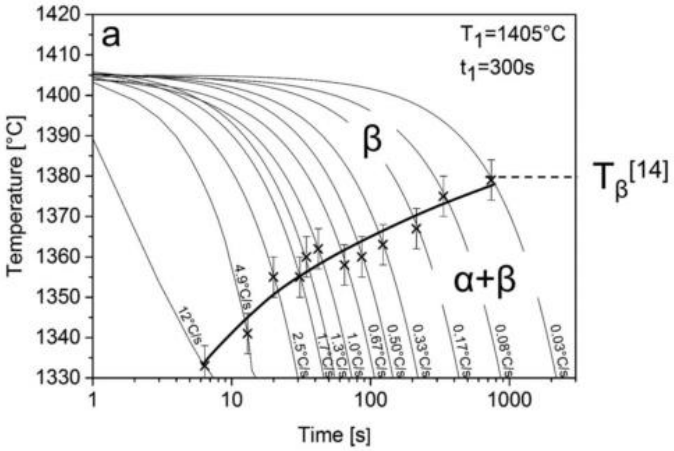

Figure 2-10. Effect of the cooling rate in the β to α temperature transformation [17]

γ-formation

The γ-phase starts to grow in the form of lamellae plates inside the previous α-grains as shown in Figure 2-9. The nucleation of the lamellae γ-phase is a diffusion-controlled process, so a higher cooling rate leads to a finer lamellar structure. This is due to limited diffusion of the elements between the α- and γ-phases. Indeed, boron additions favour heterogeneous nucleation of the lamellar γ-phase, resulting in a refined microstructure. This process is a precipitation reaction: $\alpha \rightarrow \alpha + \gamma$, where the formation of the γ-phase is governed by the Blackburn orientation relationship which can be written as Equation 2-2:

$$(0001)_{\alpha_2} // \{111\}_{\gamma}, < 11\bar{2}0 >_{\alpha_2} // < 1\bar{1}0]_{\gamma} \qquad \textit{Equation 2-2}$$

With regards to the orientation relationship, the close-packed planes and directions are parallel to each other, the precipitating γ-lamellae are also parallel to each other and perpendicular to the parental α-grains. The resulting grains consist of α_2/γ plates labelled as colonies, which display a lamellar microstructure [12].

At elevated temperatures, the γ-lamellae change their shape into a globular structure following a thickening of the plates of the α_2/γ colonies. In addition, a lens-shaped γ-phase is formed as a result of the solid-state transformation $\beta/\beta_0 \rightarrow \gamma$ [13] [18].

At sufficiently high cooling rates above the α-transus temperature, the formation of the γ-phase is suppressed when the cooling rate is higher than around 55 K/s. In this case, the microstructure at room temperature consists of highly supersaturated α_2 and β_0-phases. This supersaturated microstructure is thermodynamically unstable and transforms through the precipitation of the γ-phase during subsequent ageing treatments if sufficient thermal activation is available (around 700 ºC in TNM alloys). At low ageing temperatures, the γ-precipitates formed are very fine due to reduced diffusivity. As a consequence, the resulting fine γ-lamellae present an increase in strength and creep resistance. This is related to the formation of different interfaces acting as obstacles for dislocation movement. Nevertheless, decreasing interlamellar spacing leads to a decrease in ductility which is quite low. Thus a balance must be struck so as not to precipitate overly fine γ-plates [19] [17].

Figure 2-11 illustrates the effect of cooling rate on the formation of different phases in a peritectic γ-TiAl alloy. It can be observed that a higher Nb content requires a higher cooling rate to maintain the α_2-phase metastable while preventing the massive precipitation of the γ-phase [19].

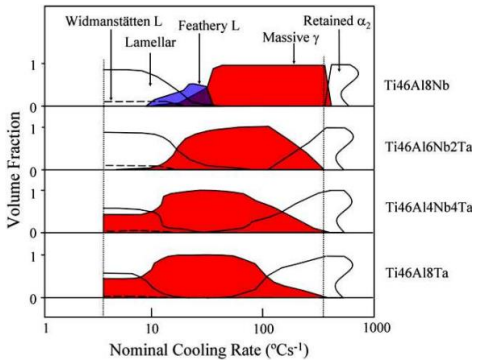

Figure 2-11. Effect of cooling rate in the resulting microstructure of different γ-TiAl alloys [19]

Other transformations

Cellular reaction

The cellular reaction is a discontinuous solid-state moving boundary reaction, characterized by an abrupt change in orientation between the matrix and product phases. It happens when the cooling rate is too high and the sample is aged or has been in service at high temperatures for a long period. In the case of TNM alloys, the cellular reaction follows the path of $(\alpha_2+\gamma)_{fine} \rightarrow (\alpha_2+\beta_0+\gamma)_{coarse}$. As depicted in Figure 2-12, it starts at the colony boundaries because both nucleation and diffusion is favoured in this region. The cellular reaction in TNM alloys yields low strength but significantly increases plastic fracture strain [12].

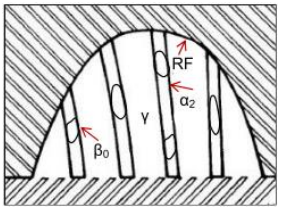

Figure 2-12. Cellular reaction representation [12]

Where: RF is the reaction front; α_2, β_0 and γ correspond to the phases involved

Ordering transformations

Ordering transformations in TiAl alloys must be considered because the mechanical properties change during ordering. These reactions cannot be suppressed by quenching due to the very short diffusion pathways. In the case of TNM alloys, the γ-phase is found to be stable at temperatures lower than the α-transus temperature, which is around 1285 ºC and is the most extensive phase [12].

Thus, ordering transformations depend on the different phases presented in the TNM. The α_2 and the β_0-phases are the ordered counterparts of the high-temperature α and β-phases. However, the γ-phase does not have a disordered counterpart, but rather decomposes during heating.

The ordering reactions are associated with changes in solubility. If the temperature is lowered below the ordering temperature of the α-phase, the aluminium content is too large to build the α_2–phase of equilibrium composition (supersaturation). This leads to two reactions, $\alpha_2 \rightarrow \gamma_{lamellar}$ and $\beta_0 \rightarrow \gamma_G$. The first reaction yields the formation of additional lamellar γ-phases. The second reaction leads to the formation of globular γ-phase on the colony boundaries, as the β_0 cannot dissolve the additional amount of aluminium.

2.2.3 Alloying elements

Depending on the alloying elements and their amount, the resulting microstructures varies and the material presents a different behaviour. Thus, the most important elements for TNM alloys are analysed as follows.

Boron

Alloying with boron is a typical procedure to improve the mechanical properties of TNM alloys, as this refines the microstructure. However, the grain refinement mechanism associated with boron additions is not currently fully understood, and the two hypotheses proposed to date approach the phenomenon from different perspectives. The first states that grain refinement is achieved by primary nucleation of the β-phase on borides [16]. This is associated with boron contents above a critical value, which is compositionally dependent. For TNM alloys, this value is around 0.5 at.% of boron [20].

The second hypothesis relates to the grain refinement effect during the solid-state β to α-phase transformation. Boron acts as an inoculant for the α-phase during decomposition of the β-phase [20] [21]. This solid-state transformation is the most widely agreed-upon refinement mechanism. In general, the nucleation of the α-phase from the β-phase is difficult due to the low coherency at the interfaces. A large energy barrier therefore needs to be overcome in order to nucleate an HCP phase in a BCC matrix, and as a result, only a few α-variants nucleate from the β-phase grain boundaries. Therefore, boron is added to form borides that act as inoculants to help the α-phase nucleate on their surface, which refines the microstructure of the alloy [22].

As stated by Yang *et al*., for a β-solidifying γ-TiAl with a boron content of 0.1 at.%, borides are thin and straight. Increasing the amount of boron to 0.3 at.% leads to curvy borides that are precipitated in inter-dendritic areas. An amount of 1 at.% of boron leads to coarse, long and straight borides precipitated from the liquid as well as borides formed in the β-phase that are precipitated in inter-dendritic areas. The results of their study indicated that the morphology of the borides is composition-dependent, and that 0.5 at.% of boron is enough to refine the microstructure of the alloy given its low solubility in the β-phase [20].

Generally speaking, boron is added to TiAl alloys ranging from 0.1 to around 1 at.% depending on the aluminium content and cooling rate. It is expected that low aluminium content requires a small amount of boron to refine the microstructure. While the cooling rate is a key factor, this process of refinement is still not fully understood. Boron is most certainly beneficial for heat-treatments conducted at high temperatures, which is due to the retard grain coarsening of the borides by pinning the grain boundaries. Another benefit is that boron promotes the formation of a lamellar microstructure ($\alpha \rightarrow \alpha + \gamma$) against massive transformation ($\alpha \rightarrow \gamma_m$), through heterogeneous nucleation of the interlamellar γ-phase [23]. From the above, it can be concluded that boron has a positive effect on alloying TiAl alloys. However, the precipitation of the desirable boride must be ensured, as their shape has a significant impact on the mechanical properties of the alloy. Hence the crystallography of Ti-Al-B-X must be studied.

The equilibrium Ti-Al-B-X phase diagram displays three intermediate compounds: TiB (B27 and B_f), Ti_3B_4 (D7b) and TiB_2 (C32). Ribbon borides: TiB (Bf) exhibit a preferential direction of growth and thus achieve a foil shape. The blocky borides: TiB (B27) do not have a preferential direction of growth, but a mixture, so they achieve a thick, straight shape [21]. The two typical types of borides in TNM alloys are monoborides TiB with B27 (blocky-type) and Bf (ribbon-type) crystal structures. These monoborides display metal-boron (MB) stoichiometry and contain around 45 at.% of boron, with around 5-10 at.% of niobium and almost no aluminium [13] [24]. However, they differ in the following ways:

- Blocky borides (B27) provide nucleation points for the α-phase and are not detrimental to the elastic limit. In addition, they are beneficial for refining the microstructure. They are associated with slow cooling rates during solidification and no segregations [25] [22] [26].

- Ribbon borides (B_f) are detrimental because they do not help to nucleate the α-phase and reduce the elastic limit (due to debonding between boride-matrix interfaces with cracking along the interfaces). This is a consequence of the large β-boride interface, which may act as a crack initiation point. They are associated with high cooling rates during solidification [25] [22] [26].

Blocky boride in TNM alloys contain around 45 at.% of boron and their composition is off-stoichiometric as a result of the creation of anti-site defects or vacancies due to the alloying elements [13]. TiB in a Nb-containing TiAl is frequently present as a mixture with Nb in nano-lamellar forms of TiB/Nb, rejecting aluminium.

As regards stability, the blocky boride is stable, while the ribbon boride is metastable [27]. There is evidence that both types of borides are present in TNM alloys [16] [20] [13]. Thus, ribbon borides are most likely formed under non-equilibrium conditions, which are associated with fast cooling rates during solidification.

Niobium

Niobium is a crucial element for the enhancement of high-temperature strength and oxidation resistance. This improvement of the oxidation resistance is achieved by reducing the oxygen transport towards the interior of the TiO_2 oxide scale. To do so the diffusional processes are reduced, which have a greater effect at high temperature, particularly during the HT and service temperature. This increases the strength and creep resistance of the α_2/γ-lamellae at high temperature, and is related to a rise in the activation enthalpy for deformation when Nb is increased in the alloy [1].

However, if the content of Nb and other β-stabilizing elements is too high, mechanical properties at high temperatures are worsened due to the generation of too much β-phase. The β-phase has lower creep resistance and strength at high temperature than the lamellar microstructure, but it is necessary to achieve the desired solidification pathway [3] [28].

Molybdenum

Molybdenum is a much stronger β-phase stabilizing element and promotes the formation of a smaller grain size than only alloying with Nb [3]. It is also beneficial for the shaping process, as small additions of molybdenum stabilize the disordered β-phase at high temperatures, and thus the equipment used during the hot work of these alloys is similar to the conventional set ups [13]. This stabilizing effect of the β_0–phase by destabilizing the ω_0-phase helps prevent several problems associated with the low ductility and brittleness of the ω_0-phase.

Therefore, Mo helps prevent the transformation from the β_0 to ω_0 phase which can occur during the ageing treatment [29]. The nucleation of nano-scaled ω_0 precipitates can occur in TNM alloys below around 825 ºC even under air-cooling conditions, and is driven by the formation of the precursor ω'' (Figure 2-13). During this process, nucleation of ω_0 particles takes places via lattice distortion of the original β_0 to form the precursor ω''. The subsequent collapse followed by the disordering of the single layers of the ω'' leads to the formation of the first ω_0 nucleus. Finally, the growing process of the ω_0 is governed by the distribution of Mo into the β_0 matrix [30].

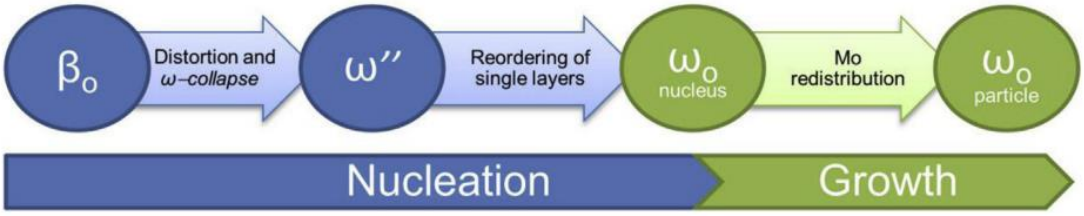

Figure 2-13. The ω_0 formation sequence

2.3 Conclusions

This section has established that intermetallic TiAl alloys have high specific strength and good corrosion resistance. They have the potential to substitute the heavier nickel-base superalloys in LPT blades, even though they present limited ductility at room temperature. However, not every γ-TiAl alloy is suitable for use in engineering materials. In this regard, intermetallic titanium aluminides can have three phases: α_2-Ti_3Al, γ-TiAl and $TiAl_3$, but only α_2-Ti_3Al and γ-TiAl have the properties required in aeronautics.

Recent decades have seen continuous development in the chemical composition of γ-TiAl alloys, to improve creep and oxidation resistance, as binary Ti-Al systems do not meet the requirements for becoming an engineering material. This has led to the third generation of TiAl alloys, in which the intermetallic β-solidifying γ-TiAl TNM alloy is one of the most promising, presenting high strength and creep resistance, as well as oxidation resistance up to 750 ºC.

TNM alloys feature the following solidification pathway: $L \rightarrow L + \beta \rightarrow \beta \rightarrow \beta + \alpha \rightarrow \alpha + \beta + \gamma \rightarrow \alpha + \beta + \beta_0 + \gamma \rightarrow \alpha + \beta_0 + \gamma \rightarrow \alpha + \alpha_2 + \beta_0 + \gamma \rightarrow \alpha_2 + \beta_0 + \gamma$. This alloy is characterized by a solidification entirely via the β-phase. During this process, once the liquidus temperature is reached, β-grains enriched in the refractory elements Nb and Mo start to precipitate on the melt. Once the alloy has completely solidified, the β-phase remains stable across a wide range of temperature. Below the β-transus temperature, the α-phase starts to precipitate consuming part of the β-phase. At the γ-solvus temperature, the γ-phase starts to precipitate consuming part of the α and β-phases. Finally, the ordering reactions occur, first the ordering of the β to β_0, and then the ordering of the α to α_2 at the eutectoid temperature.

Alloying elements play a key role in the final properties and TNM alloys are alloyed with Nb, Mo and B.

Boron helps refine the microstructure achieving improved mechanical properties, however the grain refinement mechanism associated with boron additions is not currently fully understood. The most widely accepted hypothesis is that boron acts as an inoculant for the α-phase during decomposition of the β-phase. However, the precipitation of the desirable boride must be ensured, as their shape has a significant impact on the mechanical properties of the alloy. In TNM alloys, two types of borides can be precipitated depending on the chemical composition and in particular the cooling rate. One type of boride is the blocky type which is beneficial for grain refinement, and is associated with slow cooling rates. The other, labelled as ribbon boride, has an opposite effect. By precipitating large grains and promoting segregations, ribbon borides are related to high cooling rates.

Nb is a crucial element for the enhancement of high-temperature strength and oxidation resistance, which is achieved by reducing the oxygen transport towards the interior of the TiO_2 oxide scale.

Mo has a stabilizing effect of the β_0-phase by destabilizing the ω_0-phase, and helps prevent several problems associated with the low ductility and brittleness of the ω_0-phase.

In general, there is a lack of knowledge regarding solidification cooling rate values in conjunction with the chemical composition of the type of boride precipitated. Therefore, this research seeks to provide a quantitative approach to the effect of the solidification cooling rate on the type of boride for the selected TNM alloys.

Chapter 3

3 Mechanical Properties and Alloy Characterisation

In this chapter, the material properties of TiAl alloys are examined. Firstly, providing a background to the more specific mechanical properties, and the basic knowledge required for the microstructure.

Then, the TNM-0.1B master alloy is characterised, analysing its microstructure to identify its main characteristics. Key points are analysed in-depth and the process variables to be acted upon are defined. This ensures that the new components manufactured in the as-cast state present a suitable microstructure, once the problems arising from the material/process have been addressed.

3.1 Deformation mechanisms

TiAl alloys can have many different structures, including fully lamellar and duplex structures. The fully lamellar structure is known for its high strength and poor ductility, as it contains mainly γ/α_2 lamellar colonies. In contrast, the duplex structure exhibits lower strength and better ductility, owing to the presence of a mixture of both single globular γ-phase and γ/α_2 lamellar colonies. As TiAl alloys are designed to be used in high-temperature environments such as the turbine blades of aircraft, investigating the deformation mechanism of both the single γ-phase and γ/α_2 lamellar colonies at elevated temperatures is especially critical.

The plastic strain of γ-TiAl based alloys subjected to a wide range of temperatures has been reported to be mainly caused by the softer γ-phase through dislocation motion and mechanical twinning. This is the case irrespective of whether the alloy has a lamellar or equiaxed microstructure [31] [10].

Plastic deformation of TiAl alloys results in lack of ductility, as the high-temperature yield strength is strongly dependent on grain orientation. The deformation mechanism of TiAl alloys is typically controlled by the movement of dislocation at very high temperatures. Indeed, plastic deformation of γ-TiAl can also occur by mechanical twinning. Thus, a general feature of the deformation of γ-TiAl alloys is that only one or two slip systems are being activated under most conditions. This means that a small number of slip systems is being activated, resulting in significant constraint stress that may be developed during strain. Besides, the contribution of superdislocations to deformations is not significantly enhanced at elevated temperatures, but by the effect of ordinary dislocation glides [10]. As a result, deformation of the lamellar microstructure occurs mainly by superdislocations.

In summary, various deformation mechanisms may contribute to the plastic deformation of TiAl alloys, including perfect dislocation glides with Burgers vectors b= 1/2 <110], b=1/2<112] and b=<011], and, $1/6<11\bar{2}]$ {111} order twinning [32].

The plastic incompatibility between α_2 and γ-lamellae has a significant effect on the stability of the lamellar microstructure during creep at a temperature of BDT. In addition,

many slip systems are activated in the γ-phase during creep at temperatures around BDT, but a few slip systems are also activated in the α_2-phase. As a result, a significant plastic deformation incompatibility between α_2 and γ-lamellae happens. This increasing plastic incompatibility improves the coherency strain of α_2/γ lamellar interfaces, resulting in an accelerating dissolution of α_2 lamellae in which Dynamic Recrystallization (DRX) occurs [33].

Dynamic Recrystallization

The BDT for TiAl alloys is in the range of 650 to 820 ºC. When loaded below the BDT, the deformation mechanism of a TiAl alloy with a fully lamellar structure is similar to that of one loaded at ambient temperature. When loaded above the BDT, DRX occurs in the fully lamellar TiAl alloy during hot deformation. This results in the abundant formation of recrystallized fine γ-TiAl phase grains. Once enough recrystallized grains have formed, the ductility of the TiAl alloy increases greatly, due to the sliding and rotating of the grain boundary. Below the BDT, the primary deformation mechanisms of TiAl alloys are twinning and dislocation movements.

DRX in the lamellar γ/α_2 structure process undergoes the following stages. At the initial deformation stage, abundant nano-twins nucleate from the lamellar interface and terminate at the adjacent lamellar interface. Meanwhile, large amounts of dislocations generated from the γ-lamellas take place. With the increasing strains, a great number of dislocations pile up at the twin boundaries and lamellar interfaces. Upon continuous deformation, many dislocations continue to be absorbed, leading to the formation of subgrains. By increasing the misorientation between adjacent subgrains, the subgrain boundaries transform into refined grain boundaries and eventually achieve DRX (Figure 3-1).

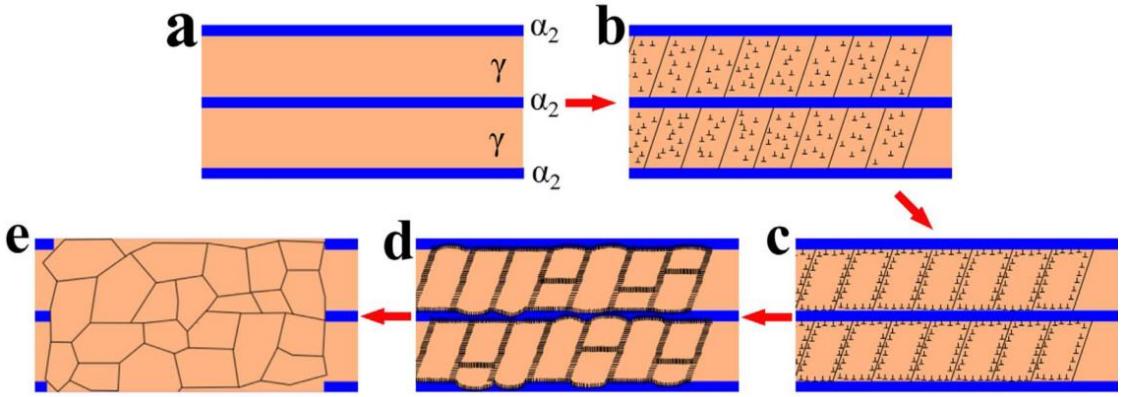

Figure 3-1 DRX process in the γ/α_2 lamellar colonies [34]

As regards the single γ-phase, dislocations can traverse the coherent twin boundaries at higher loading temperatures. The dislocation density within the nano-twins decreases with increased loading temperature. For this reason, fewer dislocation tangles can be observed in the single γ-phase in comparison to the lamellar γ/α_2 microstructure. This suggests that subgrain boundaries cannot be formed and no DRX occurs.

As dislocations and twins are inhibited at the lamellar interfaces, this results in the strengthening of the γ/α_2 lamellar colonies. At higher loading temperatures the better ductility of the single γ-phase indicates that the traversing of dislocations across coherent twin boundaries is more beneficial for ductility than the occurrence of DRX in γ/α_2 lamellar colonies [1].

With regards to crack initiation and propagation in both fully lamellar and duplex microstructures, the initiation and propagation of micro-cracks tend to be formed in the lamellar interfaces, but the mechanism is slightly different [33] [35].
In the fully lamellar microstructure, plastic deformation is mainly accommodated by the γ-lamellas in the γ/α_2 lamellar colonies. As a consequence of incoordinate deformation between the γ-lamellas and α_2-lamellas, micro-cracks tend to initiate and propagate along the lamellar interfaces. When the loading temperature increase to around 800 ºC, a severe occurance of DRX takes place near the lamellar colony boundaries. Within the γ/α_2 lamellar colonies, DRX also occurs, but it is less marked than at the lamellar colony boundaries.
As for the duplex microstructure, plastic deformation is mainly concentrated in the single γ-phase rather than the γ/α_2 lamellar colonies when loaded at around 600 ºC. Moreover, micro-cracks are initiated from lamellar interfaces within the γ/α_2 lamellar colonies or boundaries between the single γ-phase and the γ/α_2 lamellar colonies. Cracks propagate along with the lamellar interfaces or within the single γ-phase. When loaded at around 800 ºC, both single γ and the γ/α_2 lamellar colonies are elongated, and the initiation of micro-cracks along the lamellar interfaces takes place [34].

To summarise, plastic deformation of lamellar structure results in the loss of stability of the lamellar structure during creep above the BDT temperature, inducing premature creep failure and a drastic drop in mechanical properties. This is due to the thermal activation of the slip system in α_2 lamellae. However, creep below BDT temperature results in low creep strain and good mechanical properties.

3.2 Mechanical properties

In this body of research, the TNM-0.1B alloy has been chosen as the subject of study. The main advantages of this alloy is the low density of about 4.1 g/cm^3, a high specific elastic modulus of about 28 GPa, and a high specific tensile yield strength of about 140 MPa at 750 ºC. These properties refer to the after hot-working state, which is the typical processing route for TNM alloys.

The mechanical properties of γ–TiAl are strongly influenced by the final microstructure. Depending on the component properties required, different processing routes can be employed to engineer the microstructure, including heat treatments and chemical composition. Table 3-1 summarizes the effect of microstructure in the most important mechanical properties for TNM alloys [36].

Table 3-1. Assessment of microstructural constituents influencing the mechanical properties of TNM alloys [36]

Microstructural parameters	Suppression of grain growth	Yield strength at room temperature	Ductility at room temperature	Creep resistance
Small size of α_2/γ colonies	Negative	Strong positive	No influence/correlation	Negative
Fine α_2/γ lamellar spacing	No influence/correlation	Positive	No influence/correlation	Positive
Large fraction of α_2/γ colonies	Negative	Strong positive	Negative	Strong positive
$\beta_0(\beta)$-phase at colony boundaries	Strong positive	Positive	No influence/correlation	Negative
Globular γ-grains	Strong positive	Strong negative	Strong positive	Strong negative

Several studies claim that the limit of fracture toughness and creep strength is higher in nearly lamellar and fully lamellar microstructures than in a duplex microstructure [37] [38] [36]. This difference has been attributed to the α_2-laths that act as reinforcements and the morphology of the serrated grains [39]. Therefore, fully lamellar and nearly lamellar microstructures exhibit higher fracture toughness and creep strength as well as stable crack growth behaviour. Their ductility at room temperature however, is lower compared to a duplex microstructure [32]. The role of the constituents is significant because when the number of sliding systems is higher, the phase is softer. As a result, the β-phase is softer than the γ-phase, and the γ-phase is softer than the α_2-phase [40] [41].

Thus, to design a creep-resistant microstructure with an adequate ductility and strength at room temperature, a nearly lamellar γ microstructure is required. This microstructure should consist of spheroidal shaped α_2/γ-colonies with a colony size smaller than 100 µm, to increase the yield strength as well as ductility. Lamellar spacing within the α_2/γ-colonies should be in the range of 25 to 100 nm, to improve the creep properties. However, such small lamellar spacing also limits dislocation movement and therefore decreases the fracture elongation at room temperature. One option to compensate for the loss in ductility is to adjust to nearly lamellar γ microstructures with a certain amount of globular γ-grains. As a consequence of the softness of the γ-phase, dislocations can move relatively easily and mechanical twinning takes place [42].

Brittle-Ductile Transition temperature

γ-TiAl service temperature is usually below the BDT temperature. The BDT is a thermally activated process where stress is relaxed through plastic deformation rather than failure. In TiAl alloys it depends on several factors such as microstructure, chemical composition, loading rate and test environment. TiAl alloys exhibit high plastic deformation during creep at the temperature above BDT, but the maximum strain allowable in turbine blades is usually lower than 1%. Furthermore, creep life and creep strain show sharp transitions at the BDT temperature, so defining the proper service temperature for mechanical properties is of vital importance [33]. It is established that the BDT temperature for TiAl alloys is in the range of temperatures from 650 ºC to 820 ºC [34] [43] [33].

- When loaded below the BDT, the deformation mechanism of a TiAl alloy with a fully lamellar microstructure is similar to that of one loaded at ambient temperature. Thus, the primary deformation mechanism of TiAl alloys is twinning and dislocation movements.

- When loaded above the BDT, DRX occurs, resulting in the abundant formation of recrystallized fine γ-TiAl phase grains. This is the result of grain boundaries sliding and recrystallized grains rotating, which become the dominant deformation mode of the TiAl alloys.

Some examples of BDT temperature for γ-TiAl alloys are given in Figure 3-2 [33]. Figure 3-2 illustrates that BDT occurs between 780 ºC and 800 ºC for both alloys, but elongation values are markedly divergent as a consequence of their differences in the alloying elements. Thus, BDT is expected to be around the same temperature range in TNM alloys.

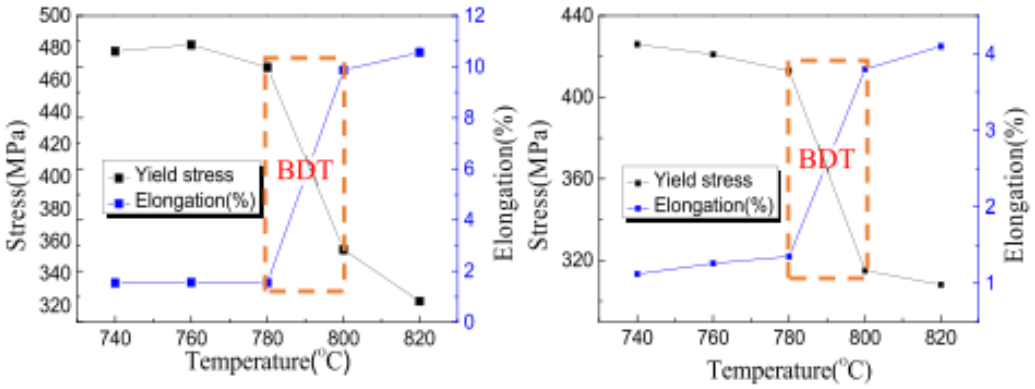

Figure 3-2. Tensile properties as a function of temperature; a) Ti-44Al-6Nb-1Cr and b) Ti-47Al-6Nb-0,1C [33]

Another variable key to understanding the mechanical behaviour of TiAl alloys is the establishment of the Brittle-Ductile Transition during Creep (BDTC). BDT is dependent on several factors, and therefore upon creep BDTC is commonly employed as the variable to analyse so as not to exceed the maximum 1% strain allowable for turbine blades. Figure 3-3 shows the drastic change the creep life and creep strain undergo during BDTC. It can be concluded that the BDTC temperature of nearly and fully lamellar structures is controlled by the α_2, with the activation of glide and dislocation movement inside the lamellae. Resulting in plastic deformation and formation of voids and cracks [33] [5]. Once again, this BDTC phenomenon is expected to take place at around 750 to 800 ºC for TNM alloys.

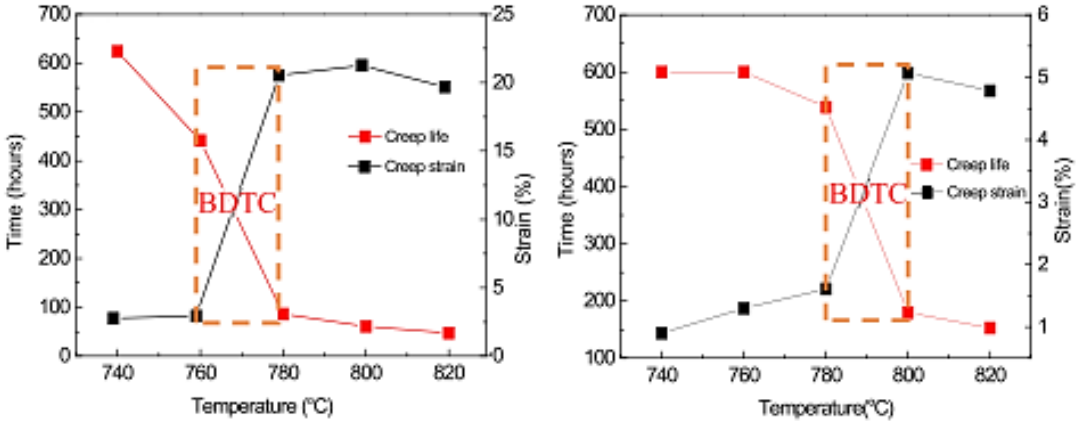

a) **b)**

Figure 3-3. Dependence of creep life and strain on temperature; a) Ti-44Al-6Nb-1Cr-2V and b) Ti-47Al-6Nb-0.1C [33]

In summation, when the TiAl alloy is in service for aeronautical components, it is critical that the BDT temperature (established between 650 to 820 ºC), is not exceeded. In this way, failure problems can be prevented. Chemical composition and heat treatments, play a significant role in raising the BDT to meet aeronautics requirements, through the formation of a suitable microstructure. To achieve good creep resistance with some ductility at room temperature a nearly fully-lamellar microstructure with no β_0 and few globular γ-grains in the colony boundaries must be formed. This is covered in more detail in Chapter 6, to obtain the required final microstructure combining HIP and HT.

3.3 TNM-0.1B master alloy characterization

Firstly, the commercial TNM-0.1B master alloy shipped from GfE was characterized. The master alloy was manufactured by Vacuum Arc Remelting (VAR) with subsequent centrifugal casting, then poured into a rotating casting wheel with steel moulds (more details on Section 0). A cross-section of the manufactured billet was analysed to understand the effect of the manufacturing process on its microstructure. This was necessary to be able to adjust the process parameters of the upcoming melting trials, and thus achieve the desired solidification conditions.

The as-received TNM-0.1B master alloy chemical composition is set out in Table 3-2. It has a relatively high amount of aluminium and low boron content, while the amount of Nb and Mo β-stabilizing elements are in the range of conventional TNM alloys (Ti-43.5Al-4Nb-1Mo-0.1B at.%).

Table 3-2. Chemical composition of the master alloy TNM-0.1B

Concentration (at.%)	Ti	Al	Nb	Mo	B
TNM-0.1B	50.4	44.5	4	1	0.1

3.3.1 Material preparation

To analyse the microstructure of the as-received TNM-0.1B master alloy, a slice of one of the supplied ingots (Figure 3-4a) was cut and a portion of around 25x10x5 mm was extracted (marked in red, Figure 3-4b). Three regions of interest were established from the obtained specimen (Figure 3-4c). The outer/surface zone corresponds to the area closest to the mould, and is thus subjected to the highest cooling rate, while the intermediate and the interior zones solidify at a lower cooling rate.

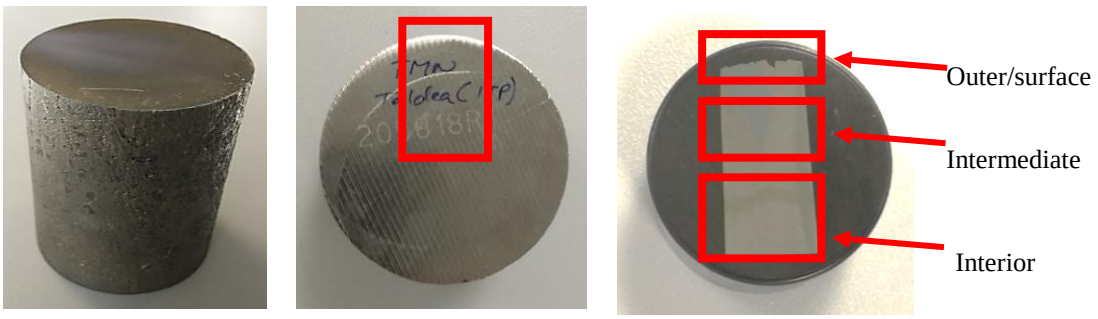

a) **b)** **c)**

Figure 3-4. Ingot of TNM-0.1B master alloy from GfE in the as-received state

The metallographic preparation began with grinding the surface to be analysed. The surface was then polished with synthetic diamond paste, and finished with a soft polish of colloidal silica solution to provide a low roughness without altering the microstructural constituents. Once the surface was conditioned, Scanning Electron Microscopy (SEM) was conducted in Backscattered Electron (BSE) imaging to analyse the microstructure. The BSE mode was used to obtain chemical contrast for better image quality, while the

image integration mode was employed to increase the image dynamic range, obtaining a sharper definition of the lamellar microstructure.

3.3.2 Microstructure analysis

Outer/surface zone (Fast cooling rate)

Figure 3-5 illustrates the typical microstructure of the sample surface that solidified inside a non-ceramic permanent mould. This surface was subjected to a fast cooling rate despite the relatively high thickness of the as-received billets. As a consequence of the high Heat Transfer Coefficient (HTC) between the molten titanium aluminide and the permanent mould, which is around 10 times higher than casting into ceramic investment casting moulds.

Many black coloured segregations (Figure 3-5a) can be observed in the vicinity of the surface containing a large number of entangled ribbon borides inside (Figure 3-5b). In these dark areas, the lamellae are not well defined, which may be related to a strong compositional variation. This trend is maintained up to several microns deep with a certain pattern in the morphology, and the amount of segregations is higher at a depth of around 2-4 mm from the surface (Figure 3-5c). This indicates that some sort of mechanism causing local disequilibrium due to the fast cooling rate has occurred (discussed in more detail in Section 5.3.2).

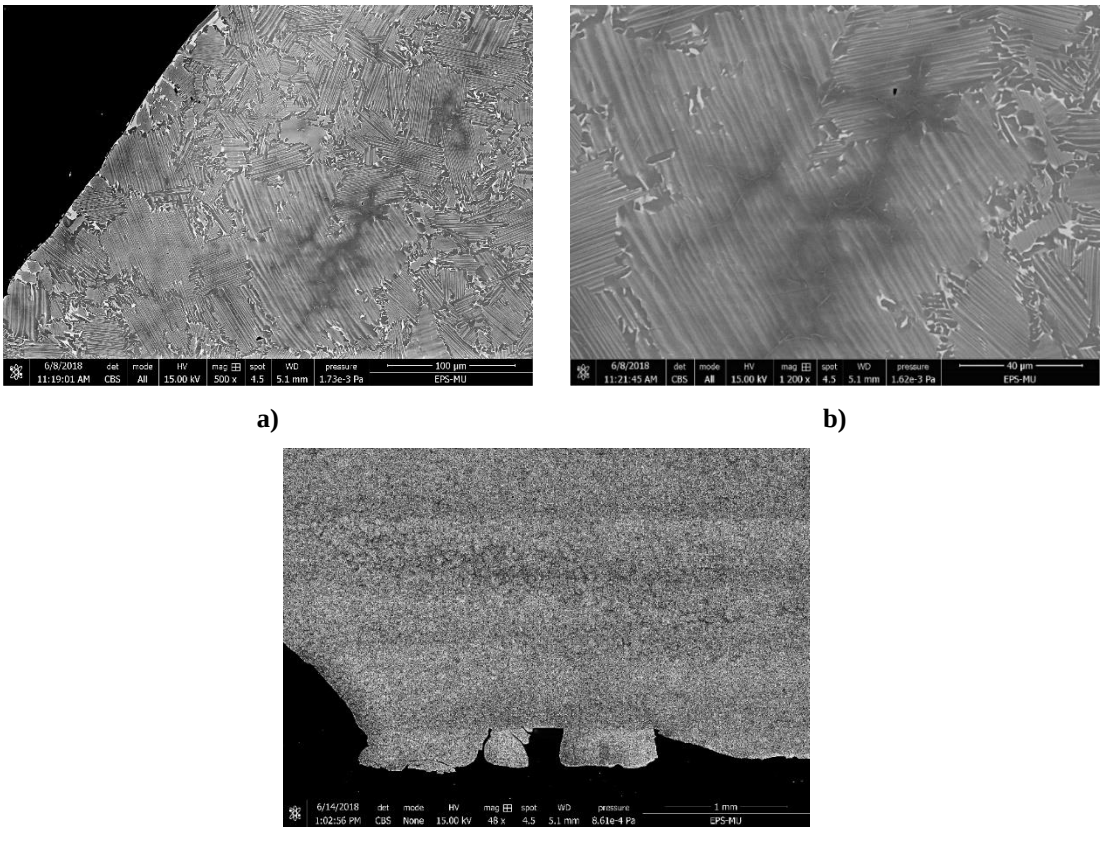

Figure 3-5. TNM-0.1B as-received from GfE, outer/surface zone; a) Segregations next to the surface, b) Ribbon borides inside the segregations and c) Reconstruction of the surface

To analyse the compositional variations and their association with the different precipitated phases, the Energy Dispersive X-Ray Spectroscopy (EDS) analysis was conducted. The EDS technique obtains information about the semi-quantitative local chemical composition through SEM. Table 3-3 presents the chemical composition of the various micro-constituents of the alloy from the selected points of analysis (Figure 3-6). It can be observed that the lamellae have a chemical composition similar to that of the bulk alloy, while at the grain boundary globular γ-phase and β-phase precipitates are detected. On the other hand, the dark areas indicate a high aluminium content and low content of β-phase stabilising elements (in particular molybdenum), as well as the presence of a large number of ribbon borides. This suggests that these dark areas remain liquid until the end of the solidification, and could be related to the combination of the fast cooling rate, the low melting point of aluminium, and the reduced solubility of boron in the β-phase.

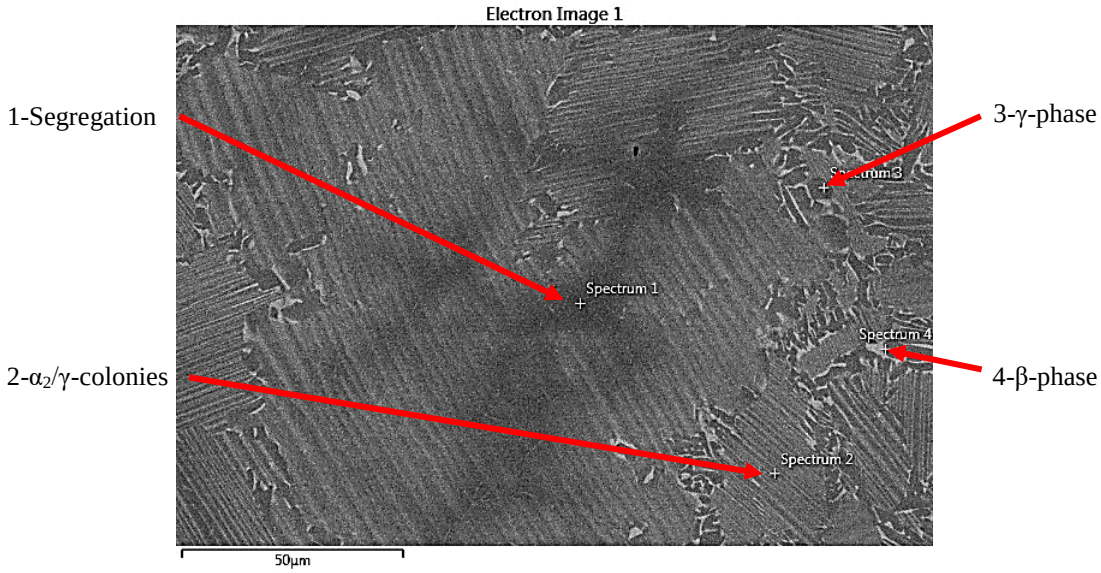

Figure 3-6. EDS, TNM-0.1B as-received from GfE, outer/surface zone

Table 3-3. EDS microanalysis, the semi-quantitative chemical composition of an outer zone of TNM-0.1B from GfE

Chemical composition / **Spectrum**	**Ti**	**Al**	**Nb**	**Mo**
1- Segregation	60.0	32.1	6.6	1.3
2- α_2/γ-colonies	60.2	28.4	9.5	2.0
3- γ-phase	59.2	29.9	9.4	1.4
4- β-phase	60.7	22.2	10.9	6.2

Intermediate zone (Medium cooling rate)

The analysis conducted in the intermediate zone reveals homogeneity in the distribution of the micro-constituents and lack of segregations. Only minor defects were detected in the form of microshrinkages due to the lack of HIPing. Overall, the zone exhibits beneficial blocky borides and a well-defined lamellar microstructure (Figure 3-7). It would thus appear that an intermediate cooling rate does not generate segregations, and prevents the formation of the detrimental ribbon boride.

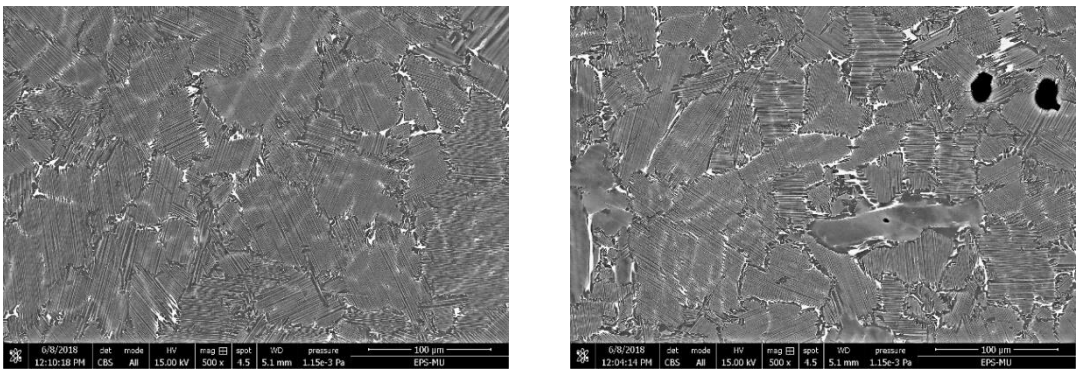

a) **b)**

Figure 3-7. TNM-0.1B as-received from GfE, intermediate zone; a) General and b) Some defects

Interior zone (Slow cooling rate)

Analysis of the interior zone reveals a fairly uniform microstructure (Figure 3-8a). However, it presents localized micro-shrinkages with segregations around them, as a result of a chemical composition gradient (Figure 3-8b). The interior zone is the area with the greatest thermal mass and therefore the last area to solidify, so aluminium and boron which are rejected from the melt tend to be enriched. As dendritic microshrinkages are formed by the contraction suffered by the liquid metal during solidification, this could validate the hypothesis that the last regions to solidify correspond to the areas where segregations are potentially promoted. The rest of the surface shows homogeneity without the presence of segregations or ribbon borides, due to the low cooling rate of the interior zone.

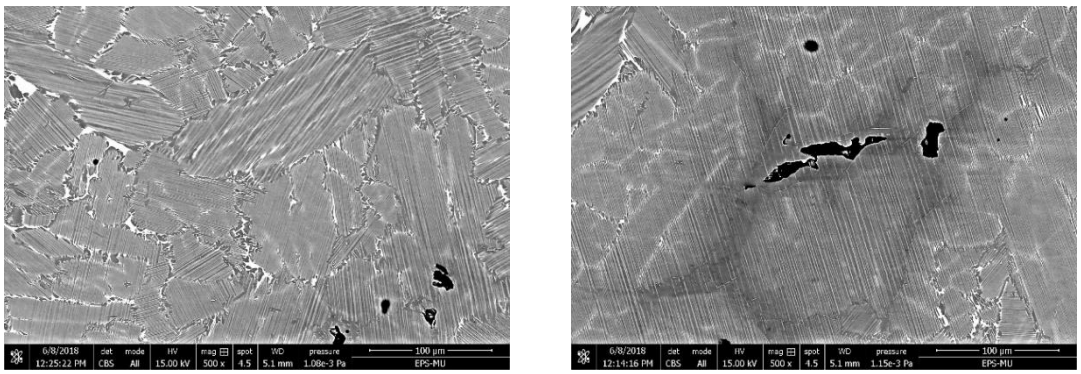

a) **b)**

Figure 3-8. TNM-0.1B as-received from GfE, interior zone; a) General and b) Segregations and microshrinkages

3.4 Conclusions

To conclude this chapter, it has been determined that γ-phase through dislocation motion and mechanical twinning is the main deformation mechanism in TiAl alloys at low temperature, with either lamellar or equiaxed microstructure. At temperatures above the BDT, DRX produces plastic deformation of the lamellar structure during creep, inducing premature creep failure and a drastic drop in mechanical properties. This phenomenon is related to the thermal activation of the slip system in α_2 lamellae. However, creep below BDT temperature results in low creep strain and good mechanical properties.

To prevent loss of mechanical properties when the TiAl alloy is in service, the component must not exceed the BDT temperature, established between 650 to 820 ºC for TiAl alloys. Chemical composition and HT, play a significant role in raising the BDT to meet aeronautics requirements. Through the formation of a nearly fully-lamellar microstructure with a minor amount of globular γ-grains in the colony boundaries, while β_0 should be eliminated. Therefore, to enhance the creep resistance and modify the mechanical properties in line with industry requirements, the chemical composition and processing window for cast TNM alloys must be adjusted.

The analysis conducted on the as-received TNM-0.1B master alloy, lent insight into the process variables to be acted upon. The outer/surface zone displays many segregations enriched in aluminium and containing a large number of entangled ribbon borides, resulting in a detrimental impact on the mechanical properties. In contrast, the intermediate and interior zones exhibit a homogeneous microstructure with few segregations, due to the lower cooling rate. To improve mechanical properties these results indicate that it is necessary to develop a homogeneous microstructure without segregations and ribbon borides. This can be achieved through the design of an appropriate chemical composition while cooling rate is controlled.

Chapter 4

4 The casting of TiAl Alloys

In this chapter, the main characteristics of manufacturing TiAl components are addressed. First, the ingot manufacturing process for the TNM master alloy is described, detailing the steps and key points. This is followed by an explanation of the technology employed for the casting of the master alloy, including a description of the facility set up.

Then, the design of the casting part and mould through computational simulation is discussed, as well as the operation window for the casting trials, which are detailed in Chapter 5.

4.1 Manufacturing Process

Intermetallic titanium aluminides have generated interest as lightweight structural materials, however it has taken considerable effort to be able to employ these materials in commercial applications. In the past, they were employed for vehicle components such as valves and pistons, and they are currently in use in LPT blades. These materials present challenging problems in manufacturing, such as the accuracy of chemical composition, microstructural homogeneity, and manufacturing of small size products. Indeed, close attention must be paid to aluminium, as its evaporation pressure is so high that achieving homogeneity is restricted to very controlled processing routes.

While the production of small-sized semi-finished can be challenging as well, both VAR and ISM or so-called CCIM can produce parts at and industrialized scale, delivering the desired requirements [44].

The industrial-scale processing routes established for wrought γ-TiAl-based alloys are summarised in Figure 4-1. The figure includes recent developments in the precision casting of TiAl alloys on an industrial scale, as well as additive manufacturing.

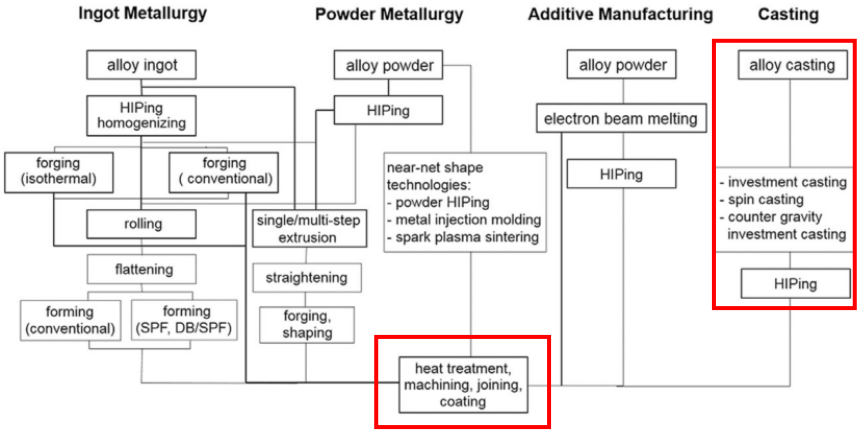

Figure 4-1. Manufacturing and processing routes established for wrought γ-TiAl-based alloys on an industrial scale [45]

Where: IM (Ingot Metallurgy), PM (Powder Metallurgy), HIP (Hot Isostatic Pressing), DB (Diffusion Bonding), SPF (Superplastic Forming), NNS (Near-Net Shape) [45]

The most commonly employed processing routes to manufacture TiAl alloys ingots are either by VAR or by Plasma Arc Melting (PAM). From the available production techniques, GfE has introduced an innovation (Figure 4-2), by combining VAR skull melting with centrifugal casting in permanent moulds. This processing route provides homogeneous and fine-grained microstructure suitable for both hot-working and investment casting operations [3].

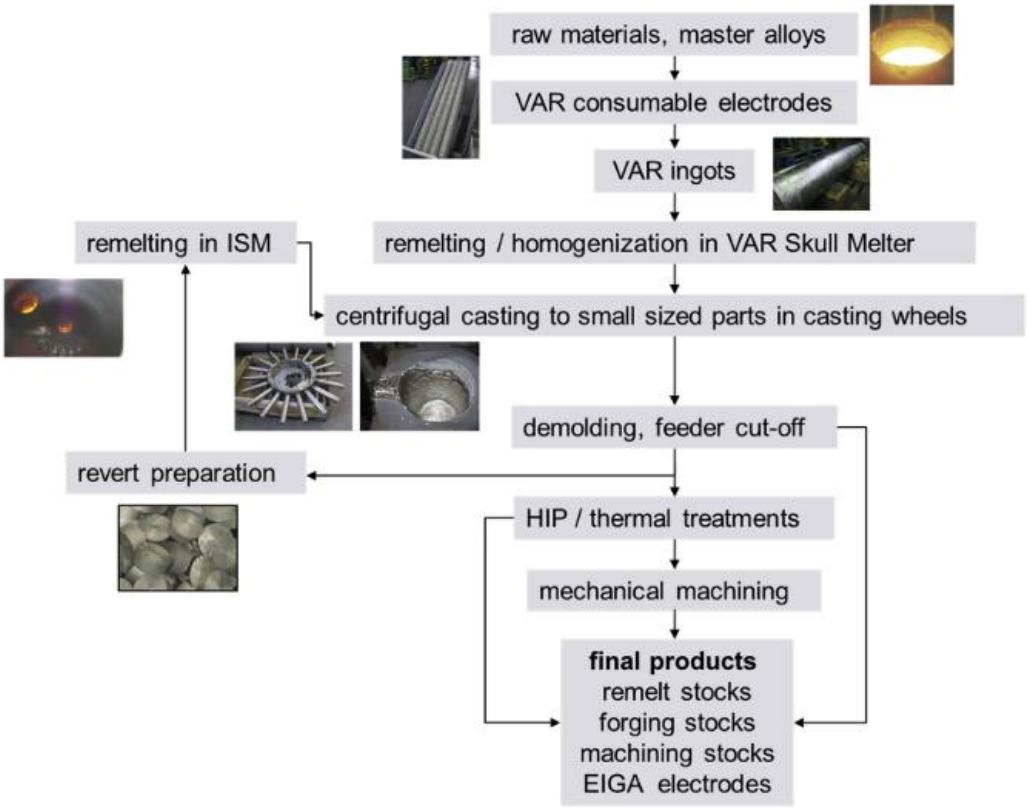

Figure 4-2. Technology chain for the production of γ-TiAl based semi-finished products, GfE [44]

Figure 4-2 shows how γ-TiAl is manufactured from raw materials to semi-finished products. The process begins with the production of the consumable electrodes made of titanium sponge, aluminium and master alloys, which is typically an alloy of AlNbMo. In this stage, all the ingredients are placed in the lower die and mixed so that every cross-section along the main axis of the compact consists of the same composition of alloying elements. The mixture is then pressed to form the consumable electrodes. Finally, the consumable electrodes are melted in a VAR under inert argon gas to produce the ingot diameter desired. This process may be repeated twice. As VAR cannot achieve the required homogeneity, VAR Skull Melting with subsequent centrifugal casting is employed, in which intensive stirring by electromagnetic forces causes the ingot to melt [44].

Finally, the melt is poured into a rotating casting wheel with steel moulds placed on the outer diameter, which ensures a casting of great soundness and homogeneity. The final product consists of cylindrical slugs. Scrap material, from removing the mould, feeder etc, is returned to the ISM.

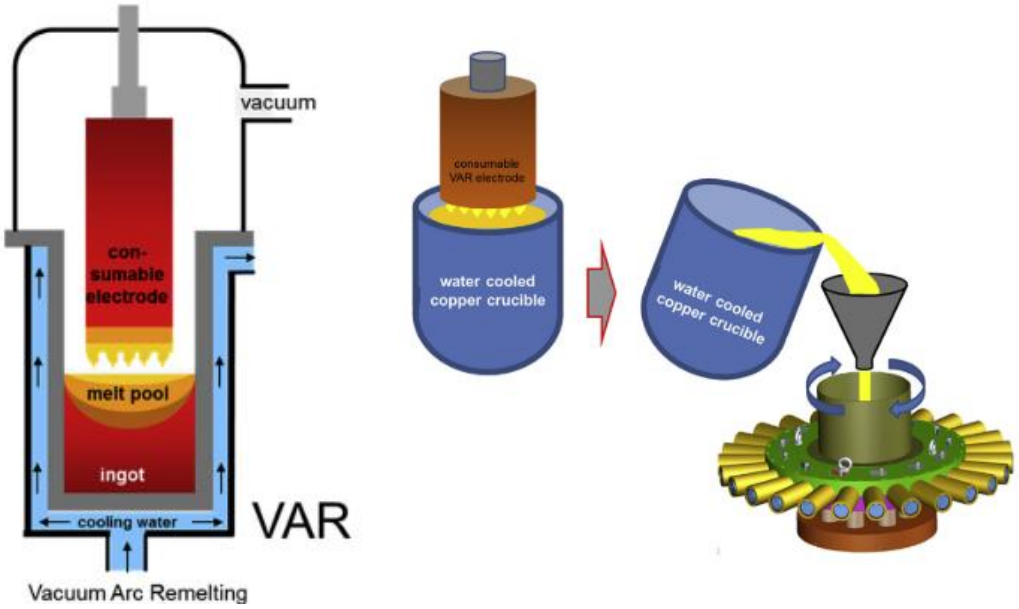

a) **b)**

Figure 4-3. Production of TiAl alloys, GfE; a) VAR and b) VAR Skull Melting with subsequent centrifugal casting in permanent moulds [44]

It is important to note that during the melting under vacuum at around 10^{-2} mbar, extensive evaporation of elements with a high partial pressure such as Al and Mn takes place. This results in the so-called black 'soot' on the chamber and 'flacky' deposits on the crucible (Figure 4-4). These deposits can be dragged in the mould during pouring, and thus it is necessary to melt under a partial pressure of argon to minimize the loss of those elements from the melt [46]. Nonetheless, use of this technique can lead to a depletion of some elements in the casting part which play a role in the final properties of the manufactured components. Indeed, given the narrow aluminium content to solidify the γ-TiAl alloy via β, the chemical composition must be adjusted.

Figure 4-4. Deposits of Al and Mn on ISM crucible after melting TiAl; black 'soot' on the chamber and 'flack' deposits in the crucible [46]

Once the final product is manufactured, HIP is applied to the cylindrical slugs to close the porosity arising from the casting. This process is mandatory to meet the technical requirements of aeronautical components. During HIPing, the components are subject to both elevated temperature and isostatic gas pressure in a high-pressure containment vessel. The HIPing process can eliminate internal voids and microporosity through a combination of plastic deformation, creep and diffusion bonding [47]. For TNM alloys, the typical HIPing parameters are 1200 ºC, 200 MPa, and 4 h, with subsequent surface cooling to room temperature [48].

The typical processing route for TNM alloys is to be hot-worked and machined to obtain the desired final geometry. This involves a great number of stages to achieve the final component. In this scenario, investment casting via CCIM is considered an appropriate process route to obtain final products without the need for further processing, as well as ensuring minimal variations in the chemical composition.

Finally, HT are applied to achieve the nearly fully-lamellar microstructure required for high strength and creep resistance, which is discussed in Chapter 6.

4.2 Cold Crucible Induction Melting

4.2.1 Physical Principle

CCIM technology or so-called ISM, involves melting and pouring the material in a vacuum, with the option of working in protective atmospheres. A crucible made of copper and internally cooled by water is used to minimize compositional variations between the charge and the crucible walls.

The crucible is formed by segments of copper separated from each other by an insulating material, which allows the magnetic field to penetrate and couple with the metallic charge assisted by the flux concentrators, as illustrated in Figure 4-5.

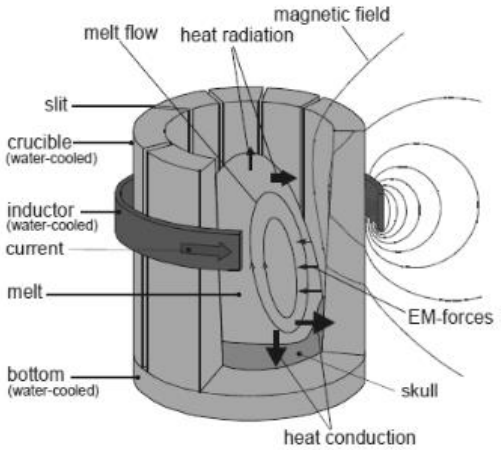

Figure 4-5. CCIM crucible [49]

The ingot is placed inside the crucible and as the alloy melts, a layer of metal between the crucible and the liquid metal called “skull” solidifies. This prevents the contamination of the liquid metal. Moreover, the flux concentrators ensure that the effective power applied is so high that the electromagnetic forces cause the molten metal to partially levitate. The resulting reduction in the exchange of heat between the liquid metal and the walls of the crucible causes a greater overheating of the metal. The stirring produced by the magnetic field has a further advantage of homogenizing the temperature and composition of the melt. When the charge is molten, it is poured into a ceramic or permanent mould that has the shape of the final component, thus requiring less surface-finishing operations [50].

The electromagnetic principle of the CCIM process is as follows: According to Ampere’s law, an alternating current that flows through a coil generates a time-harmonic magnetic field. Ideally, the magnitude of the magnetic field is related to the current by the proportionality factor μ_0, which is the constant permeability for space or vacuum. This magnetic field penetrates the segmented crucible through its slits. Using Faraday’s law, a voltage is induced in the charge, with an intensity proportional to the rate of change of the magnetic flux in the area encircled by the loop of the conductor and opposite in sign. The currents generated by the induced voltage, commonly called Foucault, dissipate the heat due to Joule effect. Moreover, the currents generated by this induced voltage give rise to a magnetic field that opposes the external magnetic field. At the same time, electromagnetic forces are also generated (Lorentz forces), which causes the charge to levitate, keeping it away from the crucible walls and thereby preventing the contamination of the molten metal. The Lorentz forces at this point are defined as the cross product of the electric current and the magnetic field vectors. Given that Eddy currents and their associated magnetic field are tangential to the material surface, the Lorentz force is always normal and pointing towards the surface [51] [50].

4.2.2 CCIM MU specifications

Mondragon Unibertsitatea (MU) is equipped with a semi-industrial scale CCIM facility capable of melting up to 1 kg of titanium aluminide in a vacuum or argon protective atmosphere Figure 4-6. Designed and manufactured by SECO / WARWICK, the equipment has a copper crucible, and the coil that surrounds the crucible has 3 rectangular turns and 18 magnetic flux concentrators. The power generator delivers up to 100 kW at 10 kHz (Figure 4-6). Table 4-1 summarizes the technical specifications of the MU CCIM facility.

a)

b)

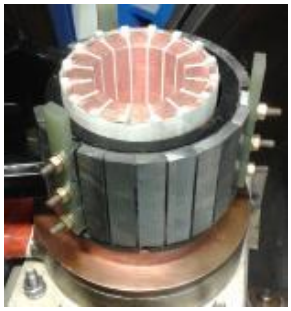

c)

Figure 4-6. MU CCIM facility; a) General, b) Vacuum chamber and c) Melt-box

Table 4-1. Technical specifications of the melting unit

Melting unit	
Maximum power [kW]	100
Maximum current in the coil [A]	2850
Frequency [kHz]	10
Maximum charge diameter [mm]	60
Maximum charge height [mm]	100
Type of atmosphere	Vacuum / Ar
Maximum vacuum pressure [mbar]	$(3.5).10^{-2}$

The moulding unit has a preheater inside the vacuum melting chamber so that the mould can be heated from 500 ºC to 1200 ºC. There is also an option to perform centrifugal casting by rotating the mould up to 350 r.p.m.

4.2.3 MU CCIM set up

To adapt the facility to melt TiAl alloys, some changes were made to the processing parameters and equipment. A new crucible, and a customized temperature recording unit that records the full range of solidification were installed inside the melting chamber. Improved melting conditions to maintain safety conditions were also established.

Charge temperature control

To measure the temperature of the melt an OPtris CTRatio 1MH two-colour-detector pyrometer was used. This technology measures the temperature of small, moving or even partially obscured metal objects within temperatures ranging from 700 ºC to 1800 ºC. It provides quick response time in the order of milliseconds to monitor fast-changing processes, and is thus ideal for casting.

Physical principle

A two-colour pyrometer detects thermal radiation of a measured object at two fixed closed wavelengths (Figure 4-7), and determine the maximum temperature of an area from the ratio of the density of the radiation. This helps to minimise the influence of the wavelength on the emissivity measurement of the target surface. To overcome this limitation the e-slope parameter is employed, which provides a correlation between the two wavelengths. This e-slope parameter can be determined by matching the temperature of the two-colour pyrometer with the real temperature provided by an immersion thermocouple [52].

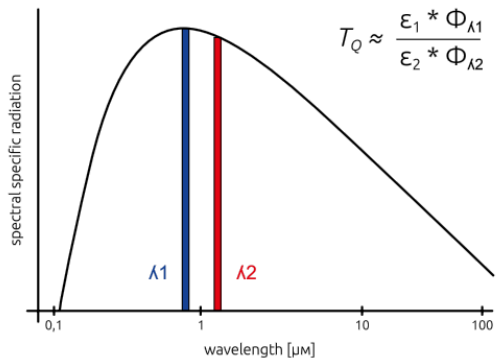

Figure 4-7. Two-colour pyrometers measurement [52]

In casting, fumes and dust are common which can cause signal degradation, and thus, mono-chromatic or single-colour thermocouples cannot provide accurate temperature measurements. However, two-colour pyrometer can measure the temperature even if the signal is weak, independent of the wavelength.

Pyrometer limitations

The pyrometer unit is located at the top of the vertical viewport to provide temperature measurements at the surface of the melt. The measured temperature value corresponds to the hottest temperature point of an area, known as a "spot size". The spot-size depends on the distance between the sensor and the measured surface (Figure 4-8). Since the sensor is located at a distance of around 1 m from the top surface of the charge, the spot size has a diameter close to 30 mm, which covers most of the surface of the ingot.

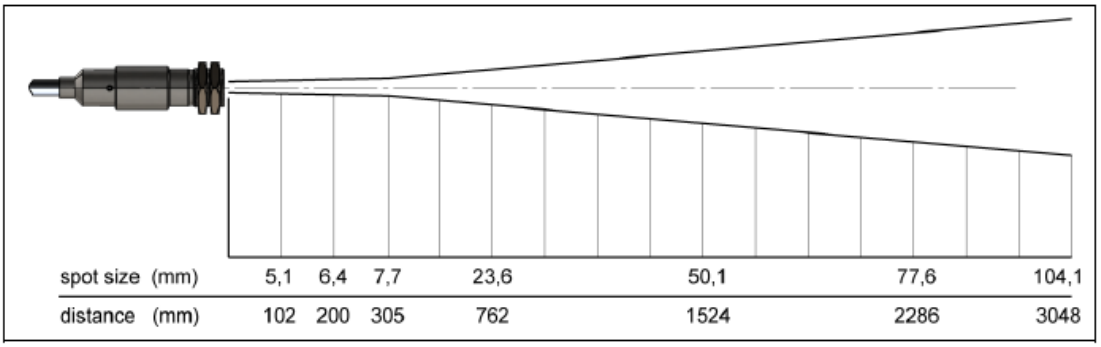

Figure 4-8. The spot size of the pyrometer as a function of the distance to the surface [51]

To properly measure the temperature of the charge, the pyrometer must be calibrated. This is due to the "skin" effect, in which the heating of the charge does not occur homogeneously throughout the volume of the ingot, and the zone of maximum temperature is located a few millimetres below the outer surface of the charge. As a result, there is heterogeneity in the temperature distribution of the charge, and the ingot melts from the bottom to the top, with the upper part being the last zone to melt due to cooling by radiation. To effectively characterize the overheating of the melt, it is therefore necessary to perform a prior calibration of the maximum temperature of the charge during heating. This procedure helps identify the thermal drift between the true value and the measurement obtained by the pyrometer.

Pyrometer calibration

To measure the true temperature value during the melting, the pyrometer must be calibrated. Therefore, the e-slope of the pyrometer was matched with the surface temperature provided by the immersion thermocouples, providing an e-slope value of 1.

The temperature distribution of the charge was calibrated according to the following procedure: Four holes were made in the TNM billet (Figure 4-9), and a K-type thermocouple was placed in each hole. The location of the thermocouples was defined considering the "skin" effect, based on the work of Chamorro *et al*. These thermocouples recorded the true temperature under stable heating conditions and were then compared to the values obtained from the pyrometer, thereby obtaining the correlation to be applied.

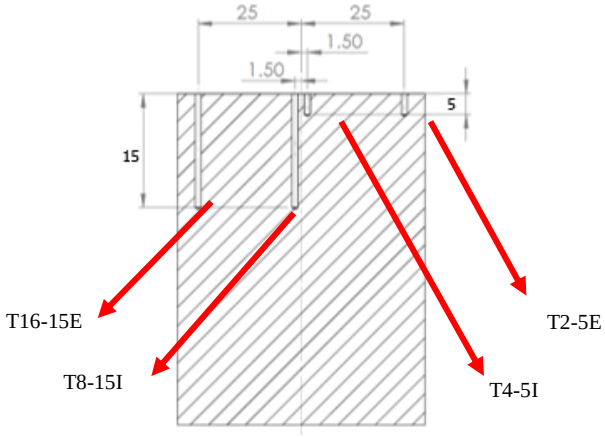

Figure 4-9. Location of the thermocouples inside the charge for the temperature calibration [51]

Figure 4-10 shows the change in temperature during the experimental heating calibration procedure. The trial consisted of applying a constant 20 kW step power until the temperature stabilized, paying attention to not exceed the maximum allowable temperature of the type-K thermocouples.

The thermal drift of the TNM-0.1B is set out in Figure 4-10 and Table 4-2. Once the temperature stabilizes (from minute 10 on), it is necessary to apply a correction value of 65 ºC over the value recorded by the pyrometer. This quantifies the true maximum temperature and measures the overheating of the melt, which helps identify the start of the melting. The maximum temperature of the charge was located at a depth of 15 mm below the surface and close to the ingot perimeter, in good agreement with Chamorro *et al*. [51].

Table 4-2. Average maximum temperature of each point of the charge, under stationary conditions

Pyrometer-True temperature	**Surface, 5mm exterior T2-5E**	**Surface, 5mm interior T4-5I**	**Interior, 15mm interior T8-15I**	**Interior, 15mm exterior T16-15E**
Average difference [ºC]	11	-79	48	65

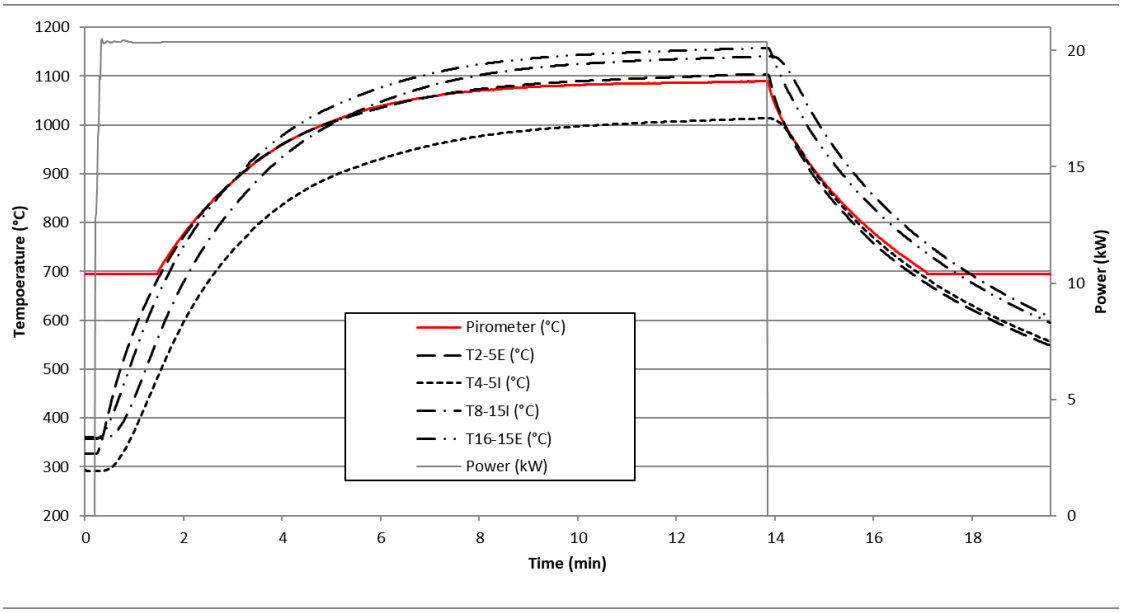

Figure 4-10. Evolution of temperature at each point of the charge

However, the fact that the conditions of the charge in the liquid-state differ from the conditions in the solid-state must also be taken into account. For this reason, this correction value may not always have the desired accuracy. Immersion thermocouples should be employed to overcome this problem, and thus the values for the thermal drift of the melt must be taken as an approach when the temperature of the melt is being measured.

Casting part temperature measurement

Given the high melting point and reactivity of the molten TiAl alloys, monitoring the melt temperature is challenging. K-type conventional thermocouples cannot be used as they can only measure temperatures at lower ranges. Indeed, as seen previously, the overheating of the ISM technology is limited, and quick response times and high-temperature measurements are therefore required. For this reason, a customized temperature recording unit was employed to measure the temperature of the melt as soon as the mould was filled.

To measure the temperature of the casting part, Omega naked C-type wire thermocouples were used. They provide fast and reliable temperature measurements as soon as the metal makes contact with the hot junction. This C-type thermocouple is formed by an alloy of wolfram and 5% of rhenium for the positive lead, and wolfram and 26% rhenium for the negative lead. Measuring temperatures ranging from 0 to 2320 ºC, with a tolerance value of 4.5 ºC or 1.0%, they are suitable for vacuum applications but not for oxidizing atmospheres which can lead to wire decomposition [53].

Physical principle

A thermocouple is formed by two different metals welded together at one end. The two wires meet at a junction, ensuring that there can be no electrical potential difference between the wires. This establishes a starting point from which thermoelectric voltage can be developed. Indeed, this emf (electromagnetic force) is developed from the measuring junction instead of by the junction.

Bearing in mind that each conductor is made of different chemical elements between wires, they respond in a different way to external stimuli (in this case, a temperature change). This implies that the emf change as local temperature changes, lower temperature results in a reduction in the emf of both thermoelements, but the amount of this reduction between wires differ due to their different compositions. This small net difference in emf change between the two dissimilar wires constitutes a thermocouple output signal. Therefore, selected wires with different known thermoelectric properties produce a useful electrical signal that varies with the temperature difference in a predictable way [54] [55]. Figure 4-11 displays the thermocouple principle, in which the cold junction compensated the emf changes between the thermocouple output signal and the conventional copper extension wire.

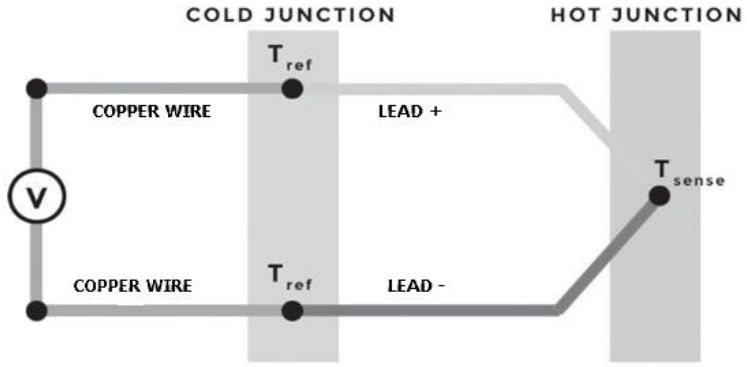

Figure 4-11. Thermocouple principle [54]

Thermocouples set up

To measure the temperature of the melt as soon as it reaches the mould cavity, a naked C-type thermocouple was placed in each step of the stepped mould. Each thermocouple wire was inserted into one of the holes of the double hole ceramic protection tube, in this way preventing contact between the wires outside the mould cavity. The wires were joined inside the mould to provide temperature measurements of the internal steps once the melt filled the cavity.

The C-type wires were connected to a signal converter unit, which recorded the temperature with National Instruments® instrumentation. These signal converters work as the cold junction, they receive an mV signal and deliver a 4-20 mA output current at 3 Hz through conventional copper wire. The signal converter unit was positioned in the vacuum chamber to facilitate operability, and was placed inside an aluminium box to protect the electronics from the intense magnetic field delivered by the coil, and to insulate against the heat from the heating chamber. Figure 4-12 shows the temperature measuring unit.

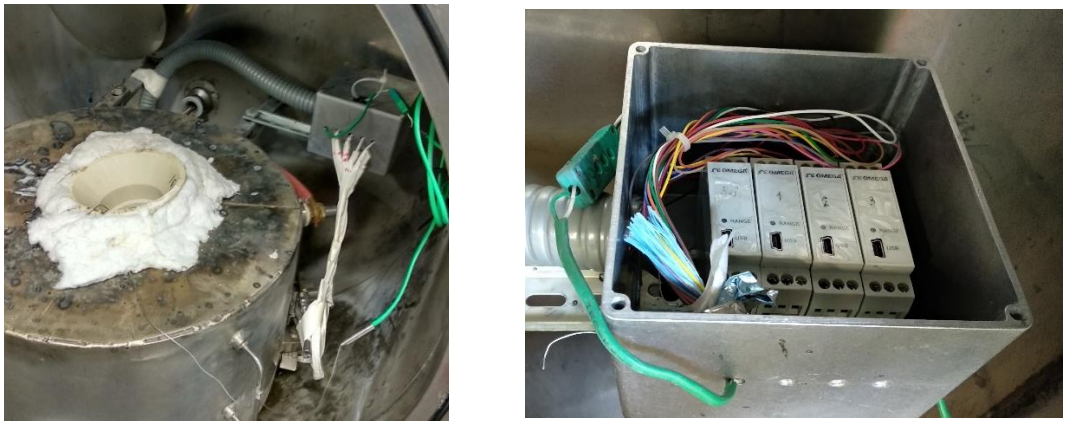

a) **b)**

Figure 4-12. Temperature measuring unit; a) Heating chamber and b) Signal converter unit

4.3 Mould Design and Casting Simulation

Investment casting is the typical processing route for highly reactive titanium aluminides as it is the most cost-effective production technique for complex thin-walled components, such as turbine blades. However, titanium alloy casting requires a crucible that does not react with the molten titanium. For this purpose, the ISM is used, but this technology has the disadvantage of providing low overheating of tens of degrees. Hence the pouring of the melt must be done quickly to avoid premature solidification before the metal fills the mould. For this reason, the pouring of the metal is restricted to top-gating (Figure 4-13a), which can generate and trap bubbles in the solidifying metal, requiring the use of HIP to remove those defects [46].

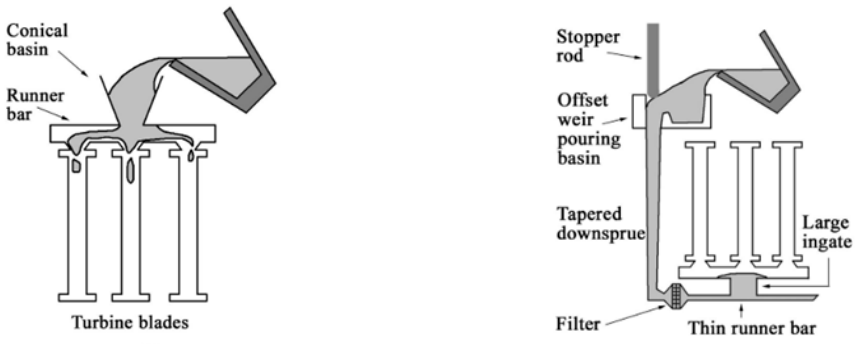

a) **b)**

Figure 4-13. Mould design for casting turbine blades; a) top-gating and b) bottom-gating

The present work focusses on analysing cooling conditions, as the microstructure of as-cast γ-TiAl alloys is strongly dependent on the cooling rate. To this end, the geometry selected was a stepped-mould with steps of different thicknesses, providing different cooling rates. The length and width of each step were designed to allow sample taking for mechanical testing.

Furthermore, some parts of a conventional gating system were omitted to try to guarantee the filling of the mould cavity (Figure 4-14). As a result, the runner system was simplified to minimize temperature loses.

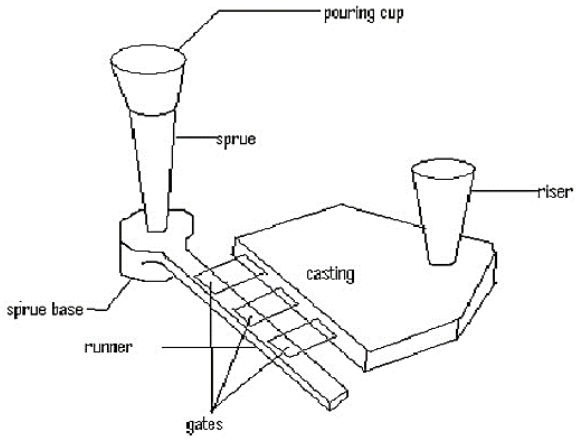

Figure 4-14. Conventional gating system

To validate the MU CCIM facility results were also simulated using is Flow-3D Cast®, chosen for its accuracy and ease of use.

This software aims to provide insights into the mould and casting part design to achieve a proper filling and solidification of the investment casting process. With the help of this Computational Fluid Dynamics (CFD) software, the solidification cooling rate was analysed to obtain an initial reference values.

4.3.1 Mould design and CFD set up

Given the low fluidity of molten titanium aluminides and the low overheating of CCIM technology, some strategies are required to successfully cast TiAl alloys. In addition to top-grating pouring (discussed in Section 4.3), increasing the overheating of the charge by melting under a relatively high argon partial pressure can also be beneficial. When compared to melting in a vacuum, this second technique can generate overheating of around 10 ºC [46].

Proposed geometry and initial sep up

In this research, both top-gating and melting under a relative high argon partial pressure were employed to improve the casting of TiAl alloys. As regards the gating design, a top-gating pouring locating the cast part with an angle of 45º to reduce turbulence during the filling was designed. An additional modification was that the sprue was designed to fit conventional pouring cups, but the runner system was not implemented to maintain the maximum temperature of the melt.

The casting part was designed with 4 steps of 2-4-8-16 mm thickness, respectively (Figure 4-15). The aim was to produce test specimens for mechanical testing while ensuring that enough melt is available to fill the stepped specimen. Thus, the length and width of the samples were of 100x25 mm while the thickness was set to 2-4-8-16 mm to generate different cooling rates, and analyse the resulting microstructures.

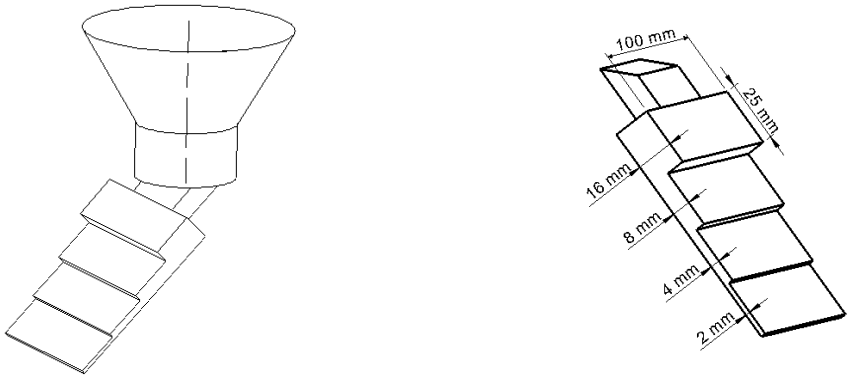

a) **b)**

Figure 4-15. CAD picture; a) Casting part and b) Stepped specimen

To ensure that the simulations were as close as possible to the investment casting process of the MU facility, the spatial distribution of each component of the CCIM within the melting chamber was defined in the computational simulation. To achieve accurate computational simulation results, customized thermophysical properties were also loaded into Flow 3D Cast® databases from the literature [56], and in situ experiments were conducted with Differential Scanning Calorimetry (DSC).

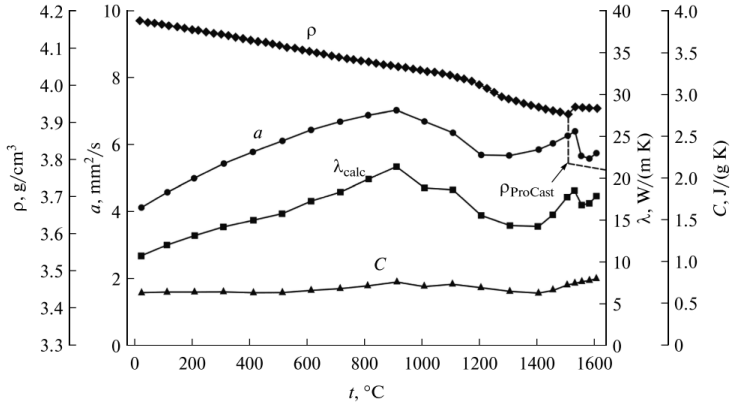

Figure 4-16. Thermophysical properties of master alloy TNM-0.1B [56]

The final step consisted of designing and running the simulation through Flow 3D Cast®, to obtain knowledge about the filling and solidification process. The computational simulation of the filling was analyzed to predict the premature solidification arising from the casting process, and the solidification cooling rate and cooling rate during phase precipitation was obtained. This helped to determine the expected solidification cooling rate during the experimental casting, as well as to correlate the cooling rate and the as-cast microstructure.

4.3.2 Filling process

The simulation of the filling process covers the pouring of the metal from the crucible to the mould, and involves the following stages. First, the casting part, mould, crucible and charge geometries are loaded in the simulation. Then, the process conditions are defined, and the filling simulation is ready to start. At the initial moment, the liquid metal is confined in the form of a meniscus shape due to the intense magnetic field generated by the coil. Once the power is cut, the meniscus collapses and then the crucible is tilted to facilitate pouring into the mould. Finally, the liquid metal enters the mould progressively until it is filled or premature solidification occurs, ending the filling simulation.

To obtain accurate results from the computational simulation, certain material-specific properties must be entered into the program, among the most important of these are the liquidus and solidus temperature, latent heat of solidification, and the HTC between the metal and the mould. However, this last HTC value is difficult to obtain experimentally, and is commonly measured through numerical simulation. In the present study values were taken from the databases built into the software.

Liquidus and solidus temperature, latent heat of solidification and specific heat were obtained from DSC analysis. Figure 4-17a shows the equilibrium solidification of the TNM-0.1B master alloy. It was determined that the liquidus and solidus temperature were of 1561 ºC and 1503 ºC, respectively, and the latent heat of solidification was 223 J/g. Figure 4-17b illustrates the temperature at which the different phase precipitations occur under equilibrium conditions. The α-phase precipitates at 1371 ºC, γ-phase at 1237 ºC , and the β_0–phase and α_2–phase at 1217 ºC and 1168 ºC, respectively. The cooling rate from the computational simulation was obtained at these equilibrium phase precipitation temperatures (Table 4-3), to correlate the cooling rate with the as-cast lamellar microstructure.

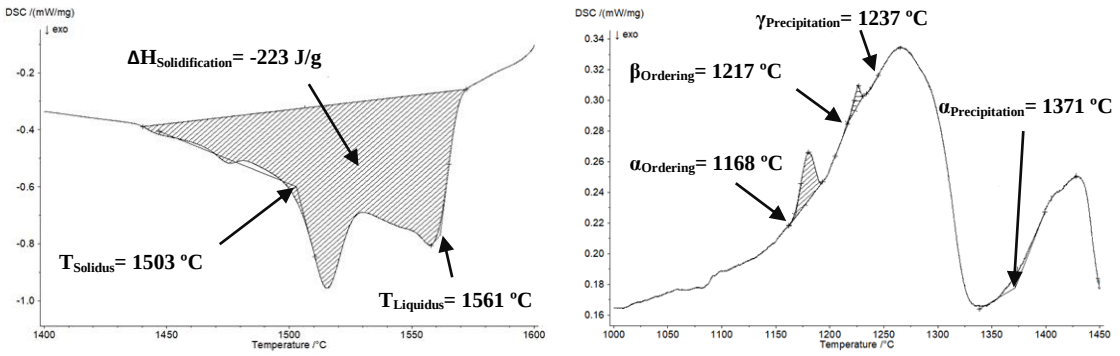

Figure 4-17. DSC TNM-0.1B; a) Solidification and b) Phase precipitation

Table 4-3. CFD prediction of the cooling rates during the phase precipitations of the TNM-0.1B

Phase precipitation cooling rate [°C/s]	2 mm	4 mm	8 mm	16 mm
α	65	29	12	7
γ	29	13	10	3

The pouring temperature was set to 1620 ºC because during previous trials the pouring temperature measured by the pyrometer was around 1600 ºC, while the corrected actual value was 20 ºC higher according to the previous calibration. The preheater, was set to 600 ºC to improve the filling of the mould and maintain industrial conditions.

The results reveal that the 4 and 2 mm steps were just filled, while 2 mm step exhibited limited misrun (Figure 4-18). Therefore, some strategies should be employed to ensure the mould filling during the experimental trials, such as melting under Ar atmosphere to increase the overheating, or increasing the mould temperature.

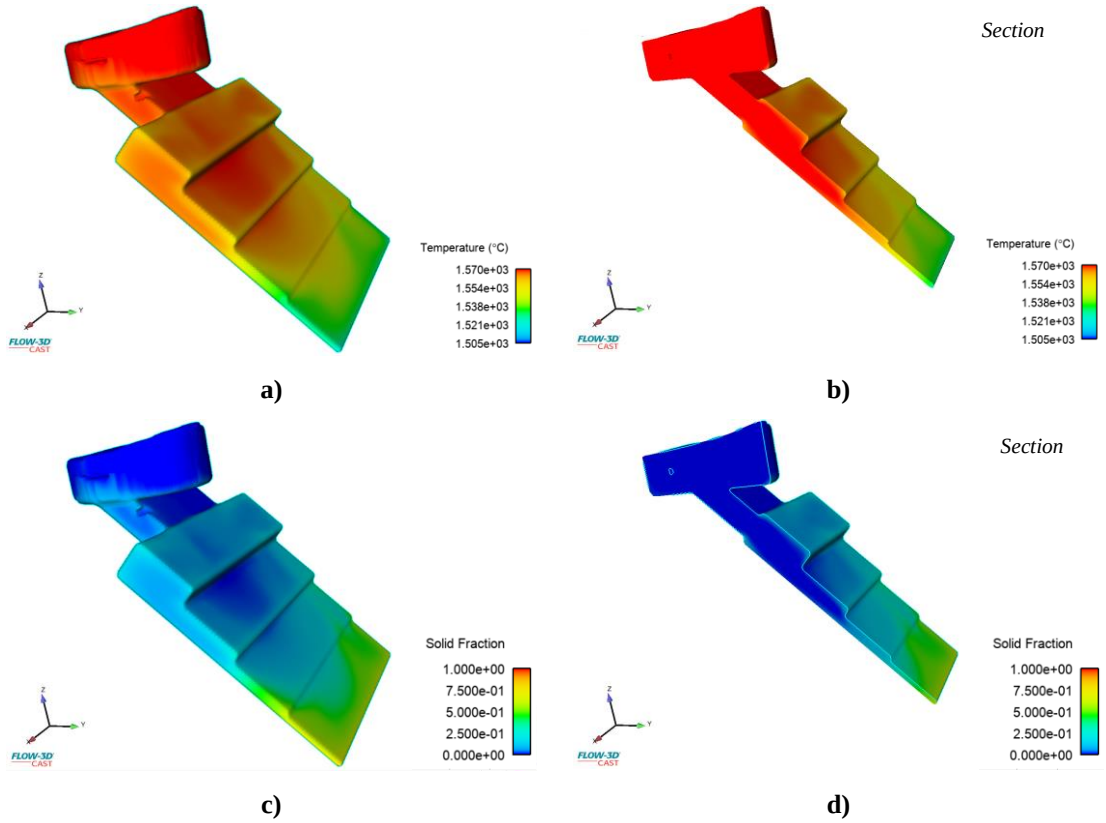

Figure 4-18. Flow 3D Cast filling; a) and b) Temperature distribution after the end of the filling simulation, c) and d) Section of the solid fraction after the end of the filling simulation

4.3.3 Solidification process

There are two key points to analyse during solidification. First, the defects arising from the casting process such as air entrainment, macroporosity, hot spots, etc. The second point is the solidification cooling rate of each step of the stepped mould, and thus the solidification cooling rate is correlated with the different microstructures to be obtained from the casting trials. This work focuses on the latter, as it seeks to correlate the cooling rate with the as-cast microstructure, while casting defects can be removed through HIPing.

The cooling rate of each step of the stepped-specimen was analysed through computational simulation to obtain a numerical approach. The solidification cooling rate was obtained from the middle of each step, taking the average solidification cooling rate from the liquidus to the solidus temperatures. Figure 4-19 shows the cooling curves and Table 4-4 summarizes the solidification cooling rates of the centre of each step of the stepped specimen. It can be concluded that both the 2 and 4 mm steps exhibited a cooling rate above 10 K/s while the 8 and 16 mm steps had a cooling rate below 10 K/s. These cooling rate values help correlate the microstructure with the cooling rate.

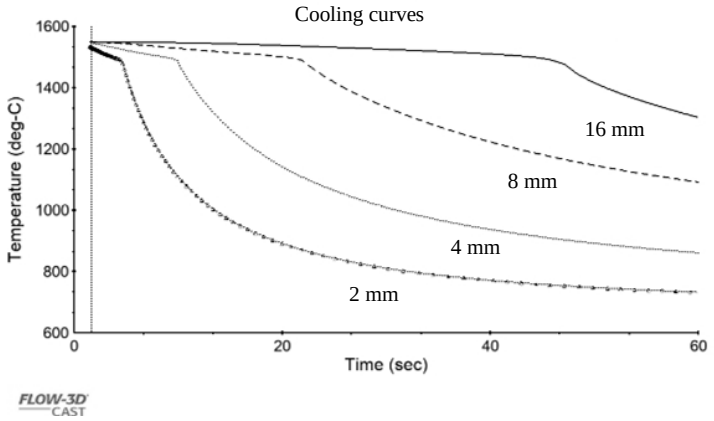

Figure 4-19. Flow 3D Cast, cooling curves of the stepped specimen with 2-4-8-16-mm thickness

Table 4-4. Flow 3D Cast solidification cooling rate of each step of the stepped specimen

	2 mm	**4 mm**	**8 mm**	**16 mm**
CFD Cooling rate [K/s]	24	11	5	2

4.4 Conclusions

To industrialize the manufacturing of TiAl alloys, the processing route requires accuracy of chemical composition, microstructural homogeneity and small product sizes. To meet the strict requirements of the TiAl manufacturing route, GfE has developed a production technique which combines VAR with ISM to cast small ingots of TiAl. While there are many technologies available to melt these TiAl ingots, CCIM (or ISM) was chosen for the present research.

To correlate the casting processing parameters with the as-cast microstructure, accurate tracking of the temperature during the melting and cooling of the metal must be ensured. Therefore, the skin effect was taken into account to measure with accuracy the molten metal temperature and the solidification cooling rate of the metal was tracked with fast responding naked C-type thermocouples.

To correlate the effect of different cooling rates in the as-cast microstructure and mechanical properties, 4 steps of 2-4-8-16 mm thickness with a length and width of 100x25 mm samples were used. The computational simulation results revealed the 2 and 4 mm steps presented a cooling rate of 24 K/s and 11 K/s, respectively. While the 8 mm step exhibited a cooling rate of 5 K/s, and 16 mm step of 2 K/s.

Chapter 5

5 Alloy Design

In this chapter, the development of a TNM based alloy optimized for casting is presented. For this purpose, the chemical composition of the TNM master alloy was modified and the casting process conditions adjusted, to obtain a homogeneous microstructure and the precipitation of the appropriate boride.

First, the effect of the alloying elements in the solidification pathway is analysed, with the purpose of narrowing the working processing window. Then, several chemical compositions containing varying percentages of aluminium and boron content are proposed, and the solidification cooling rate is analysed. These measures achieve a suitable as-cast microstructure, that with the application of subsequent HIP and HT processes, ensures improved structural mechanical properties (covered in Chapter 6). Finally, a formation mechanism for the different types of borides is proposed.

5.1 Solidification paths

Depending on the type and amount of alloying elements present in TNM alloys the solidification path can be via β-phase or peritectic. In intermetallic TiAl alloys with a solidification via β-phase (L → L + β → β → β + α → …) an isotropic structure, equiaxial grain, microstructure without texture and with little microsegregation is generated. When the solidification is peritectic (L → L + β → α → …) an anisotropic microstructure is created, with the presence of segregation and texture [23].

There is a transition concentration that leads from peritectic solidification to β-solidification, and this depends on the amount of aluminium and other alloying elements, which are determined by stabilizing the β-phase against the α-phase. From Figure 5-1, it can be concluded that the nucleation and growth of the β-phase produce a liquid enriched in aluminium and depleted in the β-stabilizing elements. This can lead to a change in the solidification pathway, in which peritectic reaction takes place by forming the α-phase straight from the melt [57].

Alloys with lower aluminium concentration than the critical value with no boron present a relatively isotropic but coarse microstructure. In contrast, boron-containing alloys with lower aluminium concentrations exhibit an equiaxial, fine and homogeneous microstructure. Thus, alloying with boron is certainly desirable in terms of microstructure. For aluminium contents above the transition concentration, there is also grain refinement through boron, but the lamellae colony size is generally larger than in alloys with below the critical aluminium content [37]. It can thus be concluded that the β-solidification pathway provides better properties than the peritectic solidification pathway.

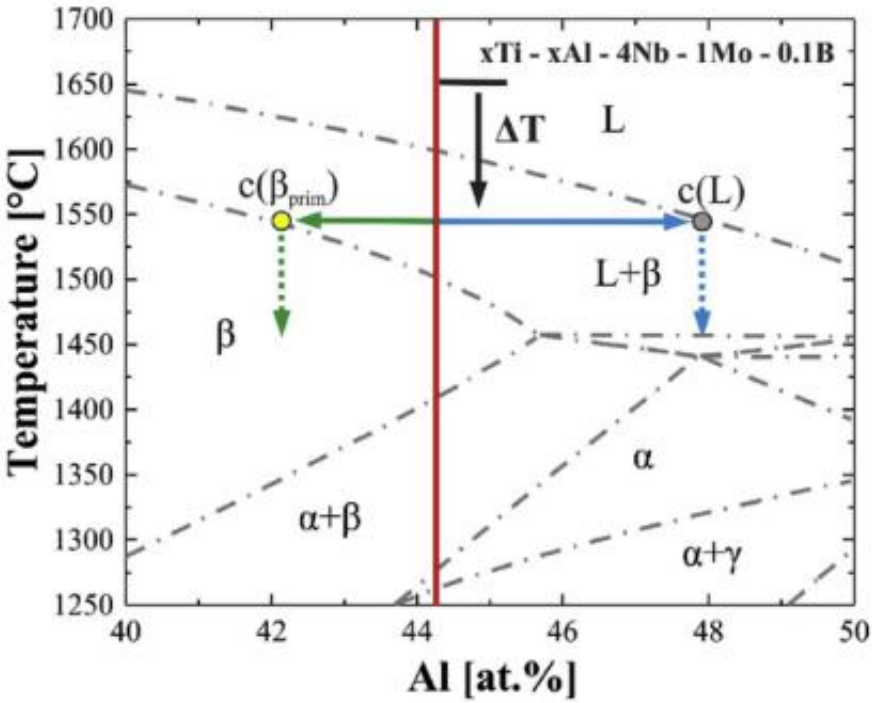

Figure 5-1. Detail of the quasi-binary phase diagram of the TNM alloy varying the aluminium concentration [57]

Where the discontinuous vertical lines represent the amount of aluminium in the β-phase and the melt respectively

5.1.1 Peritectic solidification path

The peritectic solidifying path takes the following route: L → L + β →… + α → …

In the peritectic-solidifying TiAl alloys, there is a shared growth of the α-phase with the primary β-phase during the solidification of the melt. Upon cooling, the α-phase grows over the β-dendrites and prevents nucleation of α from β. Titanium and other alloying elements that segregate to the β-phase are enriched in the dendrite cores, where the β-phase is finally transformed or remains stable as β_0-phase. Therefore, in binary peritectic TiAl alloys, the α-phase grows from the melt with a certain orientation to the heat flow direction and does not nucleate from the primary β-phase [58].

Peritectic solidification and low boron content

Liq. → Liq. + β(Ti) → Liq. + β(Ti) + α(Ti) → Liq. + β(Ti) + α(Ti) + (Ti, Nb)B → α(Ti) + (Ti, Nb)B

Figure 5-2 shows that the overall α(Ti) structure is well aligned in the direction of growth, and no grain refinement effect takes place. Ribbon borides form shortly after the peritectic onset [59] [58].

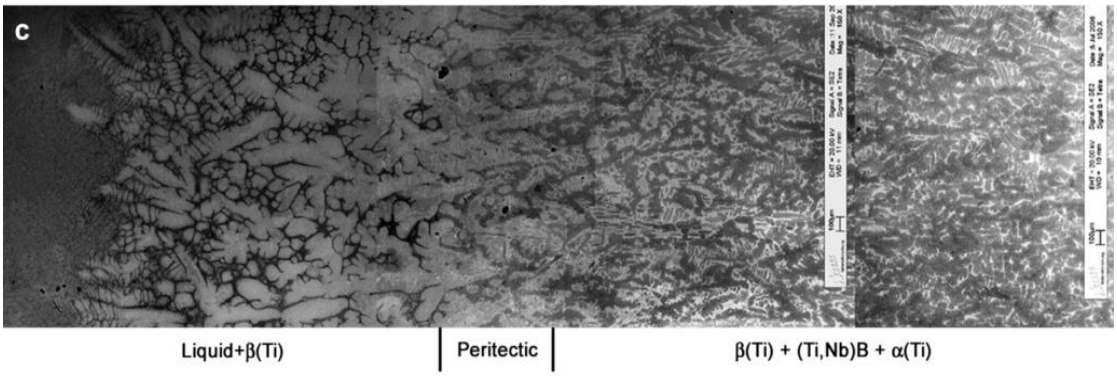

Figure 5-2. Sample Ti-43.2Al-5.4Nb-0.2B-0.2C water quenched [59]

5.1.2 β-solidification path

The β-solidifying path is as follows: L → L + β → β → β + α → …

In β-solidifying TiAl alloys, the widmanstätten α-plates are precipitated from the parental β-phase with different orientation relationships, resulting in a grain refinement effect. This leads to the segregation of titanium and niobium of the remaining β-phase [59] [58].

Solidification via β

Liq. → Liq. + β(Ti) → β(Ti) → α(Ti)

This alloy contains no boron and solidifies completely via β(Ti). Thus, large colonies of α(Ti) laths grow with a certain directionality through a process controlled by diffusion. This involves repartition of alloying elements, in which niobium is segregated positively into the remaining β(Ti), and aluminium negatively. As a result, β(Ti) dendrites grow closely parallel to the direction of solidification (Figure 5-3) [59] [58].

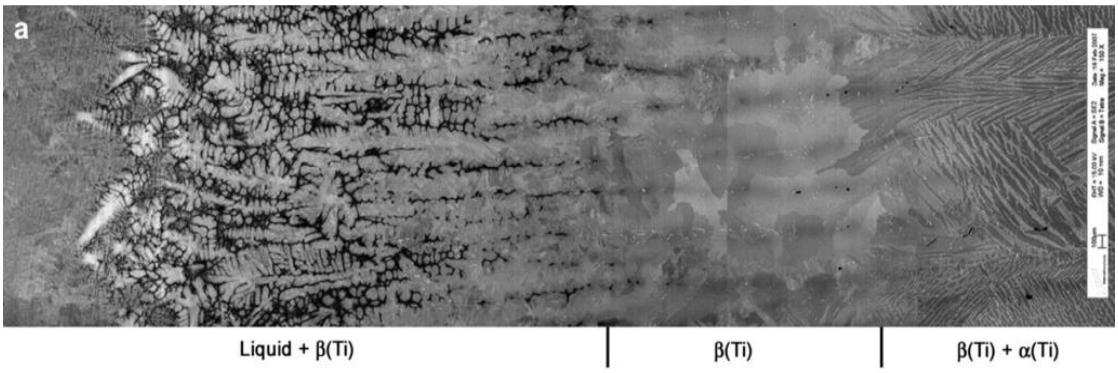

Figure 5-3. Sample Ti-45Al-8,2Nb water quenched [59]

Solidification via β and low boron concentration

Liq. → Liq. + β(Ti) → Liq. + β(Ti) + (Ti, Nb)B → β(Ti) + (Ti, Nb)B → β(Ti) + (Ti, Nb)B → α(Ti) + (Ti, Nb)B

This alloy contains about 0.2 at.% boron and solidifies completely via β(Ti). In this process, small α(Ti) grains grow independently from one another, helped by the blocky borides that act as an inoculant for the α(Ti). However, for low boron contents β-solidifying TiAl alloys, the main reason of grain refinement is that the nucleation of α(Ti) first occurs in the previous interdendritic regions still enriched in aluminium, and finally in the nuclei of the dendrites. Consequently, β(Ti) dendrites grow parallel to the direction of solidification and ribbon borides in interdendritic regions, while blocky borides may be randomly precipitated, mostly in interdendritic regions (Figure 5-4) [59].

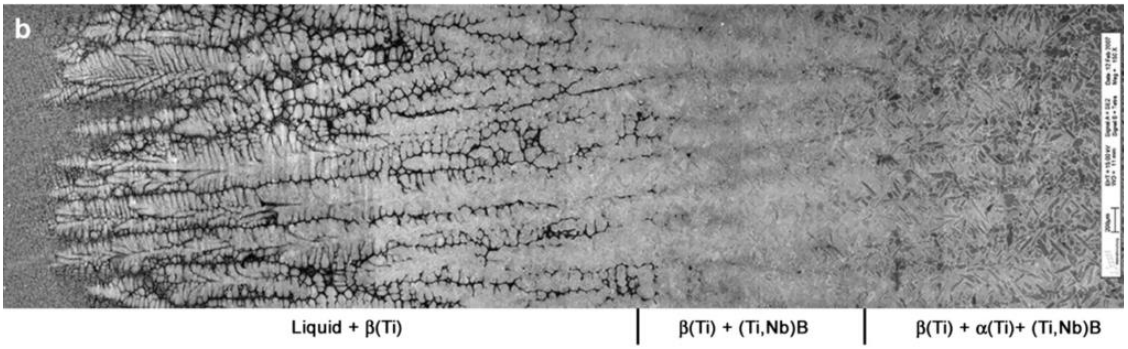

Figure 5-4. Sample Ti-43.2Al-8.3Nb-0.2B-0.2C water quenched [59]

From Figure 5-5, it can be concluded that if the solidification pathway is completely through the β(Ti) (Figure 5-5a and Figure 5-5b), then excellent grain refinement is achieved owing to the presence of borides (Figure 5-5b) during the solid-state transformation β(Ti) → α(Ti). However, in the peritectic reaction α(Ti) can nucleate on β(Ti) dendrites, and thus borides are no longer effective as grain refiners (Figure 5-5c) [58] [59].

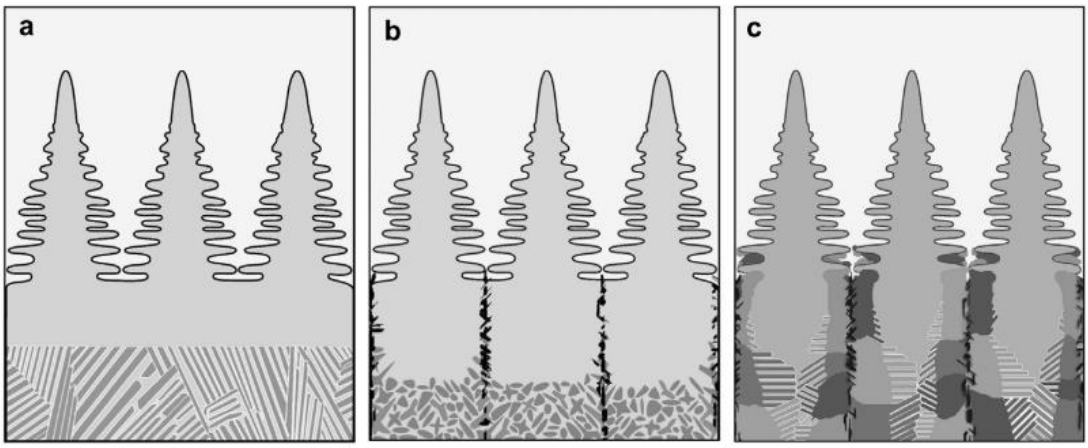

Figure 5-5. α(Ti) formation along representative transformation pathways. The liquid in White, β(Ti) – light grey, borides – black, α(Ti) – dark grey [59]

5.1.3 Conclusions

In summary, the addition of boron to β(Ti)-solidifying TiAl alloys changes the mechanism of α(Ti) formation, giving rise to excellent grain refinement. The reason is that randomly precipitated blocky borides formed in interdendritic regions act as heterogeneous nucleation sites for α(Ti) during the α(Ti) to β(Ti) solid-state transformation. In this way they prevent the majority of α(Ti) grains from becoming orientation variants that obey Burgers Orientation Relationship. In the case of low boron β(Ti)-solidifying TiAl alloys, these α(Ti) grains dominate the structure because their growth starts within the aluminium rich interdendritic areas of the parent β(Ti), resulting in limited grain refinement. However, the peritectic reaction severely impedes the refinement effect. Once peritectic α(Ti) is nucleated, it will grow in the direction of solidification, leading to a pronounced texture with elongated grains. As seen in Chapter 2, boron plays a key role in grain refinement effect during the solid-state transformation from β to α. However, inadequate cooling rates and boron content can have a detrimental effect on mechanical properties, as the borides precipitate in the form of ribbon borides instead of beneficial blocky borides. Thus, new chemical compositions and casting processing parameters should be explored which, by maintaining the solidification via the β-phase, precipitate the beneficial blocky boride and develop a homogeneous and fine-grained microstructure.

5.2 Casting of the modified TNM

This section analyses the casting process of the modified TNM alloy. First the chemical compositions to be melt were determined, and then the casting process parameters were adjusted to develop the target microstructure.

5.2.1 Raw materials procedure

To achieve the desired chemical compositions, billets of the TNM-0.1B master alloy in the as-received state from GfE were alloyed with different elements. The billet of TNM-0.1B has a chemical composition of Ti-44.5Al-4Nb-1Mo-0.1B at.%, with a diameter of 58 mm, and 80 mm height. Titanium powder with a particle size of less than 45 µm, TiB_2 powder with a particle size of less than 10 µm, and rolled pure aluminium were used as alloying elements (Figure 5-6). These alloying elements were mixed and packaged into several spheroidal aluminium containers. During casting, the billet was melted in the crucible, while the alloying elements were added to the melt once the billet was fully melted.

a) **b)** **c)**

Figure 5-6. Preparation of the chemical compositions; a) Ti and TiB_2 powder, plus rolled aluminium, b) Several spheroidal containers and c) Spheroidal aluminium container added to the melt

5.2.2 Mould procedure

The stepped mould geometry described in Section 4.3 was employed for the casting of the modified TNM alloys. Alumina was selected as the most suitable material as it has a good balance between chemical stability and ease of manufacture. More stable refractories such as yttria tend to show poorer physical stability, despite having greater chemical stability than alumina. However, as the molten TiAl is only in contact with the alumina mould for a short time and the reactivity of TiAl is lower than of conventional titanium alloys, alumina was determined to be appropriate. The preheating temperature was set to 600 ºC.

A hole was made in the centre of each step of the mould, for the placement of thermocouples to record the evolution of the temperature. As a result, the T vs t curve was obtained from the moment the metal come into contact with the mould until it completely solidified, as well as its subsequent cooling for the determination of the solidification cooling rate. Figure 5-7 shows the stepped mould and the casting part after the casting.

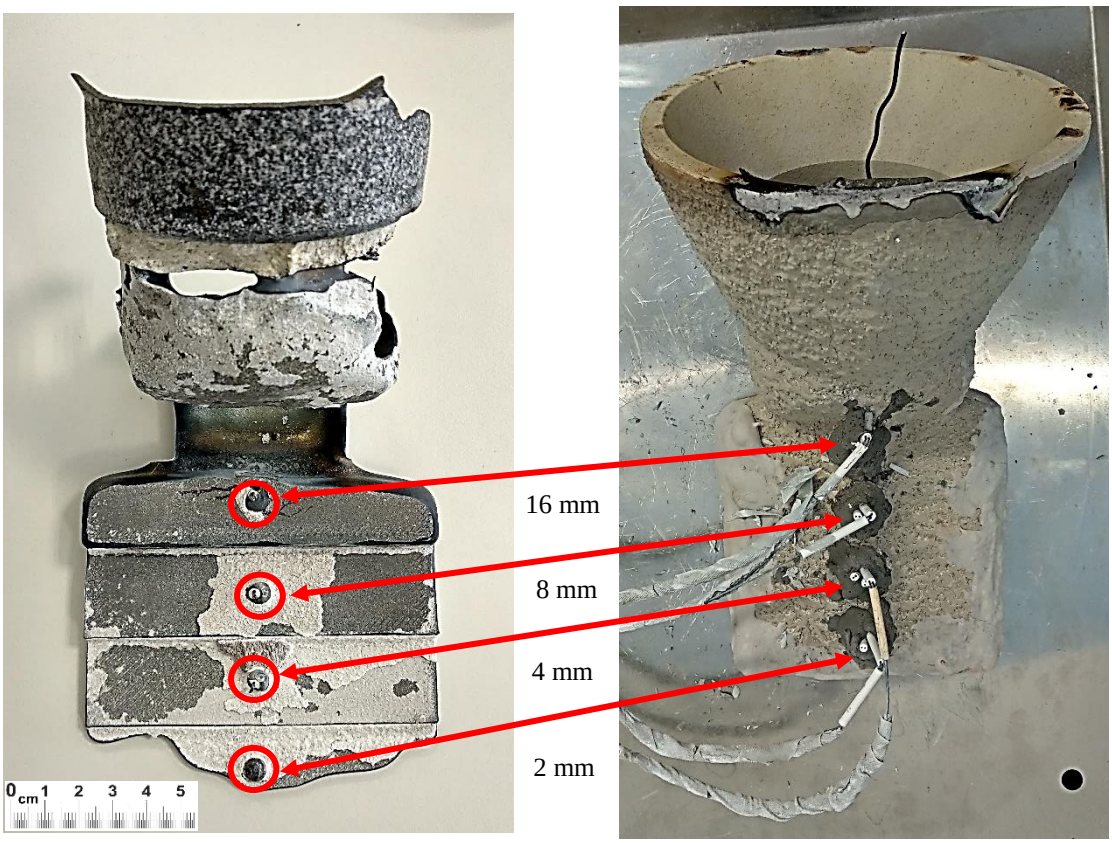

Figure 5-7. Casting components; a) Modified TNM alloy, casting part and b) Alumina stepped mould

5.2.3 Standard melting profile procedure

The master alloy billet was cast by applying a stepped power profile. The criterion of power increase was the moment when the temperature tended to stabilize (the slope approaches became constant). Once the billet was fully melted and subsequently given time to properly homogenize, the alloying elements packed into a container were poured in. To achieve this, the crucible was tilted towards the side of the pole vault and the container was placed just above the crucible. The heat rising from the radiation released the container, causing it to fall into the crucible. After a couple of minutes, the melt was alloyed and homogenized. Then, the power was increased to the maximum and the argon flow was set high to achieve the highest overheating. Finally, the power was shut off and the melt was poured into the mould. From that moment on, the mould was monitored, recording the evolution of the temperature during the solidification and subsequent cooling of the metal.

Figure 5-8 shows the key moments during the melting of the billet, where the solid line represents the temperature measured by the pyrometer and the dashed line represents the corrected temperature of the surface. The value of the surface temperature is mainly conditioned by the heat dissipation due to radiation, and to a lesser extent by the so-called skin effect. During (1) a constant temperature of around 700 ºC was registered since the pyrometer has a working range of measurement between 700 and 1800 ºC. In (2), the moments when the temperature of the charge stop increasing so quickly are indicated. This could be attributed to the greater extraction of heat by the crucible caused by a drop in the temperature of the cooling water coming from the chiller. In (3) it can be seen that after around 42 minutes the charge is fully melted, while the abrupt increase in temperature is related to the melting of the last part of the billet (top slice of the billet). The holding time of the alloyed melt was maintained for only a few minutes since aluminium has a high partial pressure, which promotes its evaporation. At (4) the container with the alloying elements is poured into the melt. Finally, in (5) the melt is poured into the mould.

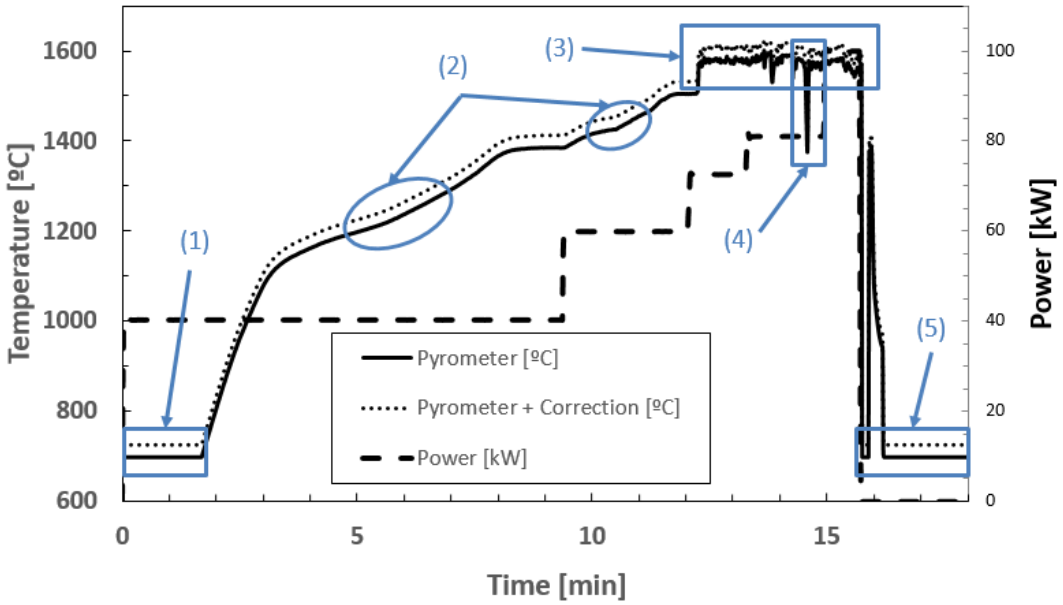

Figure 5-8. Power vs time profile, during the casting

5.3 Microstructure analysis

** The results and conclusions presented in this section have been published in the journal Metals* [60].

The TNM-0.1B master alloy exhibits segregations with ribbon borides inside. Therefore, this microstructure is not suitable because ribbon borides act as a crack initiator and there is heterogeneity in the internal structure of the material which is commonly associated with detrimental mechanical properties. To achieve the required microstructure, the chemical composition of the as-received TNM-0.1B master alloy was therefore modified, and the effect of the cooling rate in the resulting microstructure was analysed. The goal was to obtain the most suitable microstructure for high-temperature applications from the as-cast state, which can be further improved through heat treatments, eliminating the need for hot working processing. In this way more cost-effective components with enhanced properties can be developed.

The as-received TNM master alloy had a fairly high content of aluminium which could lead to detrimental peritectic solidification. In addition, low boron contents seem to promote the precipitation of undesired ribbon borides under fast cooling rates. For this reason both behaviours were analysed, and as a result chemical compositions with lower aluminium and higher boron content were proposed

This section studies the effect of the content of aluminium and boron on the microstructure, with the aim of eliminating segregations and promoting the precipitation of beneficial blocky borides. As a result, two different chemical compositions are proposed and analysed (Table 5-1). The master alloy was also cast to understand the effect of the processing route in the microstructure, relating the effect of the chemical composition and solidification cooling rate under the same conditions.

Table 5-1. Real chemical compositions of the alloys obtained by inductively coupled plasma (ICP)

Concentration (at.%)	Ti	Al	Nb	Mo	B
TNM-0.1B (master alloy)	50.4	44.5	4	1	0.1
TNM-0.6B	50.1	44.6	3.6	0.9	0.6
TNM-1.5B	51.4	42.5	3.5	0.9	1.5

5.3.1 Effect of the chemical composition

It is well known that in β-solidifying TiAl alloys a small variation in the chemical composition induces microstructural changes, in particular with aluminium. However, the cooling rate is relevant given a fixed chemical composition. Thus, both effects must be analysed independently. To this end, the fast cooling 2 mm step and the slow cooling 16 mm were evaluated and compared.

Surface of the 2 mm Step (Fast Cooling)

The TNM-0.1B master alloy was the alloy with the lowest boron content. It exhibited different types and amounts of borides in different locations. While no segregations were observed on the surface, a large number of entangled ribbon borides and segregations

were detected microns below the surface (Figure 5-9a), which are detrimental to the mechanical properties of the alloy. Figure 5-9b shows a detailed image of ribbon borides and segregations, in this areas the lamellar colonies are very large and not well defined.

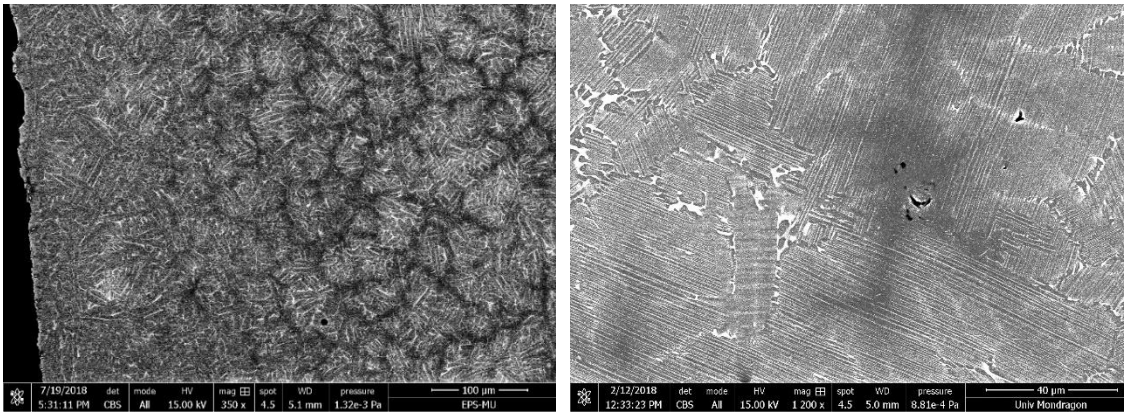

a) **b)**

Figure 5-9. BSE image of the 2 mm step of the TNM-0.1B alloy; a) ribbon borides inside segregations close to the surface and b) detailed image of the ribbon boride

The microstructure is not homogeneous, and as a result, there are many segregations with entangled ribbon borides. The black regions were enriched with aluminium and depleted with β-stabilising elements (niobium, molybdenum). The lamellar microstructure displays a chemical composition similar to that of the bulk alloy. While the γ-phase was slightly enriched with aluminium, the β-phase was enriched with the β-stabilising elements, especially in molybdenum, which is a stronger β-stabilising element than niobium. Indeed, there is a tendency to form microshrinkages around the segregations which seems to be related to these being the last areas to solidify.

In the modified TNM-0.6B, randomly dispersed segregations with ribbon borides inside are clearly observed, but not as many as in TNM-0.1B (Figure 5-10) where some blocky borides were detected. Overall, the TNM-0.6B exhibits a more homogeneous microstructure than the TNM-0.1B, and the entangled ribbon borides do not appear to be as lengthy but more randomly dispersed.

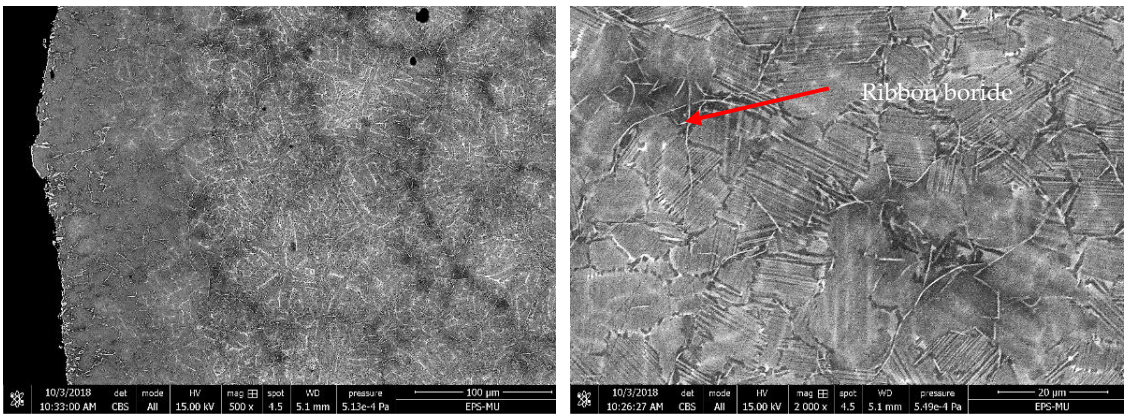

a) **b)**

Figure 5-10. BSE image of the 2 mm step of the modified TNM-0.6B alloy; a) ribbon borides inside segregations close to the surface and b) detailed image of the ribbon borides

The modified TNM-1.5B alloy shows a more homogeneous microstructure than the modified TNM-0.6B alloy, as there are few randomly dispersed segregations with ribbon borides close to the surface (Figure 5-11). A higher amount of β-phase can be observed, likely as a result of a reduction in aluminium within the bulk chemical composition. Some blocky borides can also be seen.

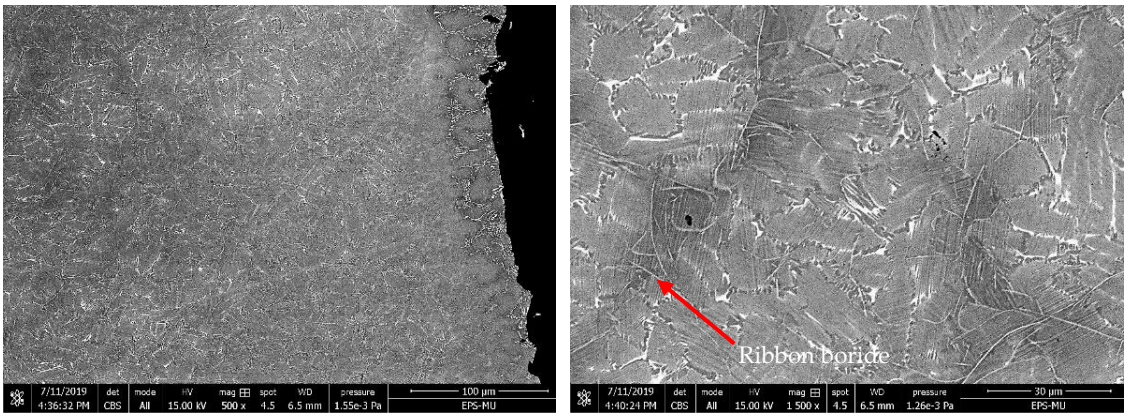

a) **b)**

Figure 5-11. BSE image of the 2 mm step of the modified TNM-1.5B alloy; a) ribbon borides inside segregations close to the surface and b) detailed image of the ribbon borides

Interior of the 16 mm Step (Slow Cooling)

The TNM-0.1B alloy exhibits microshrinkages in the casting arising from hot spots created during solidification. This is because there is a tendency to form a greater number towards the interior of the specimen due to a slower solidification cooling rate, and thus it remains the last areas to solidify. An analysis revealed mostly randomly dispersed ribbon borides, and minor segregations were detected. Nevertheless, a quite homogeneous microstructure with few blocky borides is achieved (Figure 5-12).

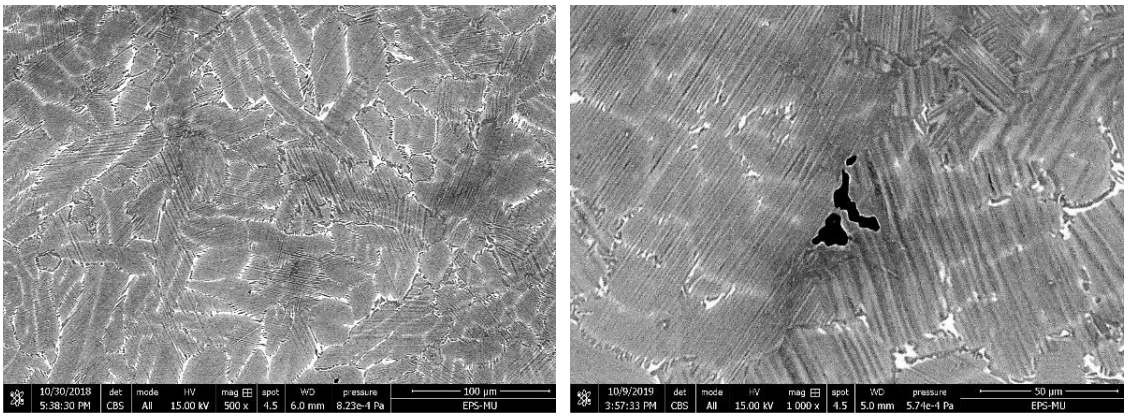

a) **b)**

Figure 5-12. BSE image of the 16 mm step for the TNM-0.1B alloy; a) general image and b) detailed image

In the case of the modified TNM-0.6B alloy, no segregations can be observed. The number of ribbon borides decreased, while the number of blocky borides increased. The bulk alloy exhibits a fine and homogeneous microstructure with a mixture of ribbon and

blocky borides (Figure 5-13). As a result, the lamellar colony size is finer and the plates of α_2/β better defined.

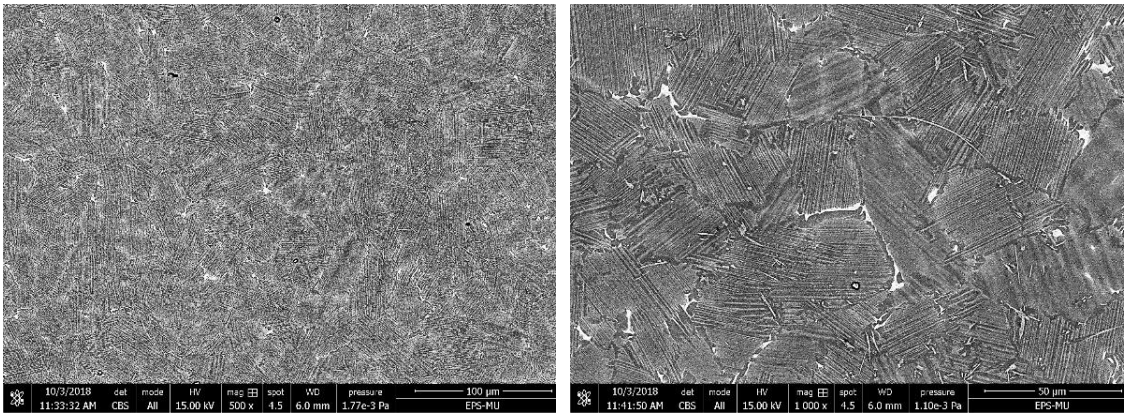

a) **b)**

Figure 5-13. BSE image of the 16 mm step for the modified TNM-0.6B alloy; a) general image and b) detailed image

The modified TNM-1.5B (Figure 5-14) alloy presents a similar microstructure to the modified TNM-0.6B alloy, with no segregations. However, most of the borides are of the blocky type, and the ribbon borides are not typically entangled. The distribution of blocky borides is more homogeneous than in the modified TNM-0.6B alloy. Overall, the TNM-1.5B displays homogeneous lamellar colony with a large number of well-distributed blocky borides, and a higher amount of β-phase due to the lower amount of aluminium.

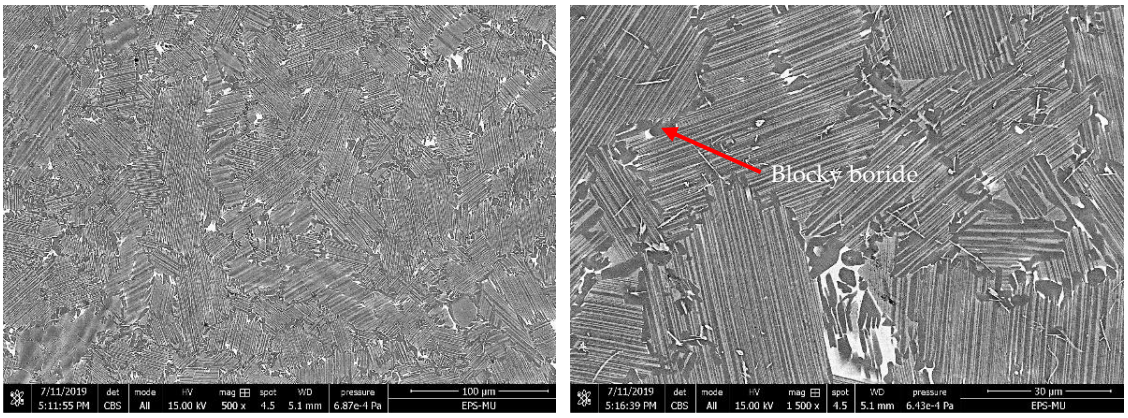

a) **b)**

Figure 5-14. BSE image of the 16 mm step of the modified TNM-1.5B alloy; a) general image and b) detailed image

Conclusions

Table 5-2 summarizes the key points of the effect of the chemical composition on the microstructure. On the one hand, TNM alloys with boron contents below 0.5 at.% seem to promote the formation of segregations with detrimental ribbon borides, in areas subjected to high cooling rates during solidification. On the other hand, boron contents above 0.5 at.% help to precipitate beneficial blocky borides, in areas with low solidification cooling rates. Heterogeneity in the microstructure is related to the presence of ribbon borides and segregations which are detrimental.

Table 5-2. Summary of the effect of chemical composition on the microstructure and type of boride to be precipitated.

Alloy		**TNM-0.1B**	**TNM-0.6B**	**TNM-1.5B**
Location	**Surface of 2 mm step (fast cooling)**	Many entangled ribbon borides and segregations	Randomly dispersed ribbon borides and segregations, with some blocky borides	Randomly dispersed ribbon borides and segregations, with some blocky borides
	Inside 16 mm step (slow cooling)	Minor segregations with ribbons and few blocky borides	No segregations and mixture of ribbons and blocky borides	No segregations with many blocky and few ribbon borides

Of the three different chemical compositions, the TNM-1.5B alloy presented the best microstructure in terms of homogeneity and fine grain, with plenty of blocky borides and no segregations. This alloy was thus chosen for subsequent analysis of the effect of the cooling rate.

5.3.2 Effect of the solidification cooling rate

In this section, the solidification of the TNM-1.5B alloy is analysed using the sensorized mould, to assess the effect of the solidification cooling rate on the as-cast microstructure. One consideration to take into account is that the ISM technology has low overheating, and the fluidity of titanium alloys is quite limited. Thus, premature solidification is expected. To overcome this limitation and to obtain a more accurate solidification cooling rate, the average cooling rate during the first 5 seconds after pouring was measured in the experimental trials (Table 5-3). The results reveal that the 2 mm step cooled at a rate of 44 K/s, and the 4 and 8 mm steps cooled at 25 K/s and 7 K/s, respectively. Technical problems related to shrinkage between the metal and the thermocouple during the experiment prevented data acquisition for the 16 mm step, so no cooling rate was recorded. However, the computational simulation predicts a cooling rate of around 2 K/s in this sample region.

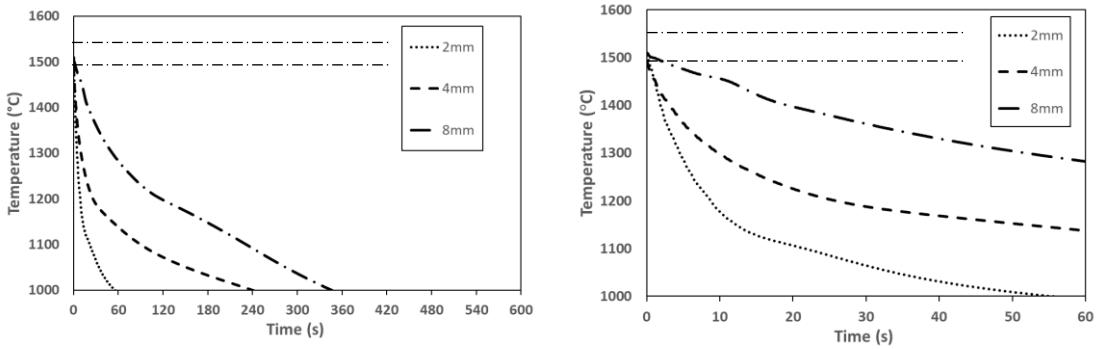

Figure 5-15. Experimental cooling curves of the modified TNM-1.5B alloy cast in a stepped mould with 2-4-8 mm thickness; a) general and b) detailed

Where the solidification range is indicated by long lines with dots

Table 5-3. Experimental cooling rate during the first 5 seconds after pouring

	2 mm	**4 mm**	**8 mm**	**16 mm**
Experimental cooling rate [K/s]	44	25	7	*2

**—Value obtained from the computational simulation*

Microstructure analysis

The next step is to relate the solidification cooling rate with the microstructure, for the selected TNM-1.5B. The microstructural analysis was performed close to the cooling rate areas analysed, to provide a better relationship between the cooling rate and the microstructure. Analysis and comparison of the SEM micrographs (Figure 5-16) and the experimentally obtained cooling curves (Figure 5-15) revealed the following: The 2 mm step displays many segregations with entangled ribbon borides at a cooling rate of around 50 K/s, while the 4 mm step exhibits fewer segregations, however there are still a great number of ribbons inside segregations at a cooling rate of around 25 K/s. In the case of the 8 mm and 16 mm steps with cooling rates below 10 K/s, the microstructure does not show segregations, but rather a fairly homogeneous distribution of constituents. This is particularly noticeable in the case of the 16 mm step with the precipitation of mostly blocky borides.

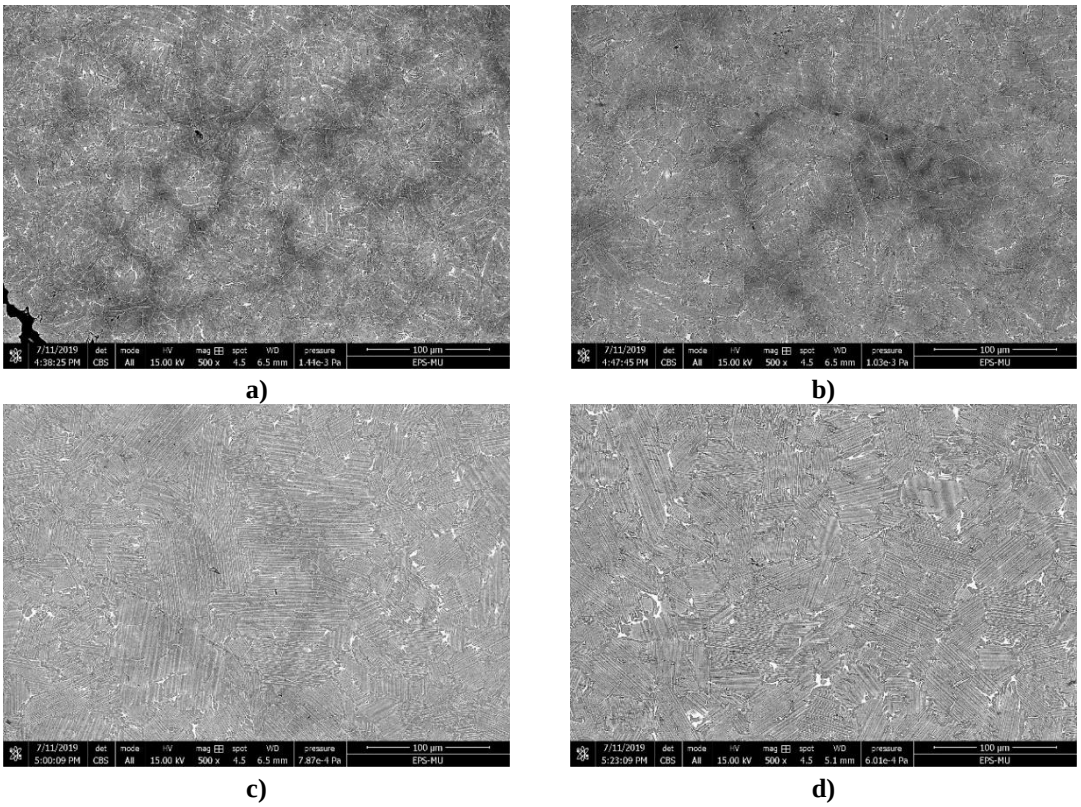

Figure 5-16. BSE image showing the general microstructure of modified TNM-1.5B alloy; a) 2 mm step, b) 4 mm step, c) 8mm step and d) 16 mm step

Conclusions

Analysis of the effect of the solidification cooling rate revealed that cooling rates above 10 K/s exhibit segregations with ribbon borides inside. Thus, it can be concluded that these are not ideal microstructures. Cooling rates below 10 K/s led to a homogeneous and fine microstructure, and can be considered beneficial for the mechanical behaviour of the alloy. This phenomenon seems to be related to equilibrium and disequilibrium conditions, in which the cooling rate and chemical composition are interrelated parameters. To gain better understanding of this phenomenon, a boride formation mechanism is proposed to determine the type of boride which forms depending on the solidification conditions.

5.3.3 Boride formation mechanism

In this section, the formation mechanism of the two types of borides in TNM alloys is presented. A formation mechanism of ribbon borides is first proposed, which is associated with faster cooling rates than 10 K/s. In the case of slower cooling rates than 10 K/s, a blocky boride formation mechanism is proposed.

Ribbon Boride Formation Mechanism

If the boron concentration is lower than the critical value (around 0.5 at.%), then borides will not form until the liquid reaches the solubility limit for boron. As a result, progressive enrichment of the liquid occurs in boron, while the β-phase is nucleated from molybdenum and niobium, leading to a melt that becomes more enriched in aluminium and boron. The proposed ribbon boride formation mechanism follows the principle outlined by Porter *et al.*, entitled "near none diffusion in solid, slow diffusional mixing in liquid" [61].

During solidification, the surface of the alloy is the first region to solidify, and as a result, boron and aluminium are moved towards the interior of the melt until the solubility limit of boron in the melt is reached. Once the boron is no longer soluble in the liquid due to its local high concentration and low solubility in aluminium [27], precipitation of ribbon borides in the form of chains/flakes takes place. Aluminium is enriched in these areas because of the depletion of β-stabilising elements.

Figure 5-17 shows the concentration profile based on the depth starting from the surface (of the mould) and the formation of ribbon borides. In Figure 5-17a, a SEM micrograph shows the surface of the TNM-0.1B alloy where a large number of entangled ribbon borides are precipitated some microns from the surface inside segregations, this is related to the fast cooling rate of the surface. Figure 5-17b plots the elemental concentration profile from the surface. It can be seen that the peak of boron is located at a certain depth from the surface due to its rejection during the solidification. Finally, Figure 5-17c depicts the formation mechanism of the ribbon borides by taking into account the migration of elements across the depth.

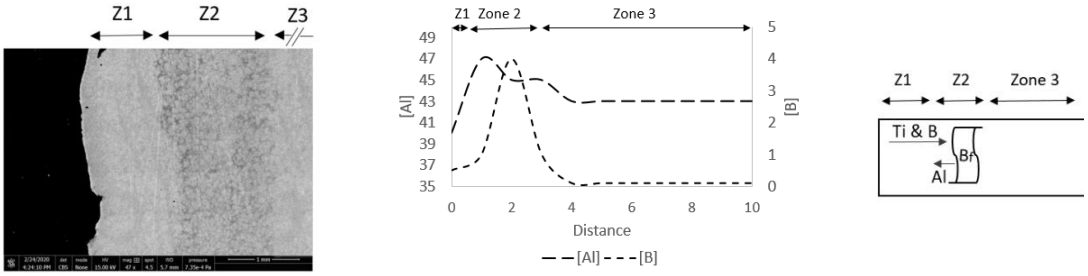

a) **b)** **c)**

Figure 5-17. Ribbon boride formation mechanism; a) SEM micrograph, b) elemental concentration profile from the surface and c) 2D depiction of the formation mechanism of the ribbon boride

Zone 1: Movement of boron and aluminium towards the interior
Zone 2: Precipitation of ribbon borides once the solubility limit of boron and aluminium is reached
Zone 3: Progressive restoration of the nominal chemical composition

An overly high solidification cooling rate leads to the formation of ribbon borides, even if the boron concentration is high enough. This is due to the localised depletion of boron under non-equilibrium solidification conditions.

Blocky Boride Formation Mechanism

Blocky borides tend to appear when the boron content is higher than the critical value (around 0.5 at.%), through random precipitation before the end of solidification, especially when the cooling rate is lower than 10 K/s. This leads to a grain refinement effect during the solid-state transformation from the β-phase to the α-phase, and hence, better mechanical properties can be achieved [22].

Blocky borides are formed from a mixture of titanium, boron and a small amount of niobium, but they reject aluminium (Figure 5-18). As niobium has a high melting point, it may act as a nucleant for these borides. In Figure 5-18a SEM micrograph of blocky borides are shown where the microstructure is quite homogeneous with a well defined lamellar microstructure, and no segregations. Figure 5-18b proposes the elemental concentration profile from the surface of the sample, and there is no macroscopic variation in the elemental distribution due to homogeneity. As a result, there are no segregations, but instead many blocky borides enriched in niobium and randomly dispersed, as depicted in Figure 5-18c.

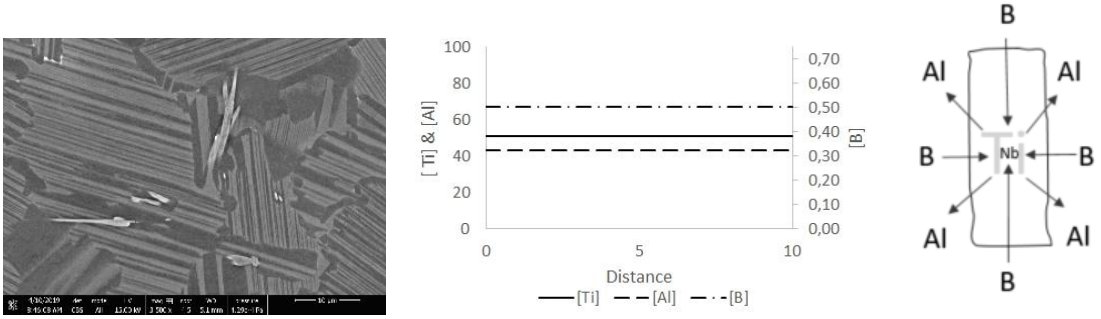

a) **b)** **c)**

Figure 5-18. Stick-shaped blocky boride formation mechanism; a) SEM micrograph, b) elemental concentration profile from the surface and c) 2D depiction of the formation mechanism of the blocky boride

As a result of homogeneity in the specimen, there was no microscopic chemical composition gradient

It is important to highlight that even if the amount of boron is high enough to precipitate blocky borides, the cooling rate should not be too high to prevent local disequilibrium, which could lead to the precipitation of ribbon borides. In the present study, a solidification cooling rate below 10 K/s is recommended.

5.4 Conclusions

Boron helps refine the microstructure of β-solidifying TiAl alloys during the solid-state transformation from β to α-phase. Boron acts as heterogeneous nucleation sites for the α-phase whenever blocky borides are precipitated, and a homogeneous microstructure is developed. However, the β-solidifying pathway has a narrow chemical composition range, and minor variations in the chemical composition can lead to an undesired peritectic reaction. The peritectic reaction severely impedes the refinement effect, producing texture with elongated grains, and thus steps must be taken to prevent it.

With the aim of designing microstructure suitable for casting that provides a homogeneous microstructure with the precipitation of the benefitial blocky boride, the effect of the chemical composition in conjunction with the cooling rate was analysed. To achieve this goal, the TNM-0.1B master alloy was alloyed with boron, aluminium and titanium; while the solidification cooling rate of the thin and thick steps of the mould were examined. From this process the following conclusions can be drawn:

Ribbon borides are formed under non-equilibrium conditions. They are precipitated when the cooling rate is too high, even if the amount of boron is high enough to precipitate blocky borides. Ribbons are formed mainly inside segregations due to their rejection of aluminium. As a result, large lamellar colonies are formed with entangled ribbon borides, which are detrimental to mechanical properties.

For the modified TNM alloy under study, when the boron content is above around 0.5 at.% and the cooling rate during solidification is below 10 K/s, blocky borides are precipitated under equilibrium conditions. In contrast, boron contents above the critical value and intermediate cooling rates are associated with the precipitation of a mixture of ribbon and blocky borides.

It is important to note that the cooling rate during solidification seems to be more relevant than chemical composition, to the precipitation of either ribbon or blocky borides. Therefore, to obtain a refined microstructure with no segregation, a cooling rate below 10 K/s and a boron content above the critical value must be ensured.

Chapter 6

6 Heat Treatments and Creep

In this chapter, the appropriate HT is designed so as to meet the required mechanical properties for aerospace and aeronautics components. Given that these components usually work for long periods at high temperatures and under relatively continuous load, the creep behaviour is a suitable performance test. To this end, the effect of different microstructures in terms of type, quantity and morphology of the different micro-constituents on mechanical properties is analysed. The resulting HT is designed to develop suitable creep strength for a cast processing route of novel modified TNM alloys.

Next, a novel process for TiAl alloys that integrates the HIP and HT processes into a single stage, a so-called "Integrated Hot Isostatically Pressing and Heat Treatment (IHH)" is presented. This reduces the processing time required for manufacturing final TNM components, achieving greater cost-effectiveness.

Finally, the mechanical behaviour of the samples is evaluated through creep tests. The novel modified TNM alloy and its post-thermomechanical processing is compared against the conventional forged TNM alloy, and the chapter concludes with a summary of the key achievements.

6.1 State of the Art of Heat Treatments on TiAl Alloys

Currently when processing TiAl alloys, as-cast plus Hot-Isostatically Pressing (cast/HIP) is the starting state for thermomechanical processing of the material, to adjust the microstructure through forging and the ensuing HT. Forging of γ-TiAl is conducted in a temperature range from 0.7 to 0.9 T_m [1]. Then, the material is heat-treated via multi-step HT to ensure balanced mechanical properties, at both room and high temperatures. A balance between strength and ductility of the final microstructure is achieved by forming small and narrow interlamellar spacing α_2/γ colonies with some globular γ-grains at the colony boundaries [23] [8].

HIP is a necessary step to reduce the number of micropores. In the case of the TNM alloy, HIP is typically performed by heating the material to 1200 ºC, hold for 4 h at 200 MPa, and subsequent furnace cooling (< 8 K/min) to room temperature. During this process a decomposition reaction within the α_2/γ-colonies according to $\alpha_2 \rightarrow \beta + \gamma$ takes place, which leads to an increase in the thickness of the γ-lamellae, as well as to the formation of secondary precipitates of the β_0-phase (called $\beta_{0,sec}$) within the α_2/γ-colonies. ω-domains can also be found within the β_0-phase, and thus further processing is required to achieve the required mechanical properties after reducing the internal porosity with HIPing [36] [62].

In the last decade, adjustment of the desired microstructure is typically conducted by hot-forming operations and further HT starting from the cast/HIP state. However, grain refinement can also be achieved by a combination of forging and post-forging

recrystallization HT, where phase transformation in interaction with recrystallization takes place, but at the expense of forging texture and segregation [3]. For this reason, it is not an appropriate processing route.

More recently, new studies have applied several multi-step HT to a cast/HIP TNM alloy without any hot-working process, with the aim of achieving mechanical properties similar to forged plus heat-treated material [63] [36] [64]. However, knowledge in how to achieve creep resistant TNM components straight from the cast/HIP state is still lacking, and no studies have integrated HIP/HT into a single process called "Integrated HIP/HT processing (IHH)".

6.1.1 Conventional heat treatment in TNM alloys

The combination of thermo-mechanical processing such as HIP, forging and multiple heat-treatments has led to an adjustment of different types of microstructures. This is in addition to refining the mechanical properties by controlling morphological parameters such as grain size, colony size, and aspect ratio or lamellar interface spacing. From the aeronautics point of view, the fully lamellar or nearly fully lamellar microstructure presents the best combination of strength, creep resistance, ductility and fracture toughness [3].

To achieve a nano-lamellar structure, a two-step heat-treatment in a TNM alloy is usually carried out after forging (Figure 6-1). During the first heat-treatment step, a solution heat-treatment is conducted above the γ-solvus temperature, leaving only disordered α and β-phase. Upon subsequent rapid cooling, the formation of lamellar γ-phase can be suppressed, which can then be finely and homogeneously precipitated in the ensuing annealing. During the second heat-treatment, the annealing procedure is typically conducted slightly above the envisaged service temperature. During this stage γ-lamellae forms in the supersaturated α_2 grains. This is achieved with sufficient thermal activation, owing to the creation of partial dislocations and bordering a stacking fault that locally accomplishes the change in the crystal structure. Finally, the alloy is slowly cooled to room temperature to minimize internal stress [3] [13] [36].

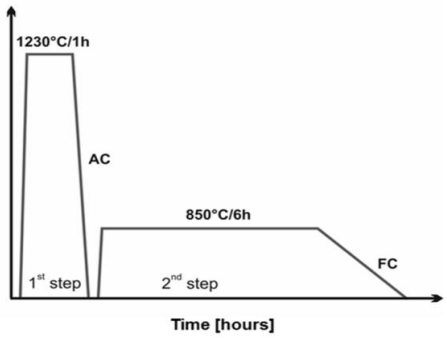

Figure 6-1. Selected HT after Cast/HIP plus forging for TNM alloy

Thus, the first step of the heat-treatment minimizes the β-phase fraction and adjusts the size of the α-grains, which are precursors to the lamellar γ/α_2-colonies. Nevertheless air-cooling (around 700 K/min) after the first step has a detrimental effect, and the resulting microstructure is far from thermodynamic equilibrium, with only a small amount of γ-phase present at the beginning of the second HT step. Therefore, a second heat-treatment

step is conducted below the eutectoid temperature, which brings the microstructural constituents closer to thermodynamic equilibrium. This is achieved by the formation of fine γ-lamellae in the supersaturated α_2-grains, the precipitation reaction starts at a temperature about 700 ºC, resulting in the formation of a mean interface spacing including α_2/γ and γ/γ of around 20 µm (Figure 6-2) [36] [13].

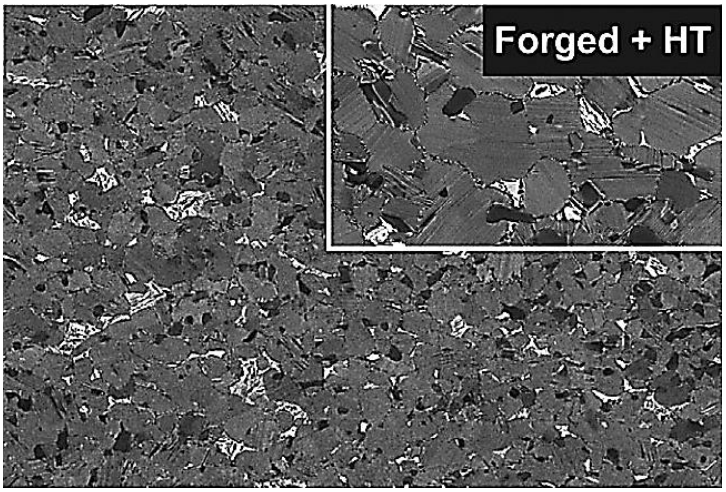

Figure 6-2. TNM microstructure in the cast/HIP plus forged plus heat-treated state [36]

It has been stated that the stress required to propagate dislocations through the interfaces is inversely proportional to the square root of the mean interface spacing. Thus, the finer the interlamellar spacing the harder the dislocation motion and α_2/γ and γ/γ-interfaces act as glide obstacles, leading to dislocation pile-ups. The increase in yield strength after the second heat-treatment step is primarily caused by the formation of fine γ-lamellae within α_2-grains. Indeed, increasing the temperature of the second heat-treatment step results in an increase in tensile ductility at room temperature, as well as a lowering in the yield strength (Figure 6-3) [65].

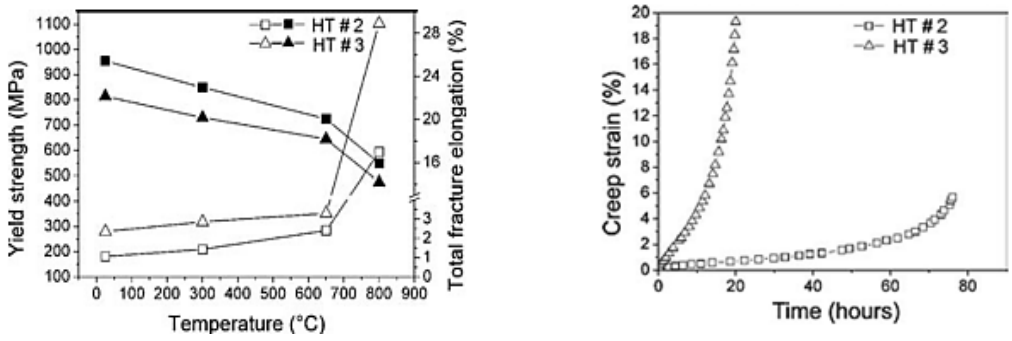

a) **b)**

Figure 6-3. TNM after HT#2 (850 ºC, 6h/FC), HT#3 (950ºC/6h/FC); a) 0.2% Yield strength, fracture elongation and b) Creep tests conducted in air at 800 ºC and 300 MPa [65]

During the second heat-treatment or so-called stabilization treatment, a cellular reaction can be observed at the α_2/γ colony boundaries, which leads to a partial breakdown of the lamellar colonies into a local refinement of the microstructure. The driving force of this cellular reaction is a strong disequilibrium after the first HT, which results in the formation of a very fine lamellar structure during the second heat-treatment step. During

the cellular reaction, there is an increase in the total grain interface energy of the lamellar interface. This can be compensated by the formation of a coarser lamellar structure, which reduces the interface area per unit volume of the material. Additionally, ω-phase are present in the β(B2)-grains with an average size in the range of 150 to 300 nm. This phase (covered in Chapter 2) with a HCP crystal structure is quite brittle and has a similar composition to β-phase, but with a higher molybdenum content [65].

6.1.2 Heat treatments after Cast/HIP in TNM alloys

In recent years, a number of new multi-step HTs for cast/HIP TNM alloys have been developed, with the aim of eliminating the need for performing hot-working processes [36] [64].

A HT with simple short-term annealing within the single β-phase field region, combined with a subsequent stabilization treatment near service temperatures, demonstrates the major advantages of a HT starting from the cast/HIP state (Figure 6-4). Using such processes, reduced annealing time, better chemical and microstructural homogeneity, and no significant texture is achieved. This multi-step HT has higher tensile yield strength and creep resistance in comparison to forged plus heat-treated material. It also provides a nearly lamellar γ-microstructure, but with a reduction in the ductility at room temperature. Annealing within the single β-phase field region with subsequent air cooling, it achieves an almost complete transformation from β to α, which can be used for a refinement of coarse-grained α_2/γ-colonies. The fast diffusion processes of the HT within the single β-phase region leads to chemical homogenization, in which segregations from the casting process can be minimized [3] [13].

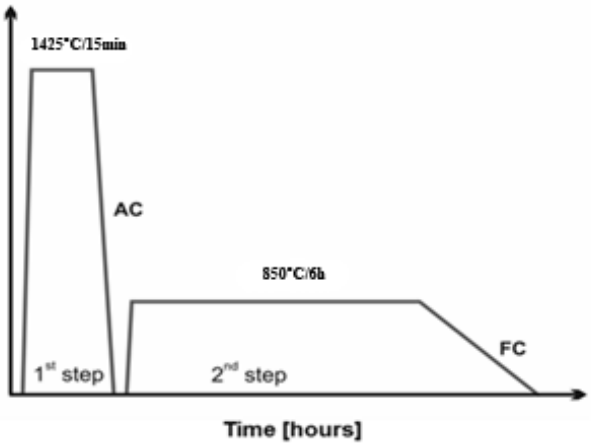

Figure 6-4. Selected multi-step HT after cast/HIP for TNM alloy

The final microstructure after the stabilization treatment consists of 97 vol.% of α_2/γ-colonies and 2 vol.% of β_0-phase at the colony boundaries. The residual content of 1 vol.% belongs to secondary precipitates of the β_0-phase, within the α_2/γ-colonies. Importantly, no cellular reaction is observed. Thus, the α_2/γ-colonies are refined to a length of 100 µm and a width of 15 µm (Figure 6-5) [36]. This microstructure shows great potential to replace the conventional route for TNM alloys. There are still opportunities for improvement however, particularly for modified TNM alloys. In addition, new processing routes that integrate HIP and HT are not currently employed for TNM alloys, which may mark a major breakthrough for the cast/HIP processing route.

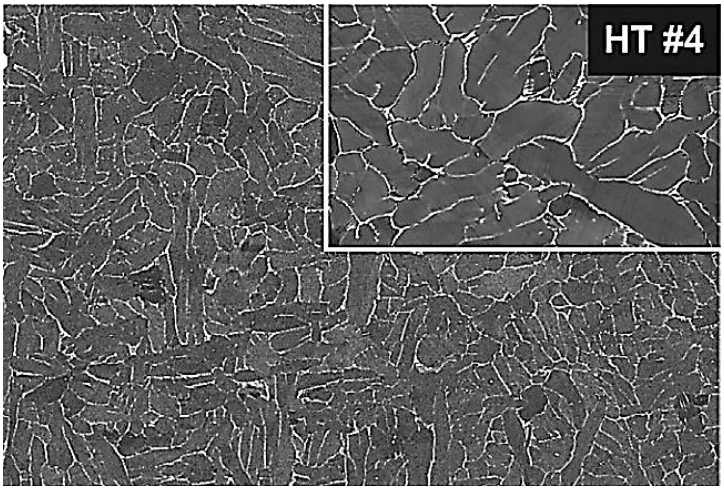

Figure 6-5. TNM microstructure in the cast/HIP plus heat-treated state [36]

6.2 Development of a single-step heat treatment for a modified TNM alloy

** The results and conclusions presented in this section have been published in the journal Intermetallics* [66].

The processing route of the modified TNM alloy under study (Ti-43.4Al-4Nb-1Mo-0.5B [in at %]) follows the Casting/HIPing, avoiding forging and multiple HT.

The desired microstructure should consist of two-phase ($\gamma + \alpha_2$) nearly fully-lamellar microstructures, because of their higher fracture toughness and creep strength in comparison to the duplex microstructure [37] [38] [36]. This difference has been attributed to the α_2-laths that act as reinforcements, and to the morphology of the serrated grains [39]. Therefore, nearly fully-lamellar microstructures exhibit higher fracture toughness and creep strength, as well as stable crack growth behaviour. However, their ductility at room temperature is lower than that of a duplex microstructure [32]. The role of the constituents (Figure 6-6) is critical because when the number of sliding systems is greater, the phase is softer. As a result, the β-phase is softer than the γ-phase, and the γ-phase is softer than the α-phase [40] [41].

Thus, a microstructure with lamellar colonies in the range of 50 to 100 µm, nanometre-spaced lamellae, and a low volume fraction of globular γ-grains and no globular β_0-grains, has the ideal distribution in which to form a fine-grained lamellar colony size with few soft constituents at the colony boundaries. This microstructure exhibits good creep strength, high fracture toughness and adequate ductility [67] [38].

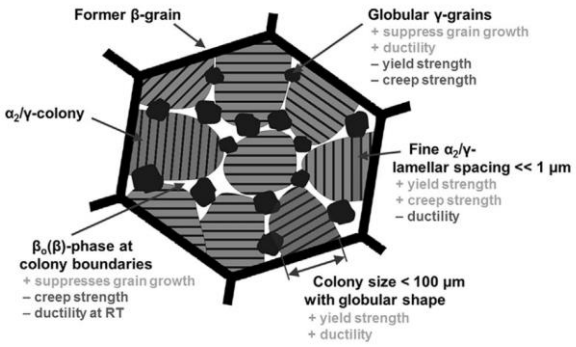

Figure 6-6. Influence of microstructural constituents on the mechanical properties [3]

To achieve the required microstructure, a post-HT is commonly applied to cast/HIPed TNM alloys. For a TNM alloy with a chemical composition of Ti-43.9Al-4.0Nb-0.95Mo-0.1B, from 1250 ºC to 1300 ºC is the most suitable temperature range to minimize β_0 [23]. Recent studies confirm this temperature range (Figure 6-7) [3]. According to [64] for a similar TNM alloy, the lamellae start to vanish at 1245 ºC, and dissolve almost completely at 1265 ºC. Thus, the temperature window should consider this temperature range to minimize the amount of β_0, and then precipitate a fine α_2/γ-lamellae microstructure with small globular γ-grains. This will achieve a refined microstructure of the modified TNM alloy that is suitable for structural applications such as LPT blades, in which creep resistance is mandatory.

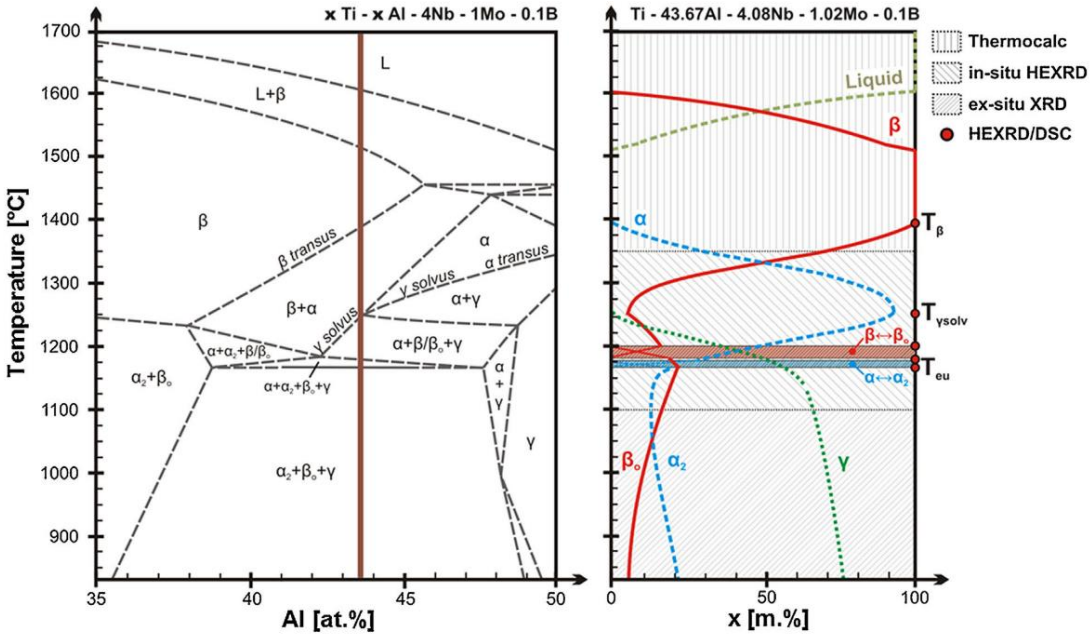

Figure 6-7. Experimental quasi-binary section of the TNM alloy system [3]

6.2.1 Procedure for microstructural development

DSC was employed to develop an appropriate microstructure through the precise control of temperature vs time. Then, the resulting microstructure was analysed using SEM which identifies the most suitable HT. Finally, the IHH process which integrates the HIP and HT processes is presented.

Heat treatment design

DSC was used to both perform the HT and control the cooling rate. DSC is a thermal analysis tool that is used to determine the temperature of phase transition and dissolution kinetics [68]. A NETZSCH STA 449 F3 Jupiter® DSC was used in this work. An argon atmosphere and yttrium crucibles were employed to prevent the TNM alloy from undergoing oxidation and mould-metal reaction. NETZSCH Proteus® software was used for the thermal analysis.

Several thermal profiles were applied to the sample from 1250 ºC to 1300 ºC at a heating rate of 10 K/min. Table 6-1**¡Error! La autoreferencia al marcador no es válida.** shows the thermal profiles applied, which is the temperature range in which the lamellar microstructure dissolves. Once the objective temperature was reached, one hour of isothermal step followed, and then a controlled cooling to room temperature. According to Schwaighofer *et al.*, air or furnace cooling rate are the typical cooling rates for TNM alloys [36], hence cooling rates in the range of 100-50 K/min, 30 K/min, and 10 K/min were used.

Table 6-1. DSC thermal profile applied

Sample	Heating [K/min]	1 h Isothermal [ºC]	Cooling [K/min]
HT 1250	10	1250	100-50
HT 1260	10	1260	100-50
HT 1270	10	1270	100-50
HT 1280	10	1280	100-50
HT 1290	10	1290	100-50
HT 1260 2	10	1260	30
HT 1260 3	10	1260	10

Microstructure analysis

First, it must be considered that the β-phase does not have a specific dissolution temperature, but rather a range of minimisation due to the high content of β-stabilizing elements. Therefore, DSC is a suitable technology to determine the dissolution and precipitation of the lamellar microstructure. While image analysis applied to the SEM pictures is appropriate to measure the amount of β_0-phase remaining at room temperature.

SEM and EDS were performed with a FEI Nova Nano SEM® 450, using BSE to analyse the microstructure and determine the semiquantitative local chemical composition. Leica Application Suite (LAS) software was used to quantify the amount of undissolved β_0-phase of the SEM BSE images in each of the six samples, by taking the mean value of the internal (Zone 1) and external (Zone 2) parts of the sample. The size of the lamellar colony and α_2/γ-lamellar spacing was measured from several SEM BSE images following a procedure similar to the intercept method of ASTM E112, as shown in Figure 6-8. To measure the size of the lamellar colony, five SEM images taken at random with a magnification of x500 were analysed. The value of each lamella is the measurement of the longest diagonal. To determine the lamellar spacing, three SEM images taken at random with a magnification of x3500 were analysed. The value of the lamellar spacing is the thickness of the measured plates divided by the number of $\alpha_2 + \gamma$ plates contained in the lamella.

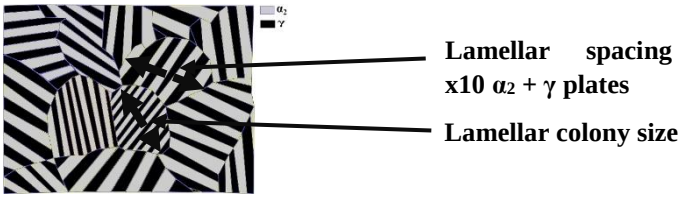

Figure 6-8. Procedure in measurements: lamellar colony size and lamellar spacing

Integrated Hot Isostatically Pressing and Heat Treatment (IHH)

The aim of this process is to achieve greater process efficiency with lower costs, by integrating the HIP and HT processes into a single stage. Known as "Integrated Hot Isostatically Pressing and Heat Treatment" (IHH), this is a new process that has shown great potential in other metallic alloys [69]. The potential benefits to applying this process to TiAl alloys are considerable.

A Quintus-QIH9® HIP lab unit from the Ruhr Universität Bochum was used for the IHH stage. This model is equipped with a new Uniform Rapid Quenching furnace (URQ®) which allows fast and precise cooling from high to low temperatures, as opposed to conventional HIP units which have slow cooling. The QIH9 fast cooling is achieved through heat exchange between the hot gas of the internal chamber and the cold gas outside of the heatshield that is pressed into the hot zone. The hot gas is cooled when passing the heatshield, which acts as a heatsink. At the same time there is a continuous circulation of gas inside the pressure vessel. This gradient of temperature between the inside and outside gas of the heatshield ensures the fast cooling of the sample.

a) **b)**

Figure 6-9. HIP; a) Quintus-QIH9 model and b) URQ® technology

6.2.2 Developing a creep resistant microstructure for a modified TNM alloy

To design a single-step HT for a modified TNM alloy, the target temperature of the treatment has to first be established, and then the cooling rate. In the first block, this target temperature is defined to minimize the amount of β_0-phase, while the optimum cooling rate is established to achieve the desired microstructure in the second block.

Phase dissolution and target temperature for the heat treatment

The results obtained from each HT profile were analysed and compared in terms of phase transformation and dissolution kinetics. This establishes the different dissolution temperatures and the optimal HT temperature.

The first transformation corresponds to the α_2 to α disordering reaction at around 1175 ºC. At a slightly higher temperature of around 1220 ºC, the β_0 to β disordering reaction takes place. Dissolution of the γ-phase above 1250 ºC involves the loss of the lamellar microstructure, and thus newborn lamellar plates form upon cooling.

Figure 6-10 plots the disordering temperature transformations. The low-temperature peak at 1176 ºC corresponds to the α_2 to α disordering reaction, while the high-temperature peak at 1218 ºC denotes the β_0 to β disordering reaction. The area behind each peak represents the energy absorbed by each phase during dissolution, which corresponds to a fully completed reaction. Both disordering reactions exhibited similar transition energies despite the difference in their temperature profiles.

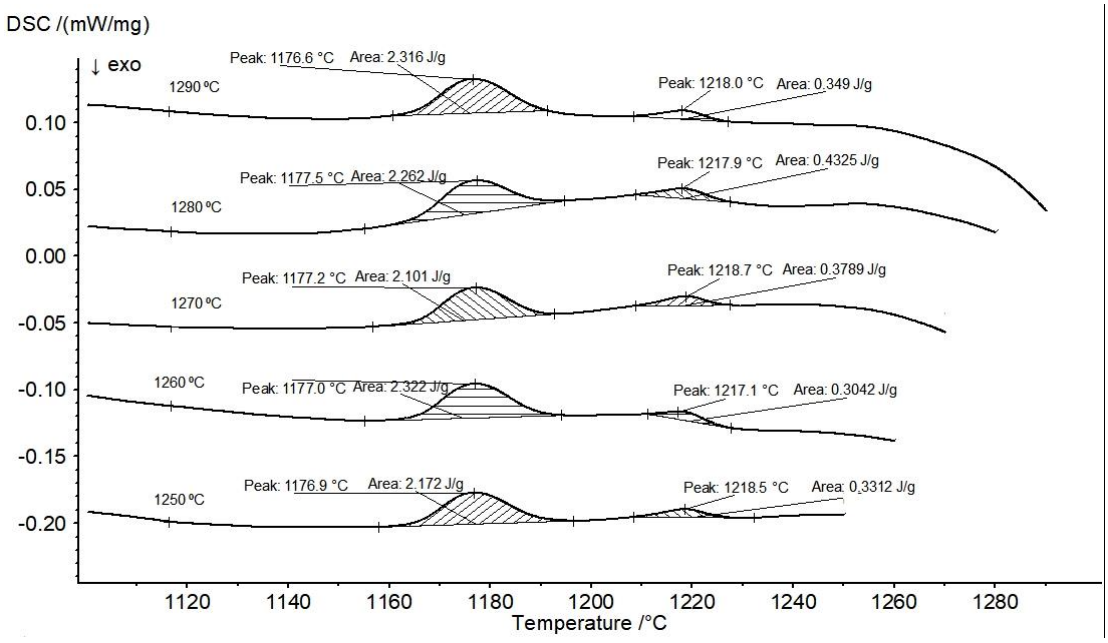

Figure 6-10. DSC thermal analysis during disordering reactions for the different trials

In contrast, the identification of the γ-phase dissolution temperature was more challenging because the endothermic process is shown as a negative slope on the DSC signal. This seems to be related to a difference in the specific heat capacity of the alloy once the decomposition of the lamellar microstructure starts. This change in the slope reveals the γ-phase dissolution temperature, which seems to begin at 1250 ºC (Figure 6-11), which is in agreement with the literature.

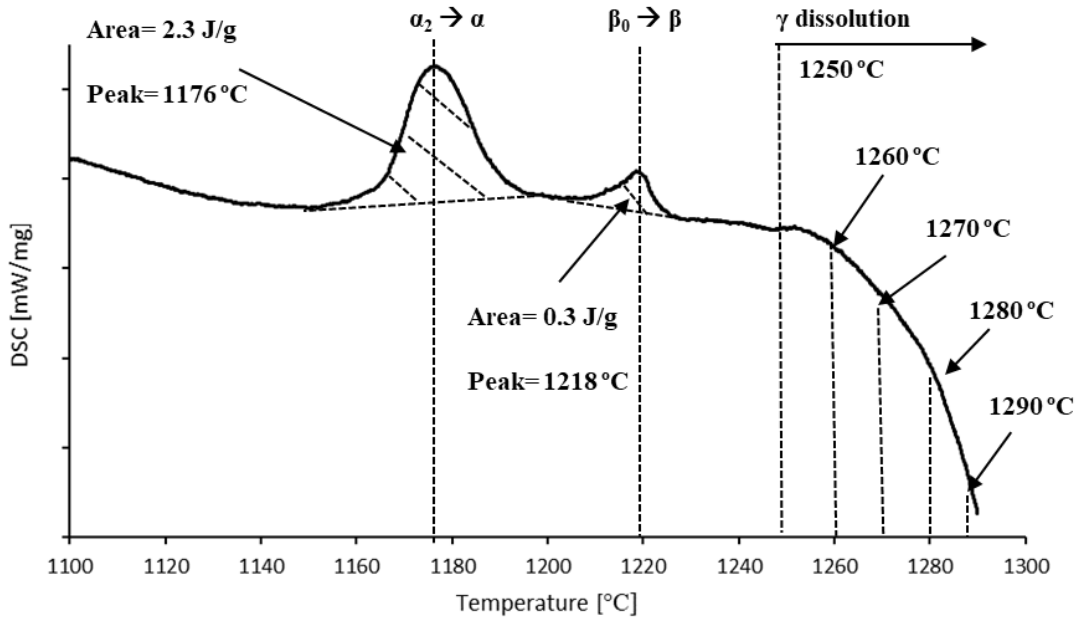

Figure 6-11. DSC thermal analysis during disordering reaction and partial dissolution of γ-phase upon heating

To determine the end of the γ-phase dissolution, the DSC signal of the isothermal step was analysed. In Figure 6-12 two signal peaks are plotted. The first is associated with isothermal drift stabilization and possible phase dissolution, caused by a change from raising the temperature to maintaining a constant temperature and the dissolution of the remanent γ-phase. The second peak corresponds to phase dissolution.

In the case of the first peak, in the trials performed at 1250 ºC and 1260 ºC, it can be seen that there is an overlap between thermal drift and phase dissolution, and no clear information could be obtained. This suggests that some amount of γ-phase dissolves during the isothermal step in both the 1250 ºC and 1260 ºC thermal profiles. At higher temperature HT, from 1270 ºC to 1290 ºC, there is no overlapped curve in the first peak, so no remaining γ-phase is expected to be dissolved. It can therefore be concluded that the dissolution kinetics of the γ-phase is higher for increased temperatures because the area below the curve is smaller at a higher temperature, and there is a reduction in the required time to dissolve the γ-phase.

Regarding the second peak, there is no signal for HT at 1250 and 1260 ºC. However, some signal can be detected from 1270 ºC to 1290 ºC, with the area reducing and the temperature increases. These signals appear to be related to phase dissolution but given the low intensity, they could correlate to some dissolution of the β-phase. For a better understanding, an image analysis technique was employed.

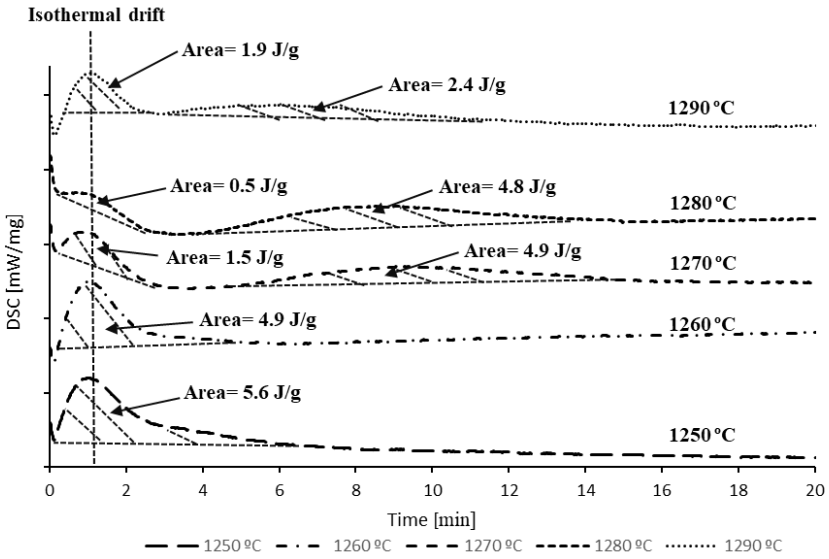

Figure 6-12. DSC thermal analysis for each sample during the isothermal step

Microstructure analysis

Figure 6-13 shows the microstructure of the resulting alloy in the as-cast state and after the corresponding HT. In the as-cast specimen, some small interlamellar areas with thick α_2/γ-plates surrounded by β-phase and globular γ-phase are visible. However, a large reduction of the β-phase was achieved by HT. In fact, lamellar spacing in all the heat-treated specimens was reduced, due to the low cooling rate from the HIP process. HT at temperatures above 1270 ºC does not provide any benefit, and instead increases processing time, as well as the incidence of γ-phase in the lamellae colony boundaries. Given that the microstructure was designed for structural applications like the widely used LPT blades in aeronautics, a nearly fully-lamellar microstructure was the target. Figure 6-13b shows that the HT at 1260 ºC provides little β-phase and enough globular γ-grains for this purpose.

The result from the image analysis reveals that the amount of β-phase in the reference as-cast state was around 4.8% in terms of area (Table 6-2). HT at 1250 ºC obtained a significant dissolution of the β-phase (0.5% of remaining β-phase), the remaining β-phase after the treatment at 1260 ºC was 0.1%, as was the case for the subsequent 1270 ºC, 1280 ºC and 1290 ºC treatments.

Table 6-2. Image analysis results, remaining %area of β-phase

Average %area of β-phase	**As-cast**	**1250 ºC**	**1260 ºC**	**1270 ºC**	**1280 ºC**	**1290 ºC**
Zone 1	4.7	0.4	0.1	0.2	0.1	0.1
Zone 2	4.9	0.6	0.1	0.2	0.1	0.1
Total	4.8	0.5	0.1	0.2	0.1	0.1

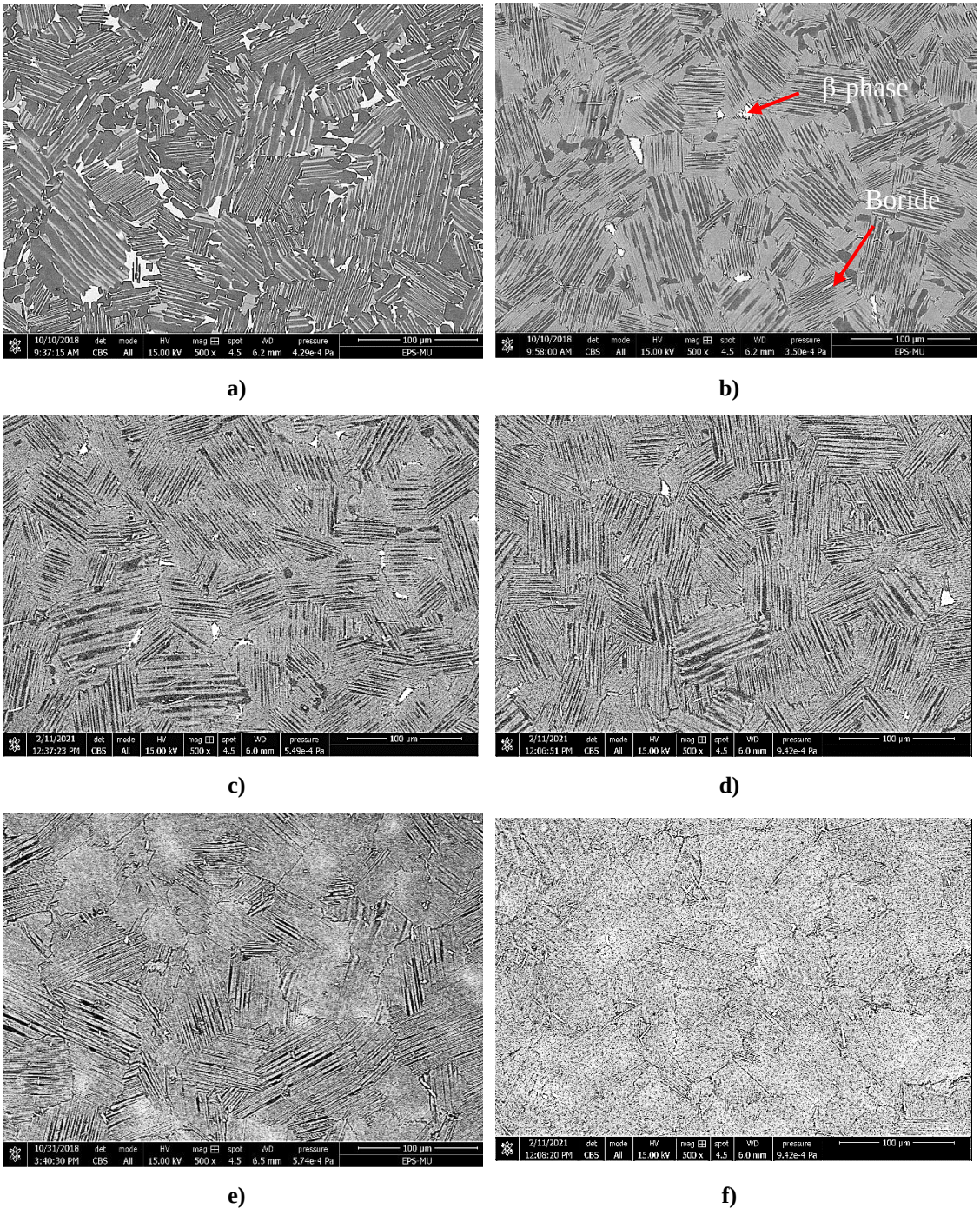

Figure 6-13. BSE images of the modified TNM alloy in the different states; a) As-cast, b) 1250 ºC, c) 1260 ºC, d) 1270 ºC, e) 1280 ºC and f) 1290 ºC

In summary, 1260 ºC can be considered the maximum HT temperature at which the β-phase is minimised and the γ-phase is properly precipitated, resulting in an alloy with a microstructure suitable for structural applications.

Development of the optimized microstructure through cooling rate control

Once the temperature of the HT is established, the cooling rate to precipitate a suitable lamellar microstructure must be determined. For this purpose, three different cooling rates are shown in Figure 6-14 for the selected 1260 ºC HT: 10 K/min, 30 K/min and 100-50 K/min. Those cooling rates are in the range between air and furnace cooling, which are the most common for precipitating the final microstructure for TNM alloys. The Figure 6-14 illustrates that the precipitation temperature of the γ-phase depends on the cooling rate. A cooling rate of 10 K/min starts precipitation at a temperature of 1255 ºC, one of 30 K/min starts at 1245 ºC, and of 100-50 K/min at 1236 ºC. The precipitation of the β-phase was not identified because there is no specific temperature, but rather a range. In fact, very little β precipitated during cooling (Table 6-2). As these results show, the cooling rate affects the phase precipitation kinetics, because high cooling rates lead to a decrease in the precipitation temperature of the globular γ-phase, which is confirmed in Figure 6-16.

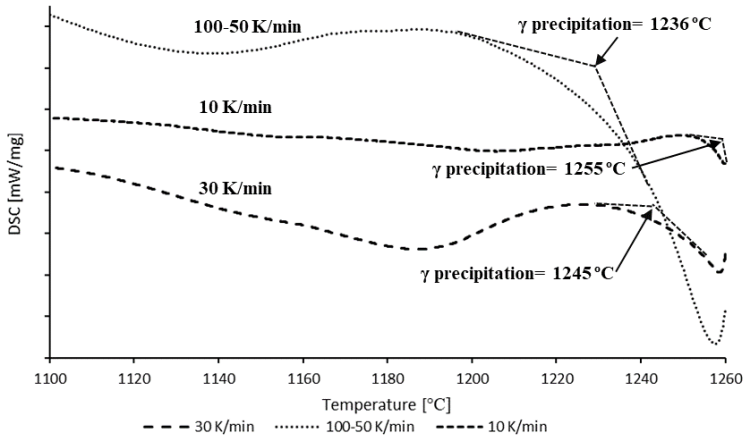

Figure 6-14. DSC thermal analysis of the cooling at different cooling rates

Regarding the size of the lamellar colony (Figure 6-15),

Table *6-3* shows that 75 µm was the average size for a cooling rate of 10 K/min, 64 µm for 30K/min, and 60 µm for 100-50 K/min. Therefore, all the cooling rates give rise to the desired lamellar colony size below 100 µm. These results support the fact that the higher the cooling rate, the smaller the lamellar colony size.

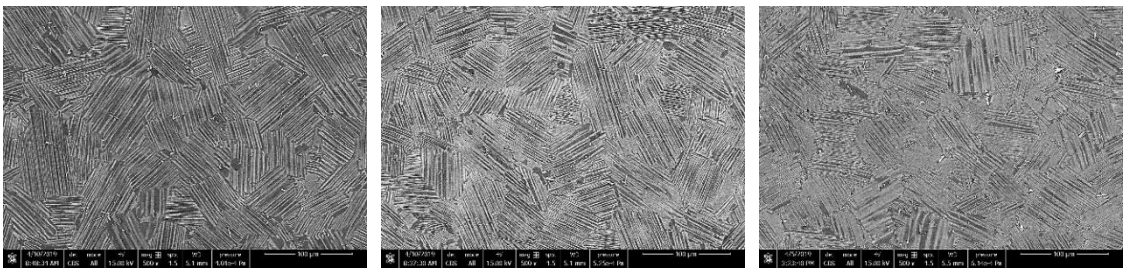

a) **b)** **c)**

Figure 6-15. Modified TNM heat-treated 1260 ºC X500; a) 10 K/min, b) 30 K/min and c) 100-50 K/min

Table 6-3. Results of the average lamellar colony size for each cooling rate at 1260 ºC HT

	10 K/min	30 K/min	100-50 K/min
Colony size [µm]	75 ± 14%	64 ± 18%	60 ± 12%

As regards lamellar spacing, Figure 6-16 shows that a cooling rate of 10 K/min provides a α_2/γ-lamellar spacing of 1.2 µm, a value which is above the desired limit of 1 µm for effective structural applications of TNM. Nevertheless, cooling rates of 30 K/min and 100-50 K/min produced lamellar spacings of 0.6 and 0.4 µm, respectively. Thus, these cooling rates are effective for producing a refined microstructure. The globular γ-grains located in the colony boundaries of the 100-50 K/min sample almost vanished, while those of the 10 K/min sample were too coarse. Interestingly, 30 K/min presented small globular γ-grains, which seems to provide balance in terms of creep strength and ductility [38]. In

Table 6-4, a summary of the results of the α_2/γ-lamellar spacing is shown.

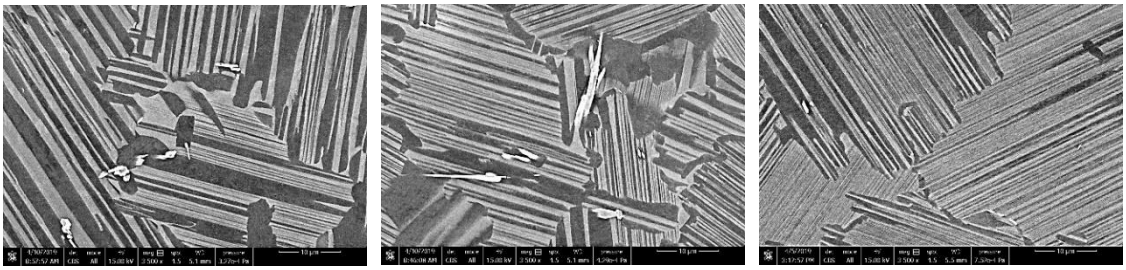

a) **b)** **c)**

Figure 6-16. Modified TNM heat-treated 1260 ºC X3500; a) 10 K/min, b) 30 K/min and c) 100–50 K/min

Table 6-4. Results of the average α2/γ-lamellar spacing for each cooling rate at 1260 ºC HT

	10 K/min	30 K/min	100-50 K/min
Lamellar spacing [µm]	1.25 ± 15%	0.58 ± 10%	0.39 ± 17%

The conventional forged TNM alloy consists of fine-grained lamellar α_2/γ-colonies with an average grain size of 25 µm and a lamellar spacing of 22 nm. It contains a 29 m% (mass percentage) α_2, 5 m% β_0 and 66 m% γ [62]. In contrast, the results of the present research is a modified TNM alloy with an average grain size of 64 µm and a lamellar spacing of 580 nm. It contains a 35 m% α_2, 65 m% γ and 0.1 m% β_0. Consequently, conventional and modified TNM alloys show differing mechanical properties, as a result of the difference in grain size and lamellar spacing, as well as the amounts of the different microconstituents.

Selected HT applied to the IHH process

Once the optimal HT was defined, the selected temperature vs time profile was applied to the newly developed TNM-1.5B in the IHH process.

The flat specimens subjected to the IHH process had dimensions of 20x10x3 mm, and were placed in the centre of the molybdenum furnace on a small alumina pedestal. The air was then evacuated and the chamber filled with Ar to atmospheric pressure, to create a protective atmosphere. Next, the IHH cycle defined in Figure 6-17 was applied to the newly developed TNM-1.5B-IHH. This cycle consists of the first stage of conventional HIPing under 200 MPa in Ar atmosphere and 1250 ºC for 3 hours, which greatly reduces the micro-porosity and macro-porosity arising from the casting process. This was followed by the second stage of HT at 1260 ºC for 1 hour with controlled cooling of 30 K/min to room temperature, in an Ar atmosphere at 200 MPa, which allows the development of the target microstructure.

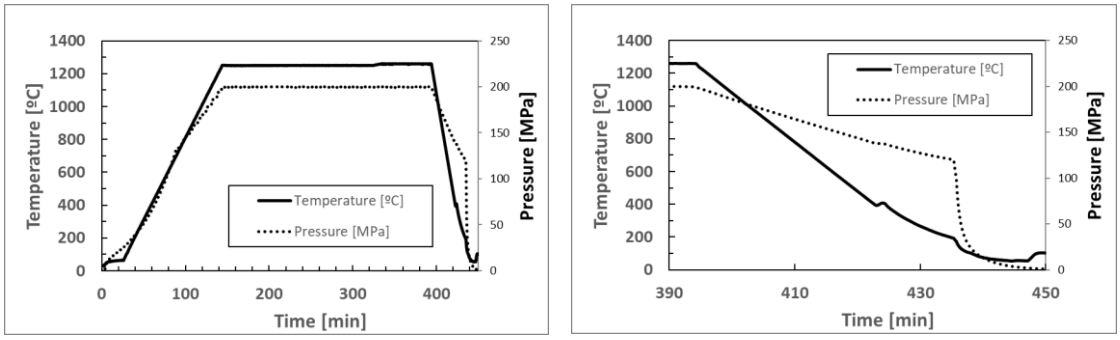

a) **b)**

Figure 6-17. IHH cycle applied to TNM-1.5B-IHH; a) General and b) Detail of the cooling

6.2.3 Conclusions

A novel HT from the cast/HIP state that reduces the processing time and costs was developed. It consists of a single-step heat-treatment in which TNM alloys can be improved according to the requirements of structural applications. The first step consists of conventional heating to the envisaged treatment temperature at a cooling rate of 10 K/min. Then, an isothermal step at 1260 ºC during 1 h is followed, which reduces the detrimental effect of the β-phase. Finally, a cooling rate of 30 K/min is applied to limit the precipitation of the γ-phase grains at the lamellae colony boundaries. Providing the most suitable microstructure for structural applications, by achieving a lamellar colony size below 100 µm and an α_2/γ-lamellar spacing below 1 µm, respectively. In addition, some small globular γ-phases located in the colony boundaries help increase ductility, eliminating the fragility associated with fully lamellar microstructures.

6.3 State of the Art of Creep

Creep is a time-dependent deformation under a certain applied load that generally occurs at high temperature. As a result, the material undergoes a time-dependent increase in length, which could be dangerous while in service. The first creep testing machine was created to test the peformance of materials for aircraft at high altitudes, temperatures and pressure. For this reason it is commonly used in the design of turbine blades. Figure 6-18 shows that the stress and temperature applied in the test play a significant role in creep curves. In general, a high temperature or high stress provide a reduced or even no secondary creep stage due to an accelerated creep rate, while low stress or low temperature gives rise to a long secondary creep due to a uniform strain rate [70].

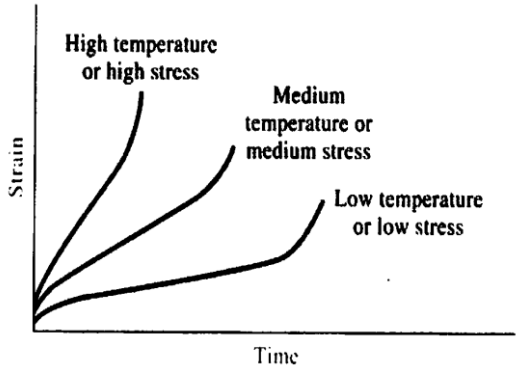

Figure 6-18. Effect of temperature and stress on the creep curves [70]

Stress rupture test is an accelerated alternative for the creep test. During the Stress rupture test, the time necessary for the material to fail under an overload is determined. Stress rupture test provides a measure of the ultimate load-carrying ability of a material as a function of time, while creep tests measure the load-carrying ability for limited deformation. The two tests complement each other but for alloying design creep is widely used while stress rupture test is commonly employed in the industry to test components [71]. Thus, in this investigation creep tests are employed for alloy design. In the following Figure 6-19 and Table 6-5 the main differences between both processes are summarized.

Table 6-5. Comparison between creep and stress rupture test

Test	Creep	Stress Rupture
Load	Low loads	High loads
Accuracy	Precision strain ($\varepsilon_f < 0.5\%$)	Gross strain (ε_f up to 50%)
Duration	Long term (2000-10000 h)	Short term (< 1000 h)
Cost	Expensive equipment	Less expensive equipment

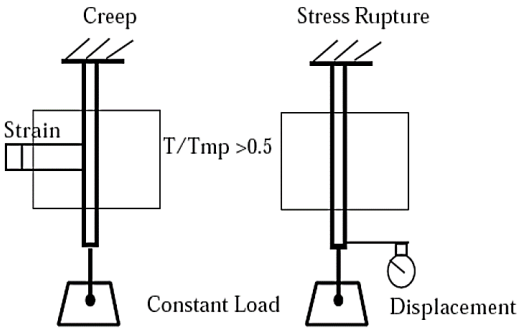

Figure 6-19. Creep vs stress rupture test [70]

Creep of materials relates time-dependent plasticity under fixed stress at an elevated temperature, and is usually performed 0.5 times above the melting temperature. The term "creep" is related to plastic deformation that occurs over time at a constant, and below yield stress of the metal.

The typical creep curve displays three consecutive stages (Figure 6-20). During the primary creep or stage I, the primary creep rate (plastic strain rate) decreases with increasing strain. During this stage, the material suffers hardening by dislocation movements. It is followed by the secondary creep, steady-state creep or stage II, in which under constant strain rate conditions the hardening compete with dynamic recovery. Work hardening comes from the accumulation of defects (dislocations, point defects or mechanical twins) that increases the stored energy of the material. While dynamic recovery consists of releasing this stored energy involving the annihilation of defects and rearrangement of dislocation. As a result, a balance between dynamic recovery and hardening is established, meaning that hardening reduces creep rate while dynamic recovery increases it. Finally, during the tertiary creep or stage III the fracture is reached, during which cavitation and/or cracking increases the strain rate or decreases the flow stress [9] [72] [1].

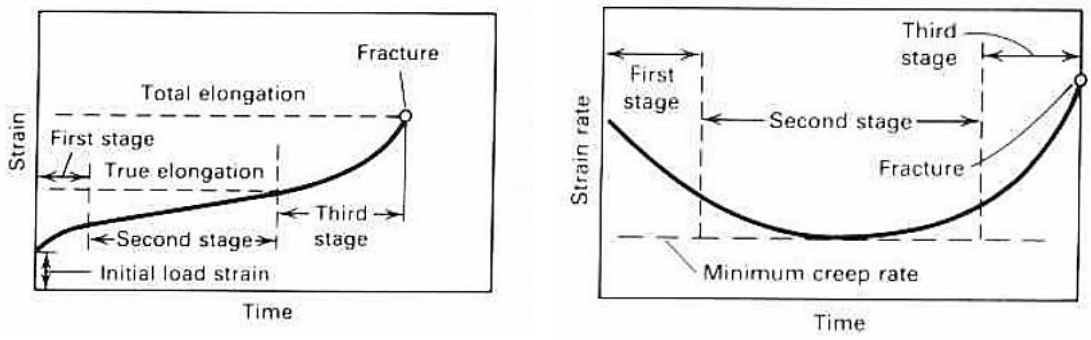

a) **b)**

Figure 6-20. Creep curves; a) Tension-creep curve, three stages of creep and b) Relationship of strain rate or creep rate, and time during a constant-load creep test [72]

The second stage steady-state or minimum creep rate is usually described by the power-law Equation 6-1:

$$\dot{\varepsilon} = \frac{d\varepsilon}{dt} = A\left(\frac{\sigma_a}{E}\right)^n \exp\left(-\frac{Q_C}{RT}\right) \qquad \textit{Equation 6-1}$$

$$n = (\Delta ln\dot{\varepsilon} / \Delta ln\sigma)_T \qquad \textit{Equation 6-2}$$

$$Q_C \equiv \Delta H = k\,T^2(\Delta ln\dot{\varepsilon} / \Delta T)_\sigma \qquad \textit{Equation 6-3}$$

Where E is Young's modulus at the creep temperature, n is the stress exponent, Qc is the activation energy, σ_a is the applied stress, and R is the universal gas constant. "A" is a microstructure-related material quantity that is assumed to be constant.

6.3.1 Creep of γ-TiAl

Titanium aluminides service at high temperatures and under high loads. Thus, the creep test is widely used to evaluate their performance. As seen in previous chapters, creep resistance in titanium aluminides vary on the microstructure. Fully lamellar (FL) microstructures have a higher creep strength than a duplex (DP) or nearly fully-lamellar / nearly lamellar (NFL / NL) microstructure (Figure 6-21) [9]. Creep of fully lamellar TiAl alloys appears to be controlled by lattice diffusion. Thus, it depends on Ti, in which atom movement occurs through the interchange of an atom in a crystal lattice site with a vacant site [73]. Microstructural parameters such as lamellar colony size, interlamellar spacing, lamellar orientation, precipitate volume fraction (γ/β in colony boundaries), and grain boundary morphology play a significant role in creep resistance.

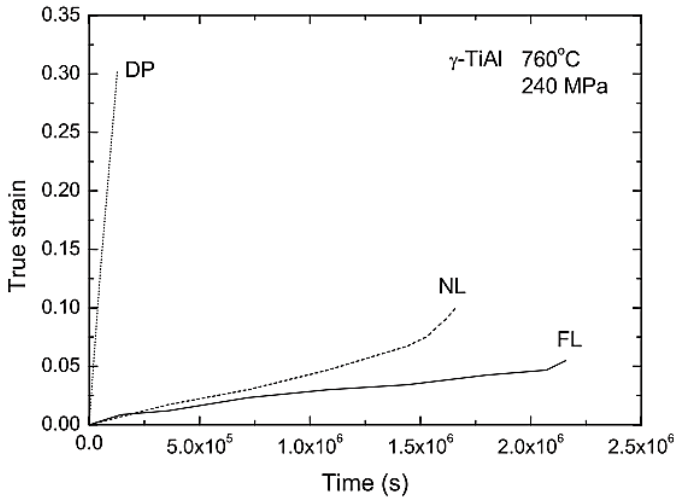

Figure 6-21. Creep curves at 760 ºC and 240 MPa of different microstructures of γ-TiAl [9]

A decrease in the lamellar interface spacing results in a reduction in the minimum creep rate (increasing creep resistance), since the mean free path for dislocations decreases and the dislocation density is lower [73]. Two mechanisms are suggested to increase creep resistance due to a reduction in the lamellar spacing. The first is related to the impediment of dislocation glide by a reduced interface spacing. The other is associated with a restriction in the dislocation motion parallel to α_2/γ lamellae, causing a bowing out of dislocation segments [74].

Creep resistance depends on the orientation angle between the loading axis and lamellar plane. There are two orientation models since the γ-phase is softer than the α_2-phase at high temperatures, the soft and hard mode. In the hard mode (angle close to 0º and 90º), deformation mainly occurs oblique to the lamellar interfaces. Thus, deformation happens across the twinning and dislocation activated in other γ laths, resulting in bowed lamellae. As a result, yield and fracture stresses are higher across the lamellae. In the soft mode (angle between 30-60º) however, deformation is carried out by slip parallel to the lamellar interfaces. Therefore, some lamellae deform by parallel twinning and others through dislocation slipping. In this case, the lamellae are not distorted, and yield and fracture stresses are lower when deformation takes place in the plane of the lamellae [74] [75] [47]. Hence in hard mode, the α_2/γ lamellae interfaces are effective barriers for twinning and hinder dislocation motion due to a small nm scale lamellar spacing. In soft mode colony boundaries provide a limited barrier for dislocation motion due to μm scale spacing [76].

Figure 6-22 illustrates the influence of the orientation angle between the lamellae and the loading axis for a given γ-TiAl that has a lamellar spacing of 520 nm. In this case, the hard mode provides a lower structural factor $B_\gamma(\Phi, \lambda)$, which results in lower creep rate [74].

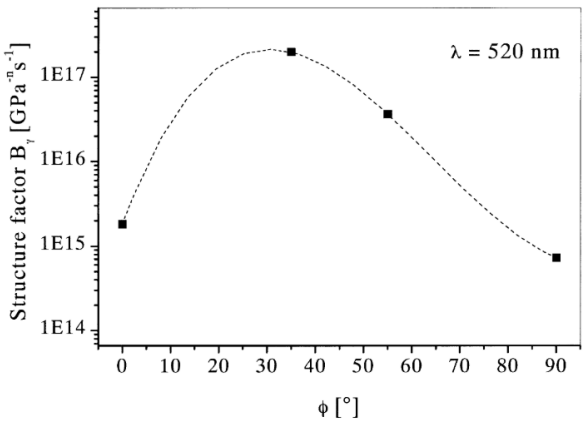

Figure 6-22. Influence of the orientation angle between the lamellae and the loading axis with the structure factor [74]

Alloying elements play a significant role in creep resistance. Refractory elements like W, Nb, Mo and V and interstitial elements like C, Si and N reduce creep rate due to the promotion of precipitation hardening or solution hardening.

Creep stages of γ-TiAl

Creep curves of TiAl alloys undergo three different stages. Primary creep in which the creep rate decreases with time, secondary creep or steady-state in which the creep rate remains constant, and tertiary creep in which creep rate increases with time.

Primary creep

Primary creep takes place in two stages, an instantaneous strain which occurs once the load is set, and a primary transient where the strain rate declines with time to minimum creep rate. In the case of fully lamellar γ-TiAl alloys, it is brought about by the relaxation constraint stresses due to the propagation and multiplication of interfacial dislocations. Indeed, crystal imperfections and inhomogeneities increase primary creep [1].

Secondary creep

During steady-state or secondary creep, the lamellar structure of TiAl alloys starts to decompose into the spheroidal microstructure because of DRX processes. The ensuing local deformation causes the metastable α_2 to partially dissolve, (predominantly from the α_2/γ interface) to form the γ phase. During this transformation, owing to the lower solubility of interstitial elements in the γ-phase, it is easier to reach the precipitation limit of oxides and other small elements. In fact, these insterstitial elements help to pin dislocations so creep strain rate is minimized, and ductility can thus be reduced [1] [77].

It is also important to note that the decomposition of the α-phase into lamellar α/γ during cooling is sluggish, and consequently the γ phase is below equilibrium. Therefore, high-temperature creep is expected to shift phase-field towards equilibrium, with the result that α_2 transforms to γ [34]. In Figure 6-23, the evolution process of the α_2/γ lamellar structures during creep is depicted [33].

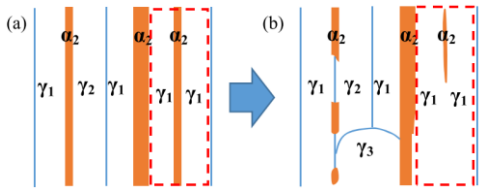

Figure 6-23. Microstructural degeneration of α_2/γ lamellae; a) Initial morphology and b) After creep testing [33]

Where:
γ_1, γ_2, γ_3 have similar compositions with different crystal orientations
γ_1, γ_2 are pseudo-twin relations
γ_3 results from the creep-induced recrystallization γ phase

Tertiary creep

Tertiary creep commonly starts at 2 to 3% strain in TiAl alloys with a rapid increase of creep rate due to large strain accumulation. Thus, tertiary creep occupies a large portion of the total creep life of TiAl alloys. The mechanisms associated with tertiary creep are a progressive increase of the dislocation density and DRX. The main factor that accelerates creep rate in TiAl alloys is microstructure degradation related to phase transformation and DRX, rather than void formation and necking which are delayed until the last stages of creep [1] [76].

6.3.2 Creep of TNM

The third generation of γ-TiAl TNM alloys exhibit improved creep behaviour and enhanced high temperature performance compared to the second-generation Ti-48Al-2Cr-2Nb. However, their operating temperature has an upper limit of 750 ºC due to microstructural instability, which is associated with a strong chemical composition disequilibrium ($(\alpha_2+\gamma)_{fine} \rightarrow (\alpha_2+\beta_0+\gamma)_{coarse}$) (Figure 6-24). With long exposure to a high temperature, discontinuous precipitation or cellular reaction takes place due to an increase of the lamellar interface energy. This promotes the breakdown of the lamellar colonies [65]. Consequently, coarser lamellar structures are precipitated, resulting in lower yield strength and higher plastic deformation, while creep properties are worsened [67].

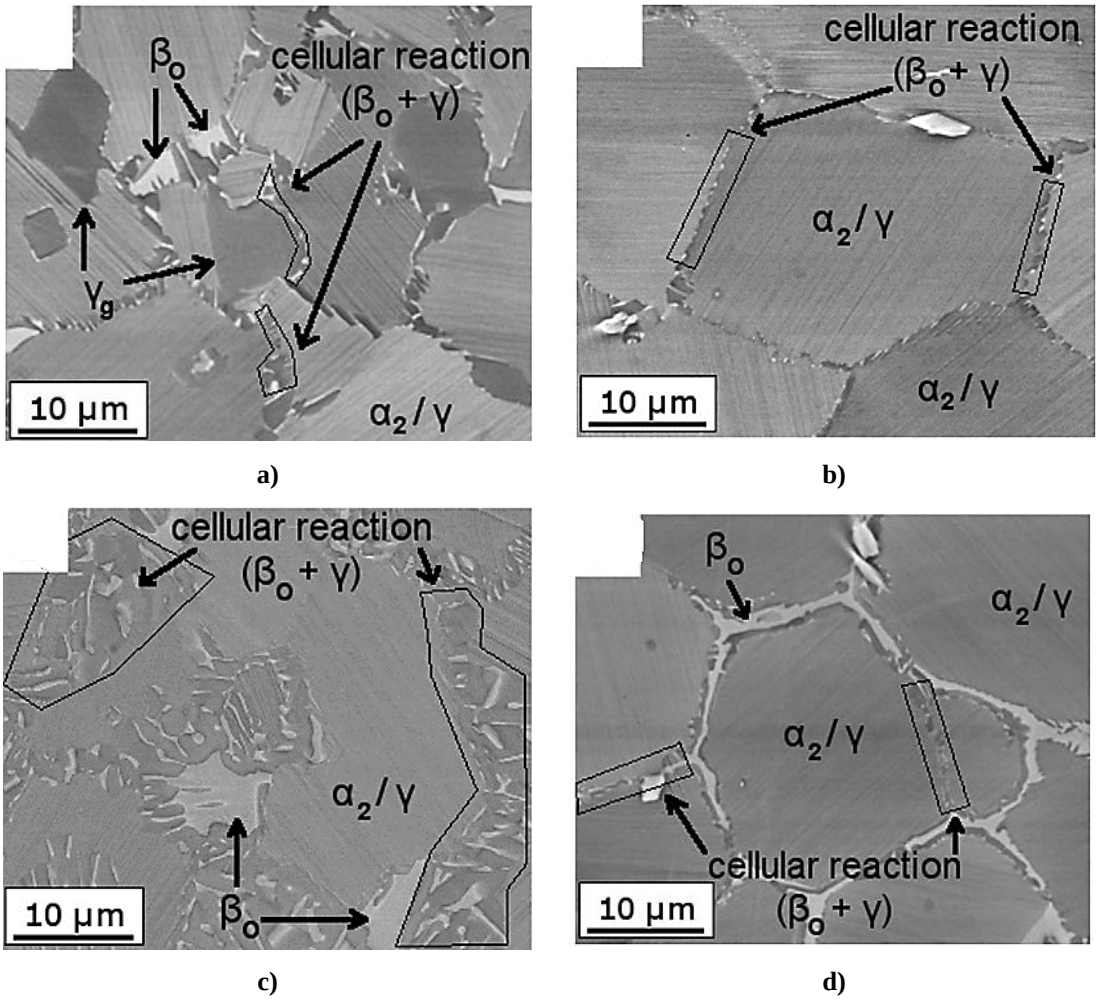

Figure 6-24. The cellular reaction of TNM alloys with different microstructures; a) Nearly lamellar + γ, b) Nearly lamellar + β, c) Nearly lamellar + β and d) Nearly lamellar + high β [78]

In the case of the abovementioned for TiAl systems, the parameter commonly employed to define creep behaviour is the minimum creep rate. This minimum creep rate is mainly controlled by the strain hardening that takes place during the first stage of creep, in which a decrease in lamellar spacing improves the minimum creep rate by lowering it.

Thus, fully lamellar with small lamellar spacing microstructures have the potential to improve creep resistance, (Figure 6-25) [79] [80]. This however, is at the expense of ductility, and a balance between creep strength and ductility should be established (discussed in Chapter 3).

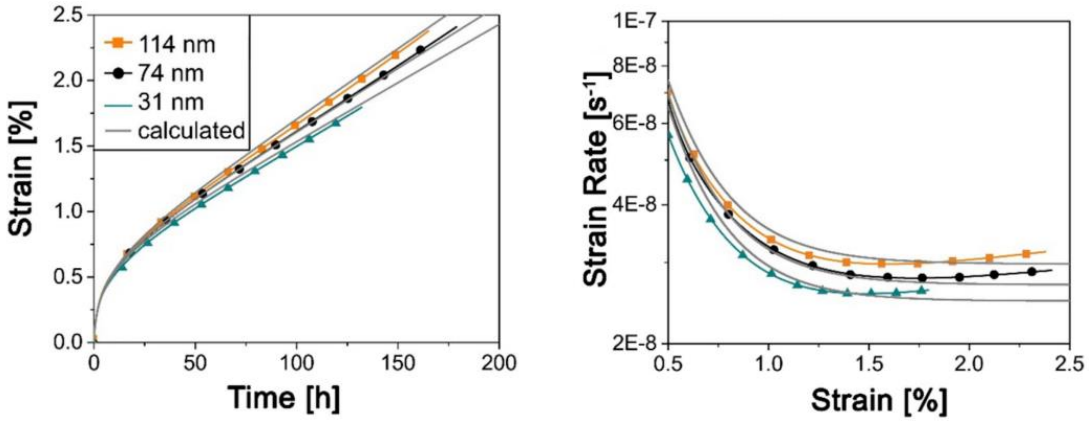

Figure 6-25. Creep of TNM⁺ with different lamellar spacings; a) and b) [79]

In Figure 6-26 microstructure is related to the creep strength of a TNM alloy. A nearly lamellar microstructure with β_0-phase and globular γ-phase ($NL_{\gamma+\beta_0}$) presents the highest creep strain. It is related to a β_0-phase that facilitates diffusional processes at elevated temperatures and reduces the sliding resistance of grain boundaries, owing to the less densely packed BCC crystal structure. In contrast, a nearly lamellar microstructure with no β_0 enhances the creep strength. Finally, a fully lamellar microstructure provides the lowest creep strain rate and increases the component lifetime, as a result of the elimination of globular γ-phase that promotes dislocation movements on the grain boundaries [62].

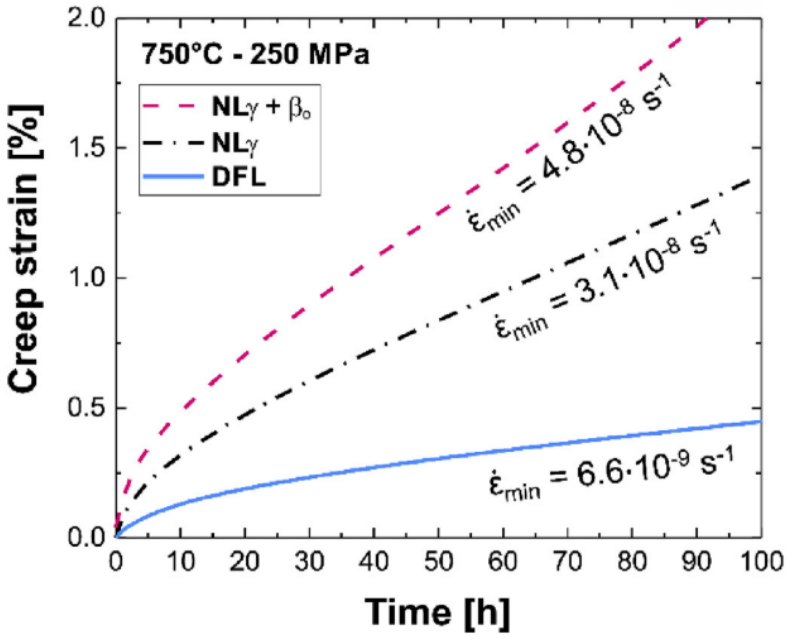

Figure 6-26. Creep curves at 750 ºC and 250 MPa for different microstructures of a TNM alloy[62]

To improve the creep behaviour of TNM alloys, certain alloying elements such as Si and C prove to be beneficial, the so-called TNM$^+$. This is achieved by reducing dislocation motion and enhancing microstructural stability [67]. C increases strength and creep resistance, through solid solution hardening or by forming precipitates. However, C shifts the solidification pathway from β to peritectic solidification, inducing segregations and coarser grain. This can be restored to β-solidifying through an increase in Nb and Mo, or by reducing the content of Al. Si acts as a solid solution hardener and promotes the formation of precipitates [12]. Figure 6-27 shows a comparison of the creep behaviour of the abovementioned alloys.

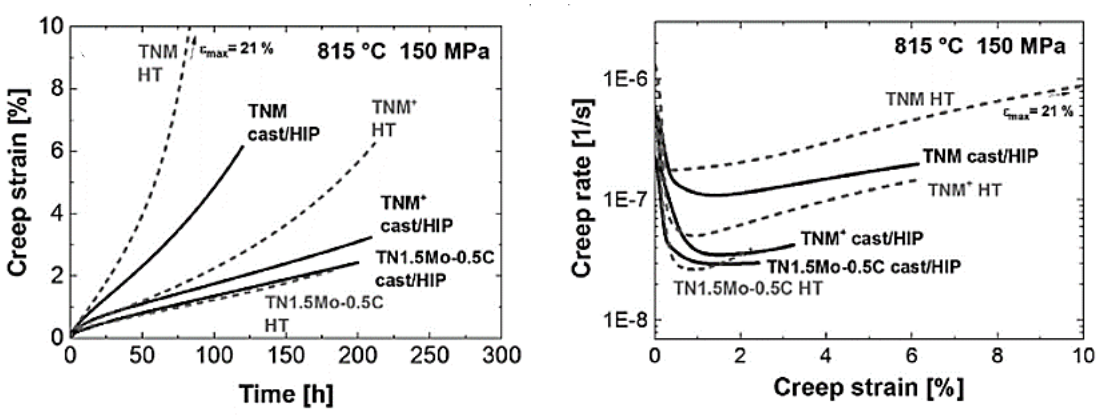

a) **b)**

Figure 6-27. Creep properties of several TNM alloys in cast/HIP and heat-treated condition at 815 ºC and 150 MPa; a) Creep strain vs time and b) Creep rate as a function of creep strain [67]

6.4 Validation of the microstructure by creep tests

Once the HT that generates the desired microstructure is designed and applied to the specimen, its behaviour is evaluated with the creep test. To this end, a comparison between three different samples was made. The first sample, "TNM-0.8B-HIPIMR" is the TNM-0.8B in the cast/HIP state, which is considered as the starting point. The second sample, "TNM-0.8B-HIPIMR-HT" is the TNM-0.8B in the cast/HIP/HT state, in which the selected HT is already applied. Finally, the third sample, "TNM-1.5B-IHH" is the TNM-1.5B in the cast/IHH state. The latter is the newly developed chemical composition described in Section 5.3, integrating HIP and the selected HT of Section 6.2 into a single process called IHH. In addition, this newly developed TNM-1.5B with IHH was compared against the reference alloy, the conventional TNM manufactured by forging.

6.4.1 Manufacturing route for the creep tested samples

The samples tested at creep were manufactured by casting.

TNM-0.8B-HIPIMR and TNM-0.8B-HIPIMR-HT were manufactured using a plasma arc furnace to produce PAM ingots that were subsequently re-melted using an ISM unit. These ingots were then melted again in an induction skull furnace in a vacuum and poured into an yttrium-based ceramic mould with a stepped plate geometry. The mould was heated to 600 ºC and rotated during pouring to create a centrifugal force, which helped fill the mould cavity with the metal without misruns or severe shrinkage. Finally, both samples were subjected to HIP at 200 MPa in Ar atmosphere and 1270 ºC for 4 hours to reduce the microporosity arising from the casting process. Only sample TNM-0.8B-HIPIMR-HT was subjected to the selected HT at 1260 ºC for 1 hour with controlled cooling of 30 K/min to room temperature, in an Ar atmosphere at 20 MPa.

The novel modified TNM-1.5B-IHH alloy was manufactured by casting plus an integrated HIP/HT cycle, as follows: First, the billets of TNM master alloy were manufactured by melting the feedstock materials, combining VAR skull melting with centrifugal casting in permanent moulds, which provided homogeneous and fine-grained microstructure. Then, the billets of TNM master alloy were melted in an ISM furnace and cast into a ceramic mould at a controlled cooling rate of around 10 K/s to achieve a homogeneous microstructure with the precipitation of the beneficial blocky boride, as described in Section 5.3. Afterwards, the as-cast sample was subjected to an IHH that integrates the HIP with HT. This was achieved by HIPing at 1250 ºC for 3 h at 200 MPa in Ar atmosphere, followed by a HT at 1260 ºC for 1 h at 200 MPa in Ar atmosphere, finishing with a cooling rate of 30 K/min to room temperature. This allowed accelerated thermomechanical processing of the alloy, to obtain the final part. Table 6-6 summarises the processing of the three samples.

Table 6-6 Manufacturing and processing routes of the creep tested samples

Sample	Casting route	HIP	HT
TNM-0.8B-HIPIMR	PAM + ISM	200 MPa Ar, 1270 ºC, 4 h, slow cooling	None
TNM-0.8B-HIPIMR-HT	PAM + ISM	200 MPa Ar, 1270 ºC, 4 h, slow cooling	1260 ºC, 1 h, 20 MPa Ar, cooling at 30 K/min
TNM-1.5B-IHH	VAR + ISM	Integrated: 1250 ºC, 3h, 200 MPa Ar & 1260 ºC, 1 h, 200 MPa Ar, 30 K/min	

6.4.2 Creep test of the samples

Samples microstructure

The microstructure of the three samples tested at creep (Figure 6-28) differ considerably as a result of the different processing. TNM-0.8B-HIPIMR exhibits many big globular γ-grains and large β-phase areas along colony boundaries, with a fairly thick lamellar spacing. TNM-0.8B-HIPIMR-HT shows a refined lamellar spacing with less and smaller γ and β in the colony boundaries. In TNM-1.5B-IHH almost no β and few small globular γ-grains, with narrow lamellar spacing can be observed.

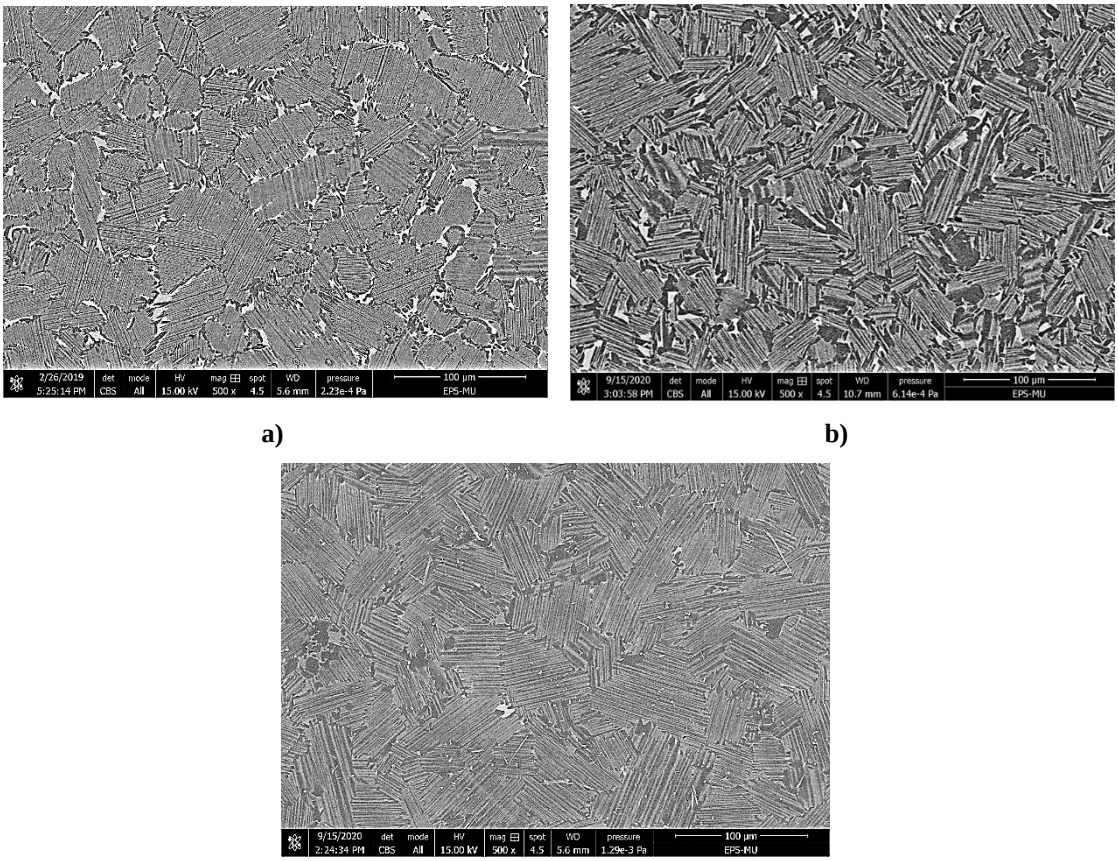

a) **b)**

c)

Figure 6-28. SEM; a) TNM-0.8B-HIPIMR, b) TNM-0.8B-HIPIMR-HT and c) TNM-1.5B-IHH

Creep test set up

The three samples were tested using a Denison-Mayes-Group creep testing machine from Ruhr Universität Bochum [81]. Type TC 20 Mark II with three-zone resistance furnace up to 1200 ºC was used, temperature control was based on up to three Type S PtRh/Pt-thermocouples with PtRh-shell. The creep specimen with dog bone geometry had a measurement length of 9 mm and a thickness of 2 mm, as Figure 6-29 shows.

a) **b)**

Figure 6-29. Creep; a) Sample dimensions and b) Creep unit

Creep results

Creep results of the three samples are shown in Figure 6-30. It can be observed that the three samples present a similar behaviour during the primary creep. However, during the secondary creep, sample TNM-1.5B-IHH exhibits enhanced creep resistance compared to the other two samples, which is reflected in the ε_{min} value. During secondary creep, TNM-0.8B-HIPIMR recorded a ε_{min} of $7.8.10^{-8}$ s^{-1}, TNM-0.8B-HIPIMR-HT of $6.4.10^{-8}$ s^{-1} and TNM-1.5B-IHH of $4.8.10^{-8}$ s^{-1}. TNM-1.5B-IHH also had quite a longer secondary creep life than both the other samples, before reaching the exponential deformation typical of tertiary creep that ends with the material failure.

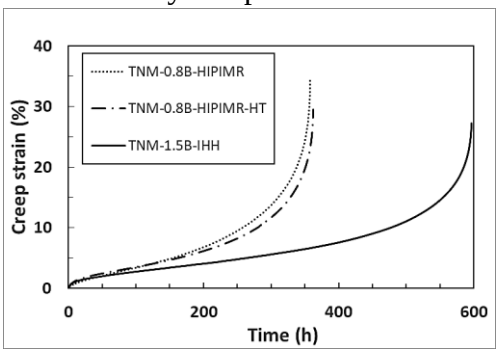

a)

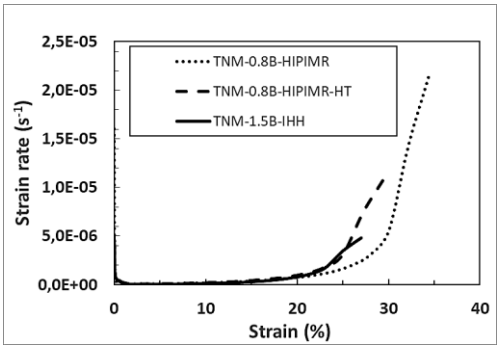

b)

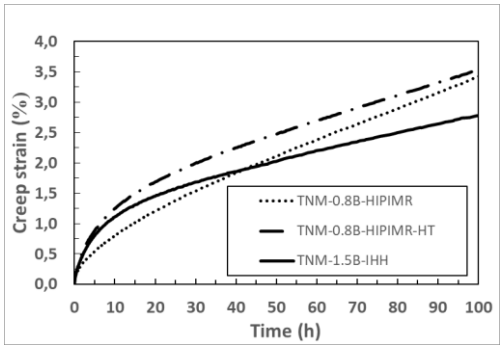

c)

Figure 6-30. Creep of the three manufactured samples; a) Creep strain, general, b) Strain rate and c) Creep strain, detailed

In terms of microstructural evolution during the creep test, the lamellas started to decompose due to DRX during the secondary creep [1] [77]. Figure 6-31 shows the microstructure before and after the creep test of the three specimens. It can be seen in Figure 6-31b (TNM-0.8B-HIPIMR) that the lamellae colony boundaries decomposed to form newly precipitated coarsened γ and β-phases from the metastable α_2-phase, but there is less evidence of this in Figure 6-31d (TNM-0.8B-HIPIMR-HT) and Figure 6-31f (TNM-1.5B-IHH). Therefore, as time passes there is an increase in the strain rate due to loss of strength as Figure 6-30b depicts during secondary creep, and particularly noticeable in the TNM-0.8B-HIPIMR.

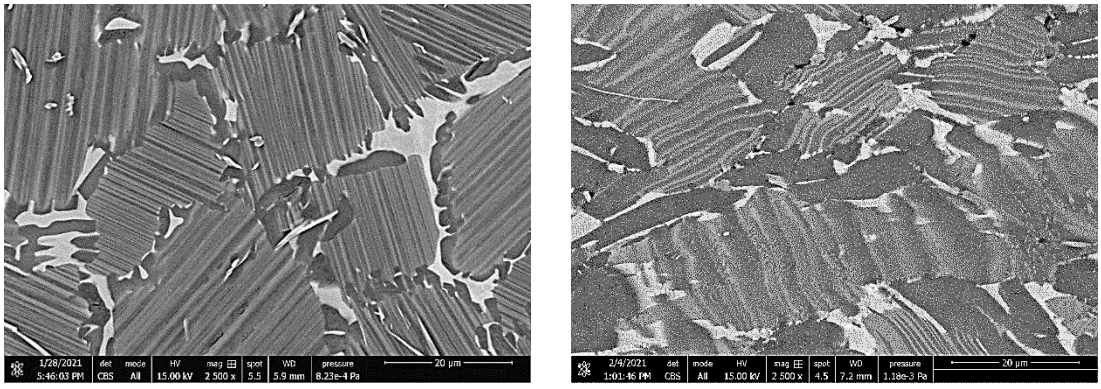

a)

b)

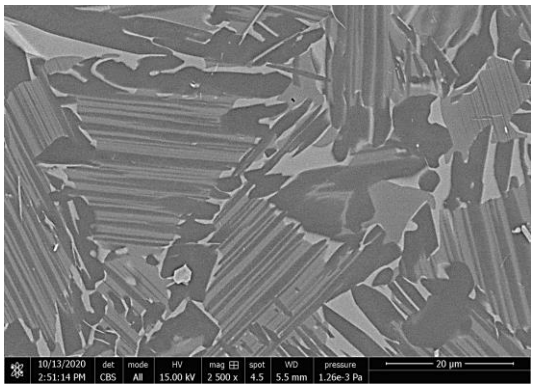

c)

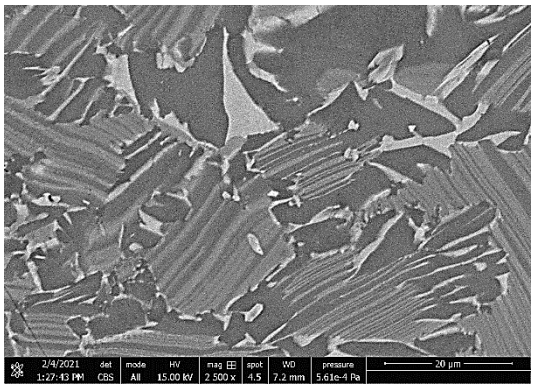

d)

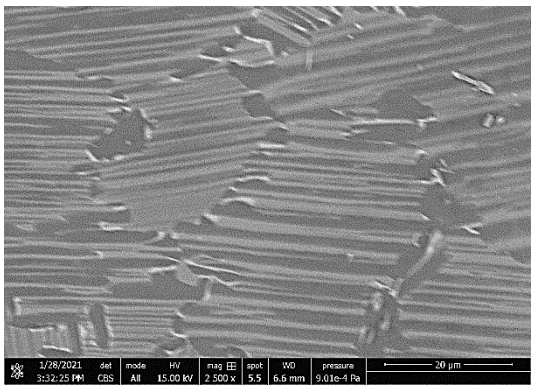

e)

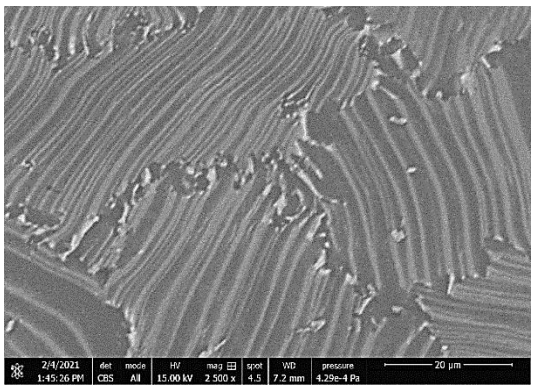

f)

Figure 6-31. SEM; a) TNM-0.8B-HIPIMR pre-creep, b) TNM-0.8B-HIPIMR post-creep, c) TNM-0.8B-HIPIMR-HT pre-creep, d) TNM-0.8B-HIPIMR-HT post-creep, e) TNM-1.5B-IHH pre-creep, f) TNM-1.5B-IHH post-creep

As regards the type of failure for the TNM-0.8B-HIPIMR, Figure 6-32a shows that at room temperature the failure is brittle, while the failure during the creep test at 750 ºC is ductile (Figure 6-32b). This suggests that the sample was tested at a temperature above the BDTC [33].

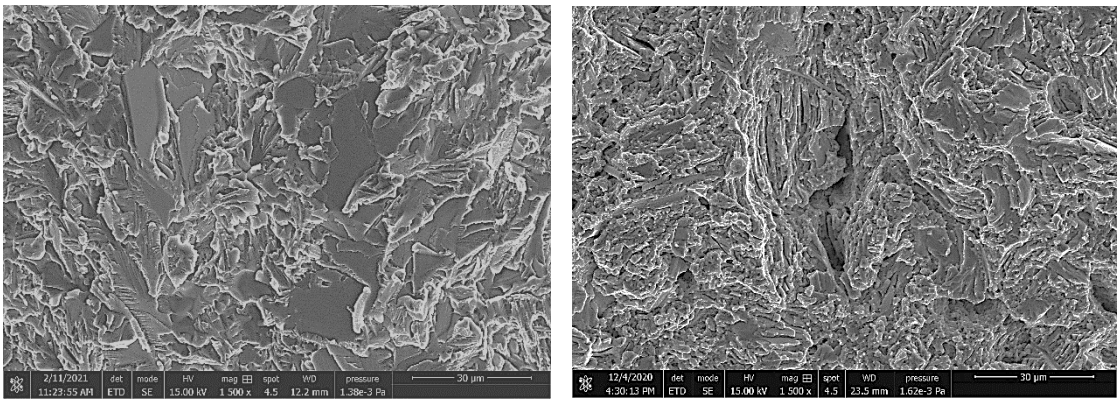

a) **b)**

Figure 6-32. SEM; a) TNM-0.8B-HIPIMR pre-creep fracture and b) TNM-0.8B-HIPIMR post-creep fracture

From these results it can be concluded that the sample TNM-1.5B-IHH displays a superior creep strength to the other samples. This is achieved by adjusting the chemical composition and solidification cooling rate to provide the beneficial as-cast microstructure described in Section 5.3, in which a homogeneous microstructure with a large number of blocky borides is precipitated.

6.4.3 Comparison between cast modified TNM and reference forged TNM

Once the enhanced cast modified TNM (TNM-1.5B-IHH) was fully developed from casting to the final part, it was compared against the conventional forged TNM alloy (Ref TNM-Forged-NLGB) (Table 6-7). The newly developed processing route was designed to improve the creep strength while significantly reducing the processing time of the alloy.

Table 6-7. Chemical composition of the samples tested at creep

Concentration (at.%)	Ti	Al	Nb	Mo	B
Ref TNM-Forged-NLGB	Bal.	43.7	4.1	1.0	0.095
TNM-1.5B-IHH	Bal.	42.5	3.5	0.9	1.5

The novel modified TNM-1.5B-IHH alloy was manufactured as described in Section 6.4.1. To manufacture conventional TNM-Forged-NLGB forged alloys, a series of processes are required involving casting, forging, HIPing and multi-step HT: First, the TNM alloy was double melted using VAR to achieve chemical homogeneity. Then, the homogenized electrodes were melted in a VAR skull melter and cast into billets via spin casting in permanent moulds. These ingots were subjected to HIPing at 1200 ºC for 4 h at 200 MPa in Ar atmosphere. Subsequently, the billets were hot-die forged and then subjected to a three-step HT to achieve a homogeneous microstructure [62]. This was achieved through first homogenization annealing, then high-temperature annealing in the ($\alpha + \beta + \gamma$) phase field, plus a stabilization annealing, as depicted in Figure 6-33.

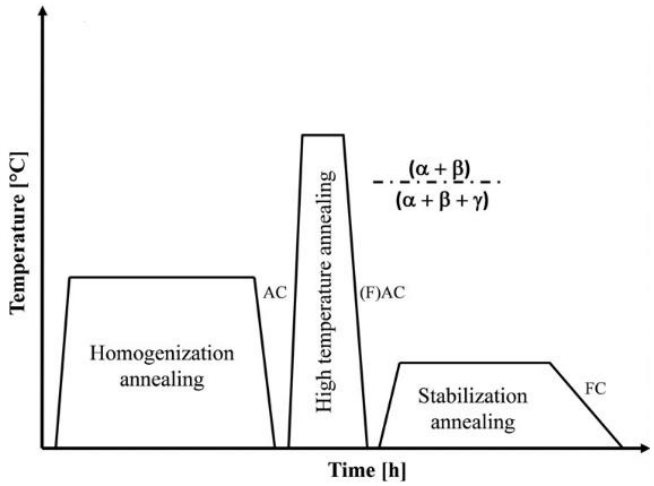

Figure 6-33. Three-step HT of the conventional forged TNM alloy [82]

Once manufactured, the microstructure of both samples was analysed to understand the effect of the type and quantity of the different micro-constituents on creep strength. The conventional TNM-Forged-NLGB consists of a fine-grained lamellar α_2/γ-colonies with an average grain size of 25 µm and a lamellar spacing of 22 nm, including a 29 m% (mass percentage) α_2, 5 m% β_0 and 66 m% γ [62]. The novel modified TNM-1.5B-IHH consists of a nearly fully-lamellar microstructure with an average grain size of 65 µm and a lamellar spacing of 580 nm, including around 35 m% α_2, 65 m% γ and 0.1 m% β_0.

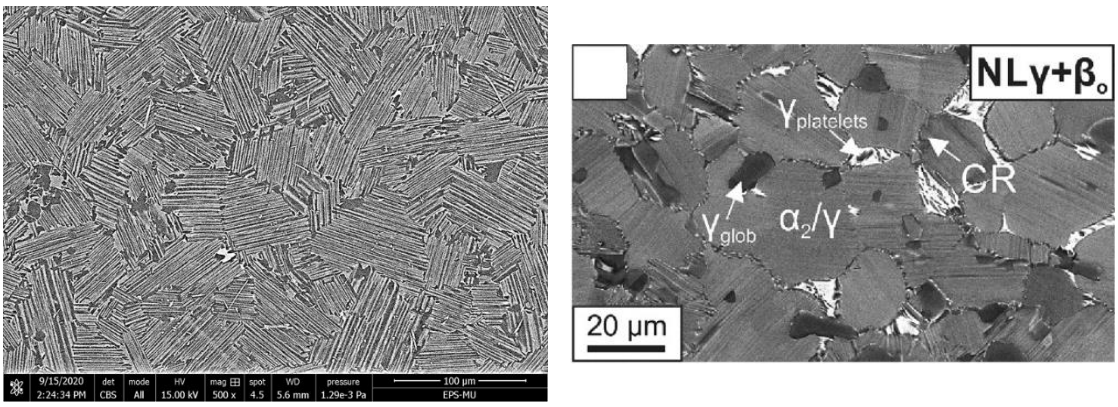

a) **b)**

Figure 6-34. BSE image showing microstructure; a) TNM-1.5B-IHH and b) TNM-Forged-NLGB [62]

The novel modified TNM-1.5B-IHH was tested at creep as described in Section 0. The conventional TNM-Forged-NLGB, was tested using a TC30 creep testing apparatus from AET Technologies, France. The specimen had an initial gauge length of 30 mm and an initial diameter of 6 mm, and the elongation during exposure was measured by inductive displacement sensors in a differential circuit [62].

Figure 6-35 shows the creep test of both the novel modified TNM-1.5B-IHH and the conventional TNM-Forged-NLGB, conducted at 750 ºC and initial stress of 250 MPa. It can be observed that TNM-Forged-NLGB had a lower strain during primary creep than TNM-1.5B-IHH. However, during secondary creep in which the ε_{min} describes the behaviour of this region, both alloys displayed a similar minimum creep rate, with values of $4.8.10^{-8}$ s^{-1} for the TNM-1.5B-IHH and of $4.9.10^{-8}$ s^{-1} for the TNM-Forged-NLGB.

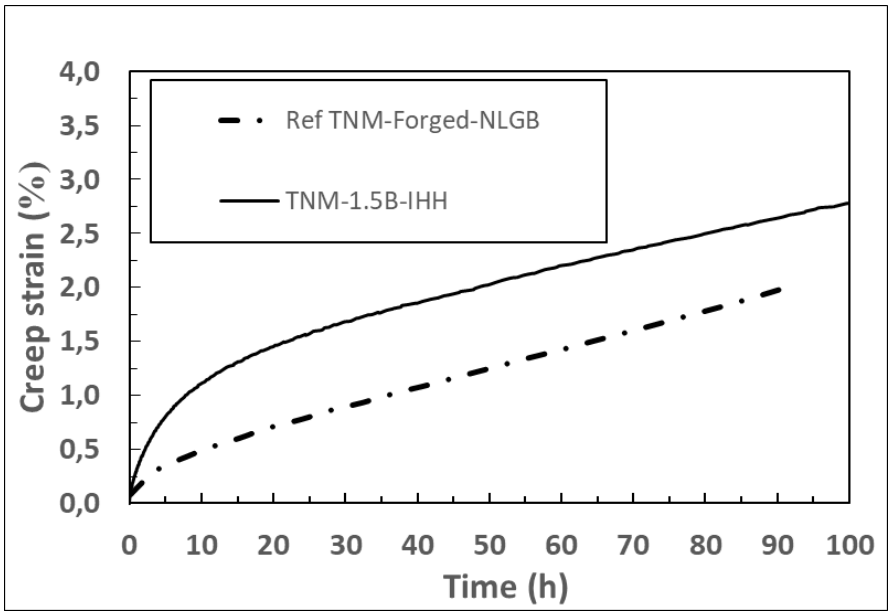

Figure 6-35. Creep curves at 750 ºC and 250 MPa of both novel modified TNM IHH and conventional TNM forged

Consequently, cast modified TNM-1.5B-IHH has achieved similar creep strength to conventional forged TNM-Forged-NLGB, despite having a larger grain size and a thicker lamellar spacing than the conventional TNM alloy. This good creep behaviour could be related to the lower presence of the soft β-phase, as the α_2-phase offers a higher stiffness.

6.4.4 Conclusions

The results reveal that the newly developed modified TNM-1.5B-IHH alloy has improved creep strength in comparison to both the other tested alloys. This is achieved by adjusting the chemical composition and solidification cooling rate to provide the beneficial as-cast microstructure described in Section 5.3, in which a homogeneous microstructure with a large number of blocky borides is precipitated. Through the casting/IHH manufacturing route, the creep results are promising, achieving enhanced minimum creep rate and creep life, at 750 ºC and under a load of 200 MPa.

In comparison with the conventional processing of TNM alloys, the novel TNM-1.5B-IHH manufactured by casting/IHH presents advantages over the conventional thermomechanical processing of forged TNM alloys. This new manufacturing route opens up the possibility of faster manufacturing, which could result in more cost-effective TiAl components. Furthermore, the new casting manufacturing route could allow components with more complex geometries to be obtained than forging, increasing the potential portfolio of manufacturers. At the same time, the machining operations required to achieve the final dimensional tolerances can be greatly reduced, resulting in lower operating costs and less material wastage.

These are early stage results, however they do demonstrate the considerable potential of the cast/IHH route if both the chemical composition and the alloy solidification condition are optimised, in conjunction with HIPing and suitable HT design.

6.5 Conclusions

To conclude this chapter, it has been established that TNM alloys in the as-cast state have limited mechanical properties due to their microstructure. To meet the stringent requirements of aeronautics components, thermomechanical processing is therefore essential. Firstly, HIP is performed to reduce the microporosity arising from the casting process. Then, the typical procedure is forging and applying the corresponding HT.

In conventional processing, TNM alloys are subject to forging. The subsequent HT step is a solution HT conducted above the γ-solvus temperature followed by air cooling, in which the lamellar microstructure is decomposed to precipitate a new one. During the second HT, the annealing procedure is typically conducted slightly above the envisaged service temperature. During this stage γ-lamellae precipitate in the supersaturated α_2 grains which originated in the previous HT.

In this work, a novel HT has been developed from the as-cast state that reduces the processing time and costs. It consists of a single-step HT design in which TNM alloys can be improved to meet the requirements of structural applications. The first step is conventional heating to the envisaged treatment temperature at a cooling rate of 10 K/min. Then, an isothermal step at 1260 ºC during 1 h is followed, which reduces the detrimental effect of β-phase and limits the precipitation of the γ-phase grains at the lamellae colony boundaries. Finally, a cooling rate of 30 K/min is applied. This achieves a lamellar colony size below 100 μm and an α_2/γ-lamellar spacing below 1 μm. In addition, some small globular γ help increase ductility, eliminating the fragility associated with fully lamellar microstructures. This develops a microstructure suitable for structural applications.

As a result of this research, a novel single-step HT for the Cast/HIP state suitable for structural applications was designed. To ensure that the developed microstructure performs successfully, creep tests were conducted.

The creep results reveal that the novel TNM-1.5B-IHH alloy modified through the cast/HIP process has improved creep strength in comparison with the other tested alloys. This is achieved by adjusting the chemical composition and solidification cooling rate to provide the beneficial as-cast microstructure described in Section 5.3, in which a homogeneous microstructure with a great number of blocky borides is precipitated.

Finally, in addition to producing TiAl components with similar mechanical properties, the novel TNM-1.5B-IHH manufactured by casting/IHH presents advantages over the conventional forged TNM alloy. This new manufacturing route presents the opportunity to reduce processing time and cost by eliminating the forging process and integrating the HIP and HT processes into a single IHH process. Furthermore, components with more complex geometries than those obtained by forging could be produced, while machining operations and material wastage would be reduced.

It should be noted that these results are somewhat preliminary, as the IHH process conditions have not yet been fully optimised for the alloy tested. Furthermore, there is limited scientific evidence of the effect of the IHH process on metallic alloys, and less so for TiAl alloys. Nonetheless, the results obtained in this work do show the potential of this process to deliver improved mechanical properties with higher efficiency, once the suitable process conditions have been defined.

Chapter 7

7 Conclusions and Future Work

This chapter presents the main conclusions derived from the work developed in the course of this PhD research project. Then, possible lines of further study extending the scope of the present work are proposed. Finally, the scientific contributions published during the development of this thesis are listed.

7.1 General conclusions

The main objective of this study was to achieve a suitable microstructure and properties for a novel aeronautic quality castable TNM alloy, by modifying the chemical composition, optimizing solidification and HT.

The chemical composition of a cast TiAl alloy was designed to achieve enhanced structural properties, with the aim of developing a creep resistant microstructure. To this end, the process parameters during casting were adapted to obtain a suitable as-cast microstructure. With a subsequent thermomechanical treatment, a microstructure with suitable mechanical properties close to those of conventional forged TNM alloys through microstructural control was achieved.

From this process, the following conclusions were drawn:

- The TNM-0.1B master alloy does not meet the requirements as it shows segregations with the presence of brittle ribbon borides, both of which are detrimental to the mechanical properties of the alloy. Thus, the chemical composition and the solidification cooling rate were adjusted to precipitate a homogeneous microstructure with the presence of the grain refiner blocky boride. The results of this study indicate that ribbon borides are formed under non-equilibrium conditions, even if the amount of boron is high enough to precipitate blocky borides when the cooling rate is too high. Nevertheless, when boron contents are above a critical value (for the modified TNM alloy, above 0.5 at.%), and the cooling rate during solidification is below 10 K/s, blocky borides are precipitated under equilibrium conditions. In general, the cooling rate during solidification seems to be more relevant than chemical composition to the precipitation of either ribbon or blocky borides. Therefore, to obtain a refined microstructure with no segregation, a cooling rate below 10 K/s and a boron content above the mentioned critical value must be ensured. Under these conditions a TNM-1.5B alloy was obtained which, with further processing, achieves the final suitable microstructure and optimised properties.

- Only when the as-cast homogeneous microstructure contains the grain refiner blocky boride, can the designed appropriate thermomechanical processing successfully provide the required final properties. For this purpose, a suitable HIP and HT were designed. The HIP treatment was set to at 1250 ºC for 3 h at 200 MPa in Ar atmosphere, which removed the defects arising from the casting process. As regards HT, a single-step-treatment allowed the development of the target microstructure. Consisting of a nearly fully-lamellar microstructure with some globular γ-phase in the grain boundaries, this provided an enhanced creep resistant microstructure. The HT had initial conventional heating to the envisaged treatment temperature at a cooling rate of 10 K/min. This was followed by, an isothermal step at 1260 ºC during 1 h which reduced the detrimental effect of β-phase and limited the precipitation of the γ-phase grains at the lamellae colony boundaries. Finally, a cooling rate of 30 K/min was applied that provided the most suitable microstructure for structural applications by achieving a lamellar colony size below 100 µm and an α_2/γ-lamellar spacing below 1 µm, respectively. In addition, some small globular γ-phase helped increase ductility, eliminating the fragility associated with fully lamellar microstructures. Application of the thermomechanical processing described above, results in a final microstructure exhibiting optimal properties for creep resistance applications.

- To evaluate the performance of the final developed microstructure, creep tests were carried out, trying to emulate the in-service conditions to which the material would be exposed. The results reveal that the novel modified TNM-1.5B-IHH alloy exhibited improved creep strength in comparison to the modified TNM-0.8B-HIPIMR-HT alloy. The improvement of the minimum creep rate and the creep life at 750 ºC and under a load of 200 MPa, almost doubled. This is mainly due to the development of the suitable as-cast microstructure (homogeneous with a large number of blocky borides), and to some extent to being subjected to the IHH process instead of the conventional HT. The new manufacturing route applied to the TNM-1.5B-IHH presents the opportunity to reduce processing time and cost by eliminating the forging process and integrating the HIP and HT processes into a single IHH process. In this way, similar properties to conventional forged TNM alloys can be achieved.

Therefore, the combination of chemical composition design, adjustment of the solidification cooling rate, and subsequent IHH thermomechanical processing, produces final cast TiAl components with an optimized microstructure which exhibits properties close to those of conventional forged TNM alloys.

7.2 Future work

This dissertation presents novel titanium aluminides based on the TNM alloy, which require a simpler processing route while achieving similar mechanical properties. Moreover, this research establishes the process conditions for β-solidifying TNM based alloys to obtain a suitable microstructure. These process conditions incorporate the whole manufacturing process, from melting/casting to thermomechanical processing. In the course of this work, the following research lines have also been identified, to satisfy some points of interest:

- Analyse the effect of the morphology and quantity of the different micro-constituents on the crack propagation threshold. This would help determine when the crack starts to spread and the subsequent loss of required properties. As brittleness is the main disadvantage of TiAl alloys, develop new chemical compositions to improve the brittleness of the material at low temperature, aiming to improve the ductility of the brittle α_2-phase.

- Enhance the stability of the γ-phase and delay its decomposition during creep by modifications in the chemical compositions and HT. This would increase the time that the component is capable of withstanding at high temperatures, without losing mechanical properties.

- Develop a chemical thermodynamics and kinetics model that correlates the chemical composition with the cooling rate to predict the phases to be formed.

- Evaluate the combined effect of pressure and temperature on the stability of the different phases, enabling the development of optimised IHH cycles for different modified TNM alloys.

- Fine-tune the IHH processing conditions to achieve optimal results. The processing conditions of the IHH are not fully optimized for the tested alloys, as a result of a small variation in the chemical compositions and solidification conditions between samples subjected to the IHH, and the samples for which the HT was designed. In addition, it is expected that both HIP and HT processing conditions differ when both processes are performed integrated.

- Develop new casting strategies to increase the overheating of the melt and thus prevent premature solidification. This could be achieved through the use of a hot wall crucible instead of the cold crucible, using graphite crucibles.

- Develop new shell layers and localized insulators that provide controlled cooling rates. This would obtain a controlled cooling rate along the entire length of the part, allowing the development of more complex components while maintaining an adequate microstructure.

- Improve the creep strength during the primary creep stage, by the design of an enhanced HT. This may include a stabilisation treatment as a last stage in the IHH cycle.

7.3 Publications

Chamorro X, Herrero-Dorca N, Bernal D, Hurtado I (2019), "Induction skull melting of Ti-6Al-4V: Process control and efficiency optimization," Metals (Basel)., vol. 9, no. 5, pp. 1–11, doi:10.3390/met9050539.

Bernal D, Chamorro X, Hurtado I, Madariaga I (2020a), "Evolution of lamellar microstructures in a cast TNM alloy modified with boron through single-step heat treatments," Intermetallics, vol. 124, no. May, p. 106842, doi:10.1016/j.intermet.2020.106842.

Bernal D, Chamorro X, Hurtado I, Madariaga I (2020b), "Effect of Boron Content and Cooling Rate on the Microstructure and Boride Formation of β-Solidifying γ-TiAl TNM Alloy," Metals (Basel)., vol. 10, no. Special Issue: Alloy Design and Microstructural Control of Structural Intermetallic Alloys, p. 12, doi:10.3390/met10050698.

Bernal D, Chamorro X, Hurtado I, "Behaviour and kinetic oxidation of several titanium based alloys employed in aeronautics," Proceedings of the XV Congreso Nacional de Materiales, Salamanca (Spain), 4 to 6 July 2018. (Oral presentation).

Bernal D, Chamorro X, Hurtado I, "Mould-metal reactivity study of Ti-6Al-4V versus intermetallic TNM-B1," EICF Euro Seminar, Helsinki (Finland), 20 to 22 May 2019. (Oral presentation).

Chapter 8

8 Bibliographic References

[1] F. Appel, J. Paul, and M. Oehring, Gamma Titanium Aluminide Alloys, vol. 1. Weinheim: Wiley, 2014.

[2] U. Habel, F. Heutling, C. Kunze, W. Smarsly, G. Das, and H. Clemens, "Forged Intermetallic γ-TiAl Based Alloy Low Pressure Turbine Blade in the Geared Turbofan," in Proceedings of the 13th World Conference on Titanium, 2016, pp. 1223–1227.

[3] S. Mayer et al., "Intermetallic β-Solidifying γ-TiAl Based Alloys − From Fundamental Research to Application," Adv. Eng. Mater., vol. 19, no. 4, pp. 1–27, 2017.

[4] L. M. Droessler, "Characterization of β-solidifying γ-TiAl alloy variants using advanced in- and ex-situ investigation methods," no. October, 2008.

[5] C. Leyens and M. Peters, Titanium an titanium alloys. 2003.

[6] J. M. Palacios, "Titanium and Titanium Alloys," Trater Press, Nov-2017.

[7] B. Sefer, Oxidation and Alpha – Case Phenomena in Titanium Alloys used in Aerospace Industry : Ti – 6Al – 2Sn – 4Zr – 2Mo and Ti – 6Al – 4V Birhan Sefer, no. July 2016. 2017.

[8] H. Sibum, V. Güther, O. Roidl, F. Habashi, H. U. Wolf, and C. Siemers, "Titanium, Titanium Alloys, and Titanium Compounds. Ullmann's Encyclopedia of Industrial Chemistry," Ullmann's Encycl. Ind. Chem., vol. 37, pp. 1–35, 2017.

[9] M. E. Kassner and M. T. Pérez-Prado, Fundamentals of Creep in Metals and Alloys. 2015.

[10] F. Appel, H. Clemens, and F. D. Fischer, "Modeling concepts for intermetallic titanium aluminides," Prog. Mater. Sci., vol. 81, pp. 55–124, 2016.

[11] H. Clemens, "Materials for Aircraft Engines ACARE * targets for 2020 Future challenges," Presentation, no. x, 2015.

[12] T. Klein, "Phase transformations and grain growth in TNM based alloys," Diploma Thesis, no. October, 2013.

[13] T. Klein, H. Clemens, and S. Mayer, "Advancement of compositional and microstructural design of intermetallic γ-TiAl based alloys determined by atom probe tomography," Materials (Basel)., vol. 9, no. 9, 2016.

[14] H. Sarriegi, "Calphad Coupled Microstructure Modelling of the AZ91E Mg Alloy Gravity Die Casting," Tesis MGEP, 2013.

[15] M. Rappaz, "Modelling of microstructure formation in solidification processes no," vol. 34, no. 3, 1989.

[16] T. T. Cheng, "Mechanism of grain refinement in TiAl alloys by boron addition - an alternative hypothesis," Intermetallics, vol. 8, no. 1, pp. 29–37, 2000.

[17] T. Klein, S. Niknafs, R. Dippenaar, H. Clemens, and S. Mayer, "Grain growth and

β to α transformation behavior of a β-solidifying TiAl alloy," Adv. Eng. Mater., vol. 17, no. 6, pp. 786–790, 2015.

[18] H. Clemens and S. Mayer, "Design, processing, microstructure, properties, and applications of advanced intermetallic TiAl alloys," Adv. Eng. Mater., vol. 15, no. 4, pp. 191–215, 2013.

[19] P. Tchoupé Ngnekou, "Microstructure, oxydation et propriétés mécaniques d'alliages intermétalliques à base de TiAl," 2010.

[20] C. Yang, H. Jiang, D. Hu, A. Huang, and M. Dixon, "Effect of boron concentration on phase transformation texture in as-solidified Ti44Al8Nb x B," vol. 67, pp. 85–88, 2012.

[21] U. Kitkamthorn, L. C. Zhang, and M. Aindow, "The structure of ribbon borides in a Ti-44Al-4Nb-4Zr-1B alloy," Intermetallics, vol. 14, no. 7, pp. 759–769, 2006.

[22] D. Hu, "Role of boron in TiAl alloy development: a review," Rare Met., vol. 35, no. 1, pp. 1–14, 2016.

[23] H. Clemens, W. Wallgram, S. Kremmer, V. Güther, A. Otto, and A. Bartels, "Design of novel β-solidifying TiAl alloys with adjustable β/B2-phase fraction and excellent hot-workability," Adv. Eng. Mater., vol. 10, no. 8, pp. 707–713, 2008.

[24] A. V Kartavykh, M. V Gorshenkov, and D. A. Podgorny, "Grain refinement mechanism in advanced γ-TiAl boron-alloyed structural intermetallics: The direct observation," Mater. Lett., vol. 142, pp. 294–298, 2015.

[25] M. Oehring, A. Stark, J. D. H. Paul, T. Lippmann, and F. Pyczak, "Microstructural refinement of boron-containing β-solidifying γ-titanium aluminide alloys through heat treatments in the β phase field," Intermetallics, vol. 32, pp. 12–20, 2013.

[26] D. Hu, "Effect of boron addition on tensile ductility in lamellar TiAl alloys," Intermetallics, vol. 10, no. 9, pp. 851–858, 2002.

[27] V. T. Witusiewicz, A. A. Bondar, U. Hecht, J. Zollinger, L. V. Artyukh, and T. Y. Velikanova, "The Al-B-Nb-Ti system. V. Thermodynamic description of the ternary system Al-B-Ti," J. Alloys Compd., vol. 474, no. 1–2, pp. 86–104, 2009.

[28] M. Naveed, A. F. Renteria, and S. Weiß, "Role of alloying elements during thermocyclic oxidation of β/γ-TiAl alloys at high temperatures," J. Alloys Compd., vol. 691, pp. 489–497, 2017.

[29] L. Song, X. J. Xu, J. Sun, and J. P. Lin, "Cooling rate effects on the microstructure evolution in the βozones of cast Ti-45Al-8.5Nb-(W, B, Y) alloy," Mater. Charact., vol. 93, pp. 62–67, 2014.

[30] T. Klein, M. Schachermayer, D. Holec, B. Rashkova, H. Clemens, and S. Mayer, "Intermetallics Impact of Mo on the u o phase in b -solidifying TiAl alloys : An experimental and computational approach," vol. 85, pp. 26–33, 2017.

[31] R. Muñoz, "In situ analysis of the high temperature deformation and fracture mechanisms Rocío Muñoz Moreno Ph . D Thesis In situ analysis of the high temperature," no. May, 2014.

[32] F. Appel and R. Wagner, "Microstructure and deformation of two-phase γ-titanium aluminides," Mater. Sci. Eng. R, vol. 22, no. 5, pp. 187–268, 1998.

[33] R. Chen et al., "Brittle–ductile transition during creep in nearly and fully lamellar

high-Nb TiAl alloys," Intermetallics, vol. 93, no. October 2017, pp. 47–54, 2018.

[34] Y. Hao, J. Liu, S. Li, J. Li, X. Liu, and X. Feng, "Effects of nano-twinning on the deformation and mechanical behaviours of TiAl alloys with distinct microstructure at elevated loading temperatures," Mater. Sci. Eng. A, vol. 705, no. April, pp. 210–218, 2017.

[35] M. S. Dahar, S. A. Tamirisakandala, and J. J. Lewandowski, "Evolution of fatigue crack growth and fracture behavior in gamma titanium aluminide Ti-43.5Al-4Nb-1Mo-0.1B (TNM) forgings," Int. J. Fatigue, vol. 111, no. October 2017, pp. 54–69, 2018.

[36] E. Schwaighofer et al., "Microstructural design and mechanical properties of a cast and heat-treated intermetallic multi-phase γ-TiAl based alloy," Intermetallics, vol. 44, pp. 128–140, 2014.

[37] M. Schloffer et al., "Microstructure development and hardness of a powder metallurgical multi phase γ-TiAl based alloy," Intermetallics, vol. 22, pp. 231–240, 2012.

[38] H. Clemens, W. Smarsly, V. Güther, and S. Mayer, "Advanced Intermetallic Titanium Aluminides," pp. 1189–1200, 2016.

[39] Y. W. Kim and D. M. Dimiduk, "Progress in the understanding of gamma titanium aluminides," Jom, vol. 43, no. 8, pp. 40–47, 1991.

[40] M. Li, S. Xiao, Y. Chen, L. Xu, and J. Tian, "The effect of boron addition on the deformation behavior and microstructure of β-solidify TiAl alloys," Mater. Charact., vol. 145, no. August, pp. 312–322, 2018.

[41] X. Wu, D. Hu, and M. H. Loretto, "Alloy and process development of TiAl," J. Mater. Sci., vol. 39, no. 12, pp. 3935–3940, 2004.

[42] S. Mayer, E. Schwaighofer, M. Schloffer, and H. Clemens, "The use of in-situ characterization techniques for the development of intermetallic titanium aluminides," Mater. Sci. Forum, vol. 783–786, pp. 2097–2102, 2014.

[43] Q. Wang et al., "Effects of lamellar spacing on microstructural stability and creep properties in β-solidifying γ-TiAl alloy by directional solidification," Mater. Sci. Eng. A, vol. 711, no. November 2017, pp. 508–514, 2018.

[44] V. Güther, M. Allen, J. Klose, and H. Clemens, "Metallurgical processing of titanium aluminides on industrial scale," Intermetallics, vol. 103, no. August, pp. 12–22, 2018.

[45] H. Clemens and S. Mayer, "Intermetallic titanium aluminides in aerospace applications – processing, microstructure and properties," Mater. High Temp., vol. 33, no. 4–5, pp. 560–570, 2016.

[46] R. A. Harding, "Recent developments in the induction skull melting and investment casting of titanium aluminides," Kov. Mater., vol. 42, no. 4, pp. 225–241, 2004.

[47] C. Yang, "Solidification behaviour and hipping induced surface modification in Ti4522XD castings," no. January, 2012.

[48] J. A. Stendal, M. Eisentraut, I. Sizova, S. Bolz, M. Bambach, and S. Weiß, "Effect of heat treatment on the workability of hot isostatically pressed TNM-B1," AIP

Conf. Proc., vol. 2113, no. July, 2019.

[49] A. Umbrashko, E. Baake, B. Nacke, and A. Jakovics, “Experimental investigations and numerical modelling of the melting process in the cold crucible,” COMPEL - Int. J. Comput. Math. Electr. Electron. Eng., vol. 24, no. 1, pp. 314–323, 2005.

[50] I. Quintana, “Numerical modelling of cold crucible induction melting (CCIM) process and fabrication of high value added components of titanium and its alloys,” Tesis MGEP, 2013.

[51] X. Chamorro, “Microfusión de Ti-6Al-4V : análisis y control de defectos,” Tesis MGEP, 2017.

[52] A. Book, “Principle , advantages , limitations and applications of two-colour pyrometers in thermal processes,” Infrared Thermom. Solut., pp. 1–8, 2010.

[53] Omega, “Omega Thermocouple Tolerance Values,” Thermocouple Toler. Values, available <http//www.omega.com/techref/colorcodes.html>, pp. 1–7.

[54] A. S. Ellab, “6 key Differences Between RTD ’ s and Thermocouples - that Might Change your Preferences,” White Paper. 2019.

[55] R. M. Park, “Thermocouple Fundamentals,” White Paper. Marlin Manufacturing Corporation, 2001.

[56] A. V. Fadeev, V. E. Bazhenov, and A. V. Koltygin, “Improvement in the casting technology of blades for aviation gas-turbine engines made of TNM-B1 titanium aluminide alloy produced by induction crucible melting,” Russ. J. Non-Ferrous Met., vol. 56, no. 1, pp. 26–32, 2015.

[57] M. Kastenhuber, T. Klein, B. Rashkova, I. Weißensteiner, H. Clemens, and S. Mayer, “Phase transformations in a β-solidifying γ-TiAl based alloy during rapid solidification,” Intermetallics, vol. 91, no. August, pp. 100–109, 2017.

[58] M. Oehring, F. Appel, J. H. D. Paul, R. M. Imayev, V. M. Imayev, and U. Lorenz, “Microstructure Formation in Cast β-Solidifying γ-Titanium Aluminide Alloys,” Mater. Sci. Forum, vol. 638–642, pp. 1394–1399, 2010.

[59] U. Hecht, V. Witusiewicz, A. Drevermann, and J. Zollinger, “Grain refinement by low boron additions in niobium-rich TiAl-based alloys,” Intermetallics, vol. 16, no. 8, pp. 969–978, 2008.

[60] D. Bernal, X. Chamorro, I. Hurtado, and I. Madariaga, “Effect of Boron Content and Cooling Rate on the Microstructure and Boride Formation of β-Solidifying γ-TiAl TNM Alloy,” Metals (Basel)., vol. 10, no. Special Issue: Alloy Design and Microstructural Control of Structural Intermetallic Alloys, p. 12, 2020.

[61] D. A. Porter and K. E. Easterling, Phase Transformations in Metals and Alloys. Springer-Science+Business Media, B.V., 1992.

[62] M. Kastenhuber, T. Klein, H. Clemens, and S. Mayer, “Intermetallics Tailoring microstructure and chemical composition of advanced γ -TiAl based alloys for improved creep resistance,” Intermetallics, vol. 97, no. January, pp. 27–33, 2018.

[63] P. Erdely et al., “Design and control of microstructure and texture by thermomechanical processing of a multi-phase TiAl alloy,” Mater. Des., vol. 131, pp. 286–296, 2017.

[64] S. K. Rittinghaus, U. Hecht, V. Werner, and A. Weisheit, “Heat treatment of laser

metal deposited TiAl TNM alloy," Intermetallics, vol. 95, no. September 2017, pp. 94–101, 2018.

[65] W. Wallgram, T. Schm, L. Cha, G. Das, H. Clemens, and F. Jeglitsch, "Technology and mechanical properties of advanced c-TiAl based alloys," Int. J. Mat. Res. (formerly Z. Met., pp. 1021–1030, 2009.

[66] D. Bernal, X. Chamorro, I. Hurtado, and I. Madariaga, "Evolution of lamellar microstructures in a cast TNM alloy modified with boron through single-step heat treatments," Intermetallics, vol. 124, no. May, p. 106842, 2020.

[67] M. Kastenhuber, B. Rashkova, H. Clemens, and S. Mayer, "Enhancement of creep properties and microstructural stability of intermetallic β-solidifying γ-TiAl based alloys," Intermetallics, vol. 63, pp. 19–26, 2015.

[68] J. Overton and B. Eng., "Thermophysical property and phase transformation determination of TiAl intermetallics," Carleton University, Ottawa, 2006.

[69] M. Ahlfors, J. Shipley, and I. Lopez-Galilea, "Hot Isostatic Pressing for the Casting Industry," eicf (European investment casters' federation), 2019.

[70] A. Chatterjee, H. Mecking, E. Arzt, and H. Clemens, "Creep behavior of g -TiAl sheet material with differently spaced fully lamellar microstructures," vol. 331, pp. 840–846, 2002.

[71] S. T. Methods, "Standard Test Methods for Conducting Creep , Creep-Rupture , and Stress-Rupture Tests of Metallic Materials 1," pp. 1–14, 2014.

[72] J. R. Davis, Heat Resistant Materials, ASM. ASM International, 1997.

[73] H. Oikawa and Y. Iijima, "Diffusion behaviour of creep-resistant steels," in Creep-Resistant Steels, 2008, pp. 241–264.

[74] W. T. Marketz, F. D. Fischer, and H. Clemens, "Deformation mechanisms in TiAl intermetallics — experiments and modeling," vol. 19, pp. 281–321, 2003.

[75] F. Appel, "TiAl Intermetallics," Encycl. Aerosp. Eng., pp. 1–14, 2010.

[76] X. Du, J. Zhu, and Y. Kim, "Microstructural characterization of creep cavitation in a fully-lamellar TiAl alloy," vol. 9, pp. 137–146, 2001.

[77] H. Z. Niu, Y. Y. Chen, S. L. Xiao, and L. J. Xu, "Microstructure evolution and mechanical properties of a novel beta γ-TiAl alloy," Intermetallics, vol. 31, pp. 225–231, 2012.

[78] T. Leitner, M. Schloffer, S. Mayer, J. Eßlinger, H. Clemens, and R. Pippan, "Fracture and R-curve behavior of an intermetallic β-stabilized TiAl alloy with different nearly lamellar microstructures Dedicated to Dr. Wilfried Smarsly on the occasion of his 60th birthday.," Intermetallics, vol. 53, pp. 1–9, 2014.

[79] M. Burtscher, T. Klein, S. Mayer, H. Clemens, and F. D. Fischer, "The creep behavior of a fully lamellar γ-TiAl based alloy," Intermetallics, vol. 114, no. September, p. 106611, 2019.

[80] R. Yamamoto, K. Mizoguchi, G. Wegmann, and K. Maruyamat, "Effects of discontinuour coarsening of lamellae on creep strength of fully lamellar TiAl alloys," vol. 6, pp. 699–702, 1998.

[81] C. Körner et al., "Microstructure and Mechanical Properties of CMSX-4 Single Crystals Prepared by Additive Manufacturing," Metall. Mater. Trans. A Phys.

Metall. Mater. Sci., vol. 49, no. 9, pp. 3781–3792, 2018.

[82] D. Huber, R. Werner, H. Clemens, and M. Stockinger, “Materials Characterization In fl uence of process parameter variation during thermo-mechanical processing of an intermetallic β -stabilized γ -TiAl based alloy,” Mater. Charact., vol. 109, pp. 116–121, 2015.